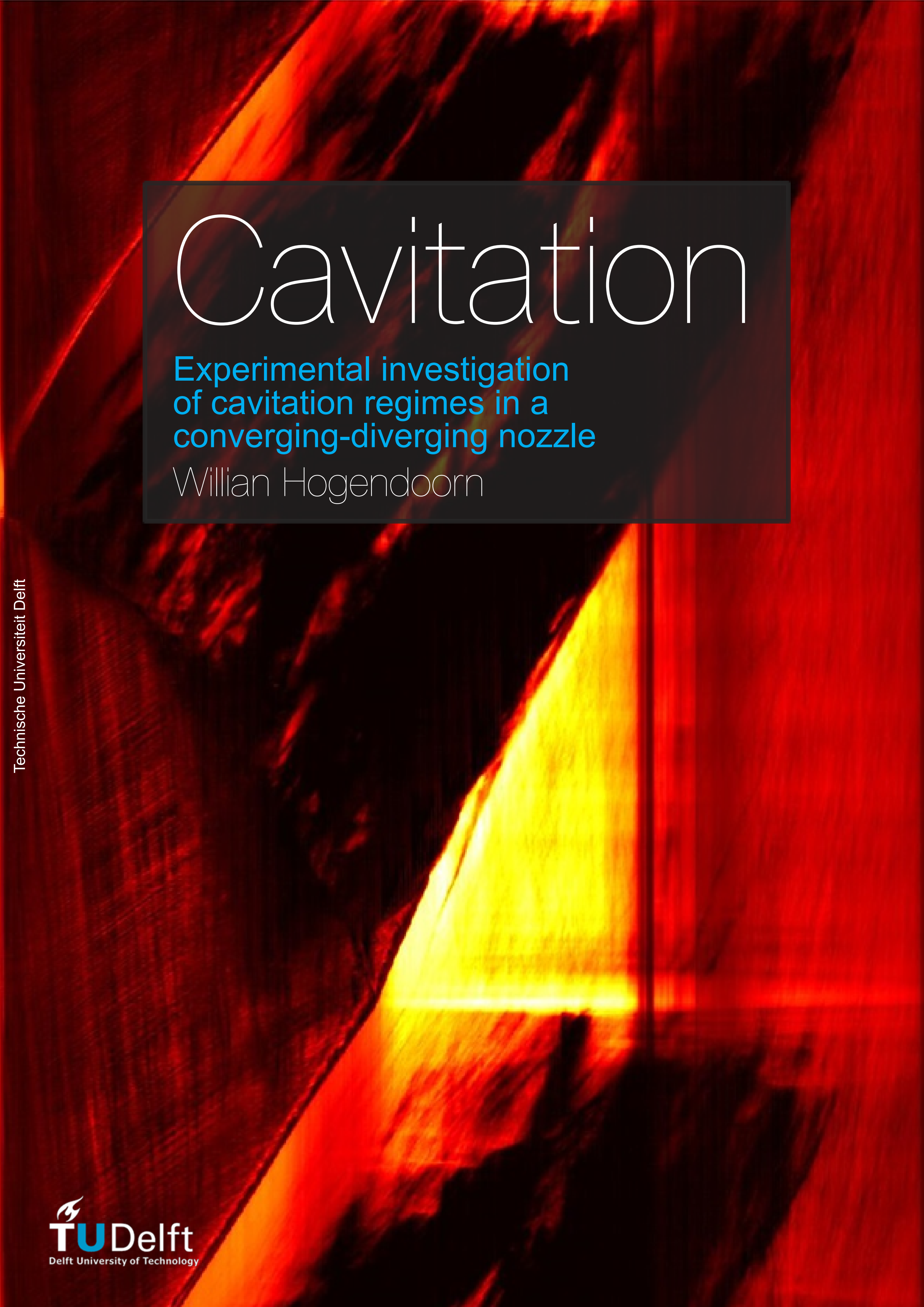

Cavitation

Experimental investigation of cavitation regimes in a converging-diverging nozzle

Willian Hogendoorn

Technische Universiteit Delft

TU Delft
Delft University of Technology

Cavitation

Experimental investigation of cavitation regimes in a converging-diverging nozzle

by

Willian Hogendoorn

to obtain the degree of Master of Science
at the Delft University of Technology,
to be defended publicly on Wednesday May 3, 2017 at 14:00.

Student number:	4223616	
P&E report number:	2817	
Project duration:	September 6, 2016 – May 3, 2017	
Thesis committee:	Prof. dr. ir. C. Poelma,	TU Delft, supervisor
	Prof. dr. ir. T. van Terwisga,	MARIN
	Dr. R. Delfos,	TU Delft
	MSc. S. Jahangir,	TU Delft, daily supervisor

TU Delft

Contents

Preface

This master thesis report is the result of a graduation period at the Fluid Mechanics department (3ME) at the TU Delft. The thesis is a part of the master Mechanical Engineering with specialisation Sustainable Process and Energy Technologies.

In this graduation period, different cavitation regimes in a converging-diverging nozzle are experimentally investigated. For readers who are especially interested in the aqcuired results, are refered to chapter 6.

Finally I would like to express my appreciation to Prof. dr. ir. C. Poelma for this master thesis position and his supervision during the graduation period. I want to thank Msc. S. Jahangir for his daily supervision and his valuable advises during this master thesis. I am grateful to the other members of my thesis committee for their participation. I am also grateful to all the other people in the fluid mechanics laboratory who supported me throughout this research project.

Willian Hogendoorn
Delft, April 2017

Abstract

In this study different cavitation regimes in a venturi have been investigated, in order to validate and develop numerical two-phase flow models further with the data obtained. The different cavitation regimes are generated by systematically changing the global static pressure and flow velocity in the flow loop. Cavitation behavior has been captured by temperature and pressure sensors and a high speed camera. The cavitation behavior has been described by means of non-dimensional parameters such as cavitation number, Strouahl number and the pressure loss coefficient.

When the cavitation number is based on downstream static pressure, the pressure loss coefficient has been found to be a linear function of cavitation number only. Flow blockage is increasing for decreasing cavitation number. When the cavitation number is based on downstream static pressure, cavity length and time scales as function of cavitation number are also collapsing on one single curve. A non-linear behavior has been found for the cavity length scale, as well as the cavity time scale. Both the length and time scale are combined in the Strouhal number, based on the cavity lengths at time of detachment. This Strouhal number is the dimensionless form of the global cavity growth velocity. It follows that for this Strouhal number, as function of cavitation number, a global minimum has been found for a cavitation number $\sigma = 0.88$. Based on this result, three different cloud cavitation shedding regimes have been identified. For $\sigma > 0.95$, the periodic cavity shedding is caused by the re-entrant jet mechanism. For $\sigma < 0.8$, the prevalent mechanism for periodic cavity shedding is the bubbly shock mechanism. Whereas both mechanisms have been observed in the transition region, $0.8 < \sigma < 0.95$.

Data analysis on basis of high speed video recordings ($\sigma < 0.8$) has indicated the presence of a pressure wave or bubbly shock, induced by bubble cloud collapse. The propagation velocity of this pressure wave in the growing cavity has been quantified. By means of the correlation between speed of sound and void fraction, the void fraction in the growing cavity has been estimated. The highest void fraction has been found in the cavity front, whereas the void fraction decreases in the direction of the venturi throat. At the throat the lowest void fraction has been found, which is 1.1 % in case of a cavitation number of $\sigma = 0.4$. From this void fraction profile the mechanism of cavity detachment in pressure wave driven cavitation has been derived. The pressure wave partially condensates the growing cavity. The link between the cavity and the venturi throat is broken by full condensation of the connecting cavity part, where the void fraction is lowest. The condition for full condensation of the connecting cavity part is only met for a pressure wave with a certain minimum amplitude.

An introduction towards shear or jet cavitation has been given, based on the results as found. To this end, the Mach number has been introduced in order to relate the pressure wave velocity with the cavity growth velocity. For the critical Mach number, Ma = 1, shear cavitation is initiated, since the pressure wave can not travel upstream and detach the growing cavity by means of condensation. Based on linear extrapolation of the results obtained, a critical cavitation number of $\sigma = 0.11$ has been found. This result has been confirmed by experimental observations which show shear cavitation at $\sigma \approx 0.1$.

Both mechanisms are causing cavity shedding in the intermediate cavitation region $0.8 < \sigma < 0.95$. More quantitative investigation has been advised for this specific region. This will lead to a better understanding of the time and length scales of both detachment mechanisms. Furthermore, verification of the current estimation of the void fraction profiles has been recommended. This verification can be done by means of X-ray measurements. From these measurements the effective throat diameter as function of position can also be obtained. With this, yet unknown, variable, the complete cavitation dynamics can be determined as function of time. In addition, more velocity measurements (i.e. pressure wave and cavity growth) for $0.05 < \sigma < 0.3$ have been advised, in order to verify the expected critical cavitation number for which shear cavitation is induced.

Nomenclature

α	air volume fraction
β	normalized grayscale level
Δh	water height
Δp	pressure drop over venturi
Δp_{vapor}	pressure loss over venturi due to wall friction losses
ν	kinematic viscosity
Π	dimensionless pressure
ρ	density
ρ_l	density of water (liquid)
ρ_v	density of water vapor
σ	Cavitation number
c	local speed of sound
c_l	speed of sound in pure liquid
d	tube diameter
d_t	venturi throat diameter
f	cavity shedding frequency
f_s	cavity shedding frequency goverened by re-entrant jet mechanism
f_w	cavity shedding frequency goverened by bubbly shock mechanism
Fs	sample frequency
g	acceleration of gravity
K	Pressure loss coefficient
k	process describing constant
m	position for FFT
Ma	Mach number
n	number of divisions of signal
P	vapor pressure
p	pressure
p_0	reference pressure
p_i	pressure at pump inlet
p_v	vapor pressure

r	bubble radius
R_0	initial bubble radius
Re_d	Reynolds number based on tube diameter
St_{d_t}	Strouhal number based on venturi throat diameter
T	temperature
U	average stream-wise velocity
u	flow velocity
u_0	reference velocity
U_{crit}	critical velocity for which cavitation inception starts
V_i	velocity at pump inlet
z	position in direction of gravity
l_0	cavity length at time of detachment
p_∞	far field pressure
St_{l_0}	Strouhal number based on cavity length

1

Introduction and outline

Cavitation is a phenomenon with both positive and negative effects, occurring in a wide variety of applications. In general the word ’cavitation’ has a negative connotation. Indeed, in many applications cavitation is an undesired phenomenon, for instance cavitation occurring in turbomachinery. In this case cavitation is the cause of erosion of the impellor blades, noise production and system vibrations, leading to failure fatique. Cavitation occurring at ship propellors is also a real problem, because of efficiency drop, wear and noise production. However, in some cases, cavitation can have positive effects, for example to mix two or more dissimilar fluids [14]. Furthermore, in the biomedical world cavitation is used in order to destruct kidney stones in shock wave lithotripsy [43]. The first research towards cavitation, occurring at ship propellors, was conducted by Osborne Reynolds in 1873 [29]. However, Reynolds was not able to find the cause of the problem, which is vaporization of water in low pressure regimes. A few decades later Charles Algernon Parsons encountered problems with his famous turbine driven ship named Turbinia [40]. Parsons investigated the cause of the loss of power by means of a self-built cavitation tunnel, which is still in existence and can be seen at the University of Newcastle-upon-Tyne. In the years after the building of this first cavitation tunnel, a lot of research and effort have been put into the physical understanding of the mechanisms behind cavitation. After more than a century of research, still questions are open or arise and the fundamental physics of cavitation are not yet fully understood. Understanding of these physics is important, because then the harmfull effects of cavitation can be minimized and the positive effects can be maximized. Also, with the growth of computational power and the development of numerical flow models, it is important to understand these physics. By implementation of the right cavitation physics in the models, reliable predictions about cavitation behavior and impact can be given.

1.1. Introduction of main research themes

The purpose of this master thesis is to serve the above presented goal of research towards the cavitation mechanisms, in order to implement these physics in numerical flow models. Practically, this implies a study towards the different cavitation regimes in a converging-diverging (CD) axisymmetric nozzle. The different cavitation regimes are generated by varying the global static pressure and flow velocity. Cavitation behavior is captured by temperature and pressure sensors and a high speed camera. For data post-processing different cavitation-describing parameters are used, such as cavitation number, Reynolds number, Strouhal number and the pressure loss coefficient. With the obtained data, numerical two-phase flow models can be validated and further developed.

1.2. Outline of report

This report starts with a literature study in chapter 2. First an introduction to cavitation is given. Subsequently the relevant fluid parameters, required for experimental data processing, are discussed. The chapter ends with a summary of the current state of the art. The experimental setup with the corresponding measurement devices is discussed in chapter 3. The highspeed imaging method is also explained in further detail. In chapter 4, the experimental procedure is presented. In this chapter, the calibration of the camera is discussed, as well as the used camera settings. The data acquisition method is also described in this chapter. In chapter 5 the method of data processing is discussed. In this chapter is described how physical quantities are extracted from the video data. The measurement results are presented in chapter 6. First the basic cavitation dynamics are explained. Thereafter the measurement results are presented from which the cavitation physics are derived. Two different cloud cavitation shedding mechanisms are discussed, as well as the shear or jet cavitation phenomenon and the expected physics behind. Finally a conclusion is given as well as some recommendations for further research in chapter 7.

2

Literature study and theoretical background

In this chapter the literature study and theoretical background are presented. To that end this chapter starts with an introduction to cavitation in section 2.1. The relevant parameters, that describes cavitating flows, are discussed in section 2.2. In section 2.3, the current state of the art is presented as well as the research towards the mechanism behind unsteady cloud cavitation shedding.

2.1. Introduction to cavitation

Cavitation can be explained by using a pressure-temperature diagram. This so-called phase diagram is presented in Figure 2.1. Cavitation is the same as boiling, in the sense that during both processes the saturated vapor/liquid line is crossed. At this line, the chemical potential of both phases is the same. Whereas for boiling the temperature of the medium is increased and by that the substance is vaporized, phase transition in case of cavitation is caused by decreasing the pressure. During this phase transition vapor pockets or cavities are formed, because this state is energetically favourable. The pressure at which these vapor cavities are formed, is the so-called vapor pressure. For water at 100°C this vapor pressure is 1 bar atm and in case of 20°C this vapor pressure is reduced to 0.0231 bar atm. It is important to note that pure water cannot cavitate [3]. Impurities in the medium, such as nuclei, small initial bubbles and dissolved gas are required for cavitation inception. Even cosmic radiation can be a source of impurities, causing cavitation inception [34].

An experiment, performed in the 1960s, by Lindgren and Johnsson [24], presents the complicated nature of quantitative cavitation inception measurements. The cavitation inception on the same axisymmetric headform (this headform is also refered as the ITTC headform, because it is conducted as part of the International Towing Tank Conference) is measured in various laboratories around the world. In this experiment the cavitation inception is measured with a certain dimensionless number, the so-called cavitation number (see Equation 2.3, which will be discussed in detail later), as function of the water tunnel speed. The obtained results are combined in one figure, which is presented in Figure 2.2. It can be seen that, depending on the water tunnel location, different cavitation inception curves are obtained as function of the water tunnel speed. This has to do with local variables that are extremely difficult, or impossible to control, such as the impurities in the medium, that varies per laboratory location. This makes cavitation a very difficult object of quantitative comparitive research.

In laboratory experiments different cavitation regimes can be observed. Imagine, for instance, a converging-diverging nozzle with a fully developed turbulent fluid flow with certain mean velocity U, density ρ and pressure p. A schematic overview of this situation is presented in Figure 2.3a. In case of a steady, incompressible, single phase flow, this venturi flow is described by Bernoulli's equation [22]:

$$\frac{1}{2}U^2 + gz + \frac{p}{\rho} = a\ constant\ along\ a\ streamline, \tag{2.1}$$

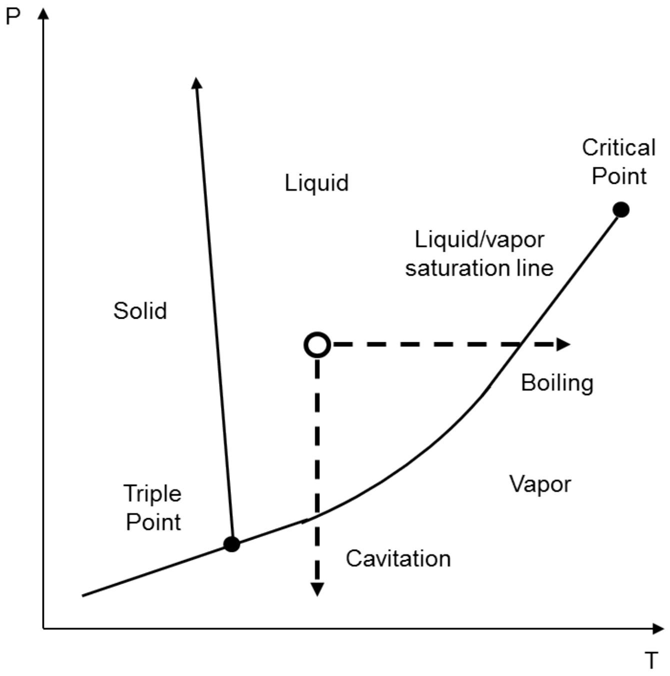

Figure 2.1: Typical phase diagram with three different phases. Depending on temperature (horizontal) and pressure (vertical) a solid, liquid and vapor phase can be distinguished. All phases coexists at the triple point. At the liquid/vapor saturation line the liquid and vapor phase coexists. Starting from the liquid phase, the liquid/vapor saturation line can be crossed horizontally, by means of heating, this process is defined as boiling. The liquid/vapor saturation line can also be crossed vertically, this can be achieved by means of pressure decreasing, this process is defined as cavitation.

where the first term is the velocity term, the second term the gravity term and the third term the pressure term. For a horizontally placed venturi the gravity term vanishes and the velocity term and pressure term are constant along a streamline. This implies that if the velocity is increased, which happens in a venturi, the pressure is decreased. From mass conservation it follows that the maximum velocity is reached at the throat of the venturi. So, at the throat of the venturi the minimum pressure occurs, as can be seen in Figure 2.3b. When there is no cavitation, the situation is depicted by pressure distribution 1. A pressure loss Δp_{vapor} over the venturi is encountered due to (wall) friction losses. By increasing the flow velocity up to a certain critical velocity U_{crit}, the pressure is reduced to the vapor pressure at the throat location. This situation is depicted by pressure distribution 2 in Figure 2.3b. Beyond the throat location the pressure distribution is shown in a dashed line. This dashed line corresponds to the no-cavitation situation. If there are enough nuclei present in the flow to start cavitation inception, vapor filled cavities can be seen. This type of cavitation is called sheet cavitation, because a sheet or ring cavity can be observed. The nature of this cavitation form is irregular, because irregular vapor bubbles/clouds are shed. The pressure distribution of this situation is not depicted, because due to the presence of an aditional phase, the flow pattern is changed in such a way that the pressure distribution becomes time dependent. Further increase of the velocity gives an unsteady form of cavitation. Periodic shedding of complete cavitation clouds can be seen in this phase. This oscillating flow can be described with the Strouhal number (see Equation 2.6, which will be discussed in detail later). This, and the next cavitation forms can be approximated by pressure distribution 3 in Figure 2.3b. In this case the pressure distribution after the throat is not presented due to unsteadiness caused by the two phase flow. This regime of periodic shedding of complete cavity clouds is generally divided in partially developed cavitation and fully developed cavitation. The difference between both regimes is the cavity length, which is larger in fully developed cavitation. However, the distinction between both regimes is rather vague, because no objective criteria are available. The final form of cavitation is the so-called supercavitation or shear cavitation regime. In this regime, the cavitating body is completely enclosed by (in case of external flow) or filled with (in case of internal flow) the cavity. This form of cavitation is for example applied to supercavitating torpedos, in order to reduce the skin friction and by that increasing the maximum velocity up to roughly five times the speed of conventional torpedos [2].

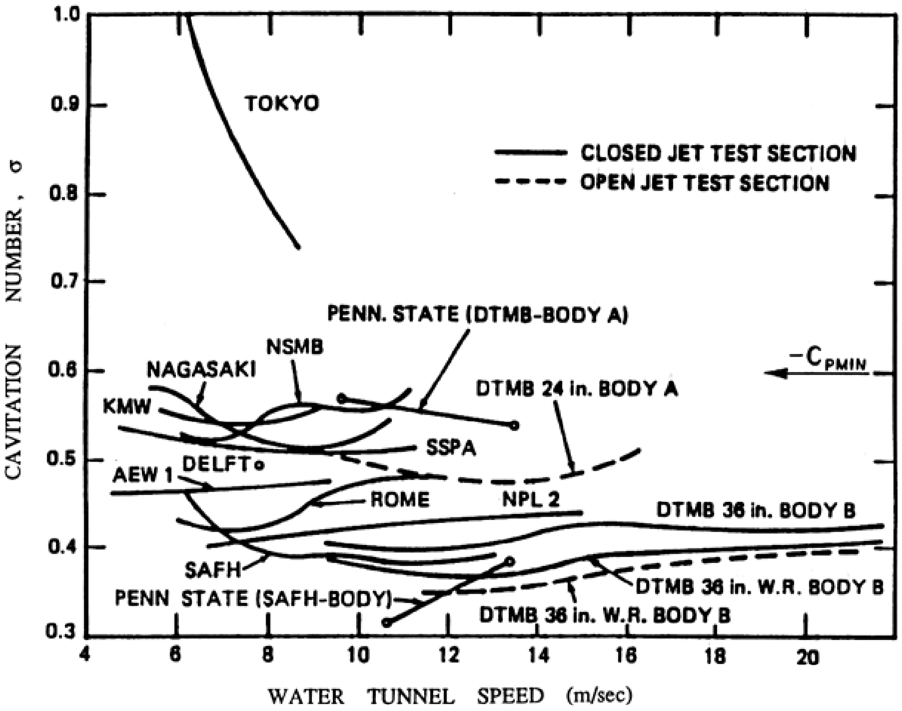

Figure 2.2: Experimental results of cavitation inception numbers as function of water tunnel speeds from different laboratories from all over the world. In all experiments the same headform is used, but different cavitation inception curves are obtained. This is due to the difference in local variables, such as the impurities in the medium that are responsible for cavitation inception. Figure reproduced from Lindgren and Johnsson [24].

2.2. Relevant fluid parameters

In fluid dynamics it is common practice to describe flow situations with dimensionless numbers. Cavitating flows can also be described with these numbers, for example the Strouhal number, as already mentioned above. There are many more dimensionless numbers that are defined in the field of fluid dynamics. The relevant fluid parameters that are used in this thesis, in order to describe cavitation dynamics, are presented in this section.

The Reynolds number presents the ratio between the inertial forces over the viscous forces. Viscous dominant flows are usually described by low Reynolds numbers (laminar flows) and inertia dominant flows are generally described by high reynolds numbers (turbulent flows). The Reynolds number based on the pipe diameter is described by:

$$Re_d = \frac{ud}{\nu}, \tag{2.2}$$

where u is the flow velocity, d the pipe diameter and ν is the kinematic viscosity of the fluid.

Cavitating flows are usually described with a characteristic number that indicates the cavitation intensity. Different definitions of this cavitation number can be found in literature. The general definition is given by:

$$\sigma = \frac{p - p_v}{\frac{1}{2}\rho u_0^2}, \tag{2.3}$$

where p is a pressure at a reference position, p_v is the vapor pressure of the fluid, ρ is the density of the fluid and u_0 is an upstream reference velocity. The cavitation number varies with temperature, since the vapor pressure is temperature dependent. Brennen [3] gives the same definition for the cavitation number, but replaces p with p_0, which denotes the static pressure at the same reference position as the upstream velocity. In the book of Franc and Michel [11], different cavitation numbers, for different objects are defined. In case of a foil, the same same definition as Brennen is given. However, the definition of p_0 is rather different in the venturi case than for the hydrofoil. Due to flow blockage of the

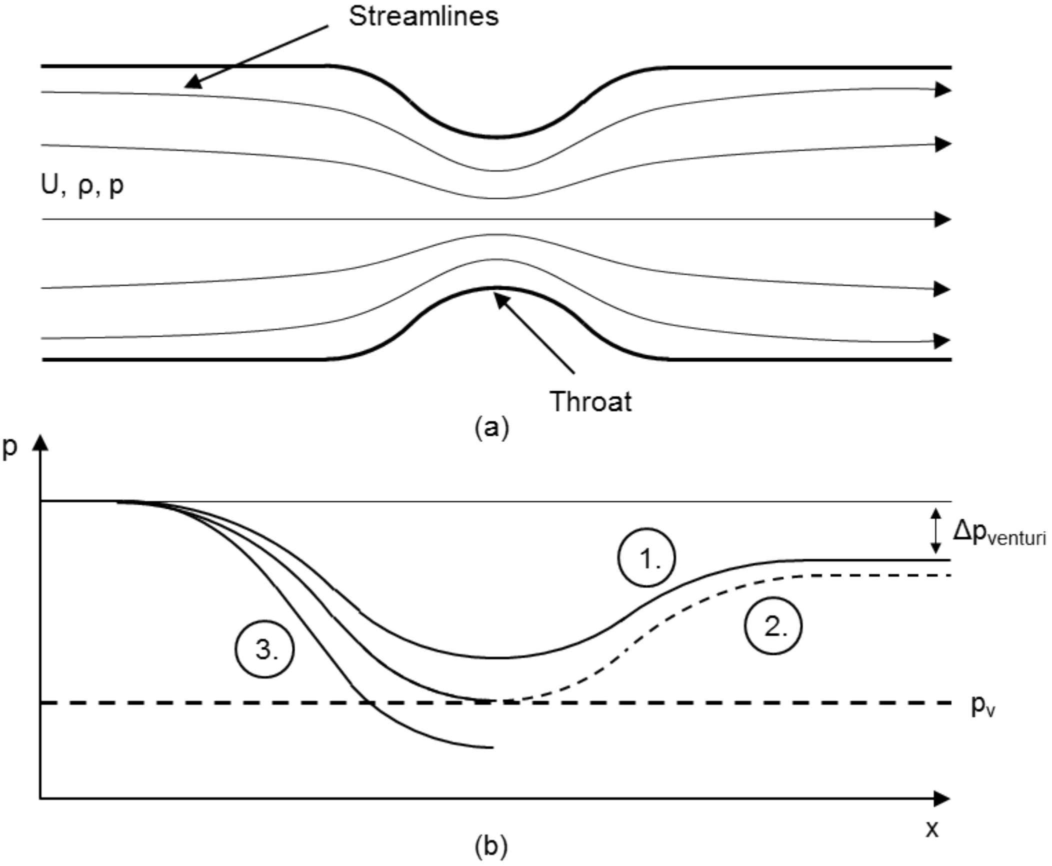

Figure 2.3: Schematic overview of a venturi with flow velocity U, density ρ and pressure p with corresponding streamlines (a). The corresponding pressure distribution for three different velocities is presented in (b). It can be seen that the lowest pressure occurs at the throat of the venturi. A non-cavitating flow is described by pressure distribution 1. In case of a venturi flow with a critical velocity, the pressure distribution is described by pressure distribution 2. The dashed line corresponds to the situation without cavitation. If cavitation inception take place by sufficient nuclei, vapor filled cavities can be seen. A cavitating flow is described by pressure distribution 3 and for this flow the pressure distribution after the throat is not presented due to unsteadiness.

venturi, the static upstream pressure (p_0) is build up. This p_0 (in combination with the lower downstream pressure) causes a flow, u_0, moving from the upstream to the downstream side. u_0 is already present in the cavitation number, as the stagnation pressure term. Furthermore, p_0 has nothing to do with the cavitation behavior on the downstream side of the venturi. For this reason the global static pressure of the system on the downstream side of the venturi is selected for p. For this definition, $p - p_v$ denotes the inverse of the driving force for cavitation generation. For high p, the driving force is low and no cavitation is expected. In case of low p, the driving force is high and cavitation is expected. This implies that cavitation intensity is increasing for decreasing cavitation number.

The vapor pressure of water, for a certain temperature (T), can be calculated with the Antoine equation:

$$\log_{10}(P) = A - \frac{B}{C + T}, \tag{2.4}$$

and is valid in a temperature range from -17.25 to 100 ° C for the following constants:

A = 4.6543;
B = 1435.264;
C = 208.302;

T is given in ° C and the corresponding output is in bar (equation adapted from Stull [37]).

In figure 2.3, a pressure loss, due to wall friction, is encountered. However, if cavitation is present, the encountered friction increases as function of cavitation intensity. In case of no-cavitation, wall friction losses are the main cause of hydraulic losses. In case of intense cavitation, even flow blockage can occur due to the complicated dynamics of the multiphase flow, according to Rudolf et al. [30]. Pressure losses can be described with the pressure loss coefficient, which is given by:

$$K \equiv \frac{\Delta p}{\frac{1}{2}\rho u_0^2}, \tag{2.5}$$

where Δp is the pressure drop over a certain distance, for example over the venturi. The density ρ and reference velocity u_0 are defined in the same way as in equation 2.3.

Periodic cloud cavitation shedding can be described with the Strouhal number based on the venturi throat diameter. Because the throat diameter is constant, this Strouhal number can be seen as a dimensionless frequency. This Strouhal number is defined as:

$$St_{d_t} = \frac{f d_t}{u_0}, \tag{2.6}$$

where the shedding frequency of the cavitation clouds is given by f. d_t is the venturi throat diameter and u_0 is the free stream velocity of the flow at the venturi throat.

In cavitation literature, there is also another definition of the Strouhal number. In this Strouhal number, the throat diameter d_t is replaced by the cavity length at the time of detachment (l_0). The shedding frequency can also be seen a characteristic time scale ($1/f$, which is required for a cavity development to the time instant of detachment. Combination of this time and length scale, gives a characteristic velocity schale: the integral cavity growth velocity ($u_{cav} = f l_0$. This cavity growth velocity is non-dimensionalized with the free stream velocity at the venturi throat (u_0):

$$St_{l_0} = \frac{f l_0}{u_0} = \frac{u_{cav}}{u_0}. \tag{2.7}$$

The final dimensionless parameter is the Mach number, this number describes the ratio of flow velocity, u to the local speed of sound (c):

$$M = \frac{u}{c}. \tag{2.8}$$

The speed of sound is rapidly decreasing when the vapor void fraction is increasing. The speed of sound in a bubbly flow can be approximated with the model of Minnaert [25]:

$$\frac{1}{c^2} = \Big(\rho_l(1-\alpha) + \rho_v\alpha\Big)\Big(\frac{\alpha}{kp}\Big) + \frac{1-\alpha}{\rho_l c_l^2}, \tag{2.9}$$

where c denotes the speed of sound, ρ_l and ρ_v denotes the density of liquid and vapor respectively. α is the air volume fraction, k is a certain constant, introduced by the polytropic relation. In isothermal bubble behavior this constant is unity and for adiabatic bubble behavior, k = 1.3. p is the pressure in the system and c_l is the speed of sound in pure liquid. For a complete derivation and corresponding assumptions, the reader is referred to the book of Brennen [3].

When a bubble collapses, the pressure field around the bubble is influenced. In 1917, Rayleigh [28] published a paper with an analytical solution for the pressure development around a single bubble during collapse. A pressure increase around the bubble boundary of 1260P is found, where P is the pressure in the far field. In the same paper the basis for the Rayleigh-Plesset equation is described, where the surface tension and viscosity was neglected. This Rayleigh-plesset equation describes the dynamics of a single spherical bubble in an infinite liquid volume. For an extensive study of this equation and cavitation dynamics, the reader is referred to the work of Franc and Michel [11]. A schematic analytical solution for the pressure field around a collapsing bubble as function of bubble radius is shown in figure 2.4.

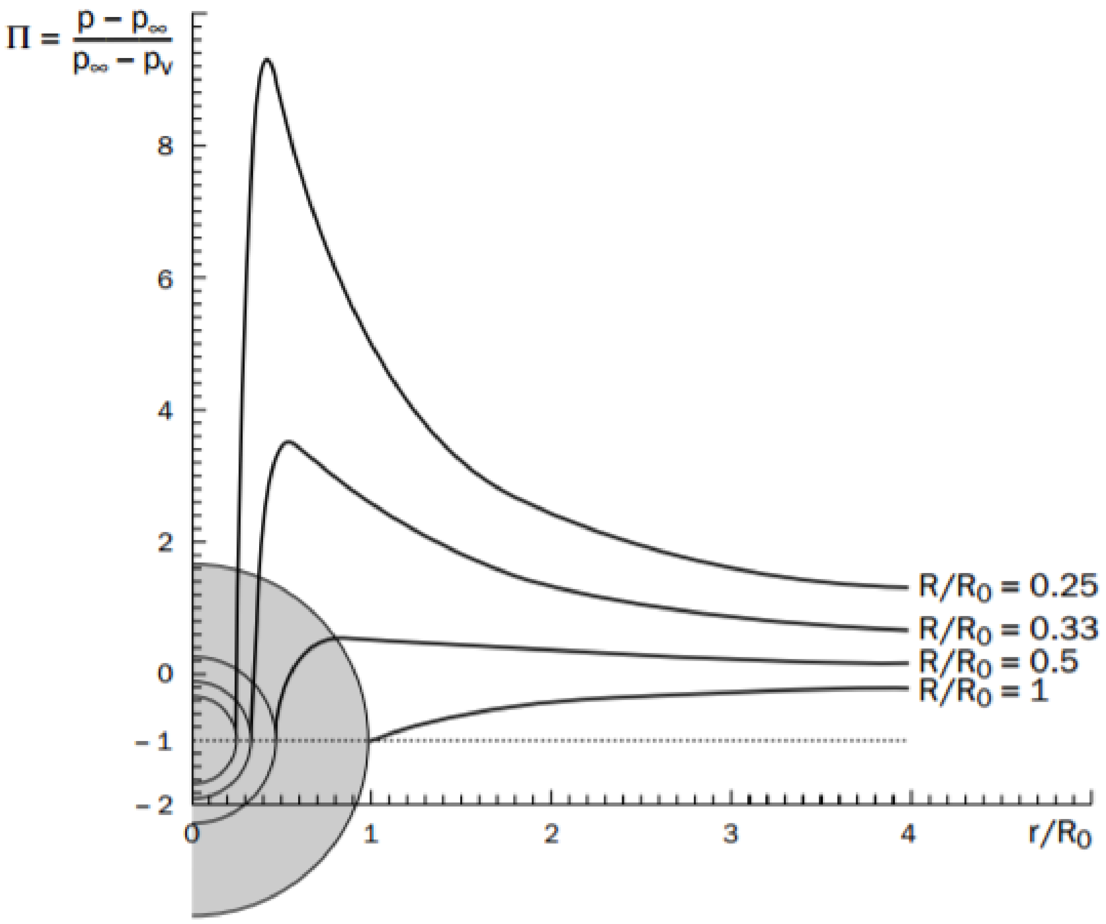

Figure 2.4: Non-dimensional pressure as function of bubble radius. It can be seen that during bubble collapse high pressures are generated. Figure reproduced from Franc and Michel [11].

2.3. Current state of the art

During the past decades, a lot of experimental and numerical research toward the different types of cavitation has been conducted. For this reseach several different geometries are used. An interesting geometrical shape is the Delft Twist-11 hydrofoil [42]. As the name already suggests, is this a hydrofoil with a non-constant angle of attack. On both ends, the angle of attack is 0° and at mid-span the angle is 11°. Through this shape a non-uniform pressure distribution is generated and hence vapor cavities are formed at low pressure locations. Due to this property, this hydrofoil is an ideal object for cavitation research and for model development and validation. Another geometry is based on cavitation in diesel injectors (see e.g. [35]). The combination of highly turbulent two-phase flow, small orifice shapes and large pressure gradients makes this a challenging field of research.

In paragraph 2.1 several cavitation regimes as function of flow velocity have been discussed. One interesting form is the unsteady shedding of cavitation clouds. Especially the mechanism that causes this unsteady cloud cavitation shedding is an intriguing field of study. Due to the complex mix of unsteadyness, two-phase flow dynamics, turbulent flow and structure interactions, this is a very complicated research field. Because of this combination, the focus has been on experimental research. For a certain combination of geometry dimensions and flow velocity this unsteady cloud cavitation shedding can be observed. To that end a wide range of measurement equipment is used, however the most prominent one is the application of a high-speed camera to observe unsteady cloud cavitation shedding. In previous research usually three different geometries are used in order to visualize this cloud shedding: in the first place 2D hydrofoils can be mentioned [5–7, 10, 27], secondly planar CD nozzles with rectangular cross-section (wedge) [13, 16, 39] and finally 1D axissymetric CD nozzles (venturi) [4, 30, 36]. Although in all geometries unsteady cavitation cloud shedding can be observed, due to the specific shape of each of the geometries, they all have their own characteristic flow dynamics. Generally, the venturies have the highest contraction ratio, due to their shape, which results in the ability of a wider cavitation range. The drawback of a venturi is the visualization of the cavity profile as function of time by optical techniques. This is the advantage of a wedge geometry with respect to the venturi geometry, caviatation profiles are easily visualized due to the 2D cavity profile.

Thus far in literature, three different mechanisms that initiates periodic vapor cloud shedding are described. In the first place, the re-entrant jet mechanism can be mentioned [20]. Secondly, the side entrant jet mechanism is proposed. This mechanism is very similar to the re-entrant jet mechanism. Side entrant jets are mentioned by Foeth et al. [10], Tomov et al. [39] and Ji et al. [17]. It is interesting to see that Foeth et al. [10] makes use of a twisted hydrofoil and Tomov et al. [39] makes use of a CD nozzle with a rectangular cross-section in order to observe the same mechanism. Foeth et al. [10] introduced the side-entrant jet term, in order to make distinction between the various directions of the re-entrant flow. The side-entrant jet is associated with the part of the re-entrant flow that has a strong spanwise velocity component. For the streamwise part of the re-entrant flow, the term re-entrant jet is used. Because of the similarity between the side entrant jet to the re-entrant jet, the side entrant jet is not discussed in further detail. The final mechanism that can be mentioned is the bubbly shock mechanism. In contrast to the re-entrant jet mechanism, this bubbly shock mechanism has only recently been presented (2015). Both the re-entrant jet and the bubbly shock mechanism are further explained and discussed in the next subsections.

Re-entrant jet mechanism

In 1955 Knapp [20] observed in a cavitating flow a re-entrent jet by means of high speed motion pictures. This re-entrant jet mechanism is very well presented in a schematic illustration proposed by Stanley et al. [36] and is shown in Figure 2.5. In this figure a nozzle wall is presented with a cavity growing on the left edge. Flow separation is caused by a (sudden) change in flow geometry (e.g. nozzle, tube bend etc.). A low pressure area is formed, at the location where the flow can not adhere to the wall. At this location, usually cavitation starts. In the total cycle time, T, different important points can be identified. At $t/T = 0$ a fully developed cavity (A) can be seen with a re-entrant jet (C) that starts traveling towards the attachment point. This re-entrant jet is caused by flow separation, and re-attaches at the nozzle wall after a certain distance from the separation point. Downstream the cavity, there is a relative high pressure with respect to the pressure in the cavity. The pressure in the cavity can be approximated by the vapor pressure. This pressure difference causes an adverse pressure gradient, which causes the re-entrant jet to travel towards the attachment point. The fixed cavity is disconnected from the venturi at $t/T = 1/3$. At $t/T = 1/2$ the vapor cavity (B) is advected with the flow and a new cavity (A) start to grow. The shedded vapor cloud (B) is further advected with the flow, coalesces and, a vortex ring is formed. In the end, at $t/T = 1$ the shedded vapor cloud (B) collapses and a new re-entrant jet (C) is generated.

After the visualization of the re-entrant jet by Knapp [20], a lot of research towards this re-entrant jet mechanisms has been performed. A summary of the most important performed research and the obtained results is given.

Different studies towards the velocity of the re-entrant jet have been conducted. Pham et al. [27] tried to measure the velocity of this jet by means of a surface electrical probe. At different foil positions the mean velocity of the jet was determined. A jet velocity with equal order of magnitude, as the free stream velocity, was found. It was also found that the velocity of the re-entrant jet increased with the distance with respect to the leading edge. They further observed that the frequency of the re-entrant jet, measured with the electrodes, was equal to the cloud shedding frequency, measured by pressure measurements. According to the authors this shows that the re-entrant jet drives the cloud caviatation shedding process. Also Kawanami et al. [19] investigated the influence of the re-entrant jet on the cloud shedding. In this study an obstacle was placed in the geometry, in order to prevent the re-entrant jet to proceed to the vapor cloud origin. The re-entrant jet could not proceed and vapor cloud shedding was not observed during this experiment. In this way they proved that the re-entrant jet is the cause of cavity cloud shedding. Sato and Saito [32] proposed that the re-entrant jet is a

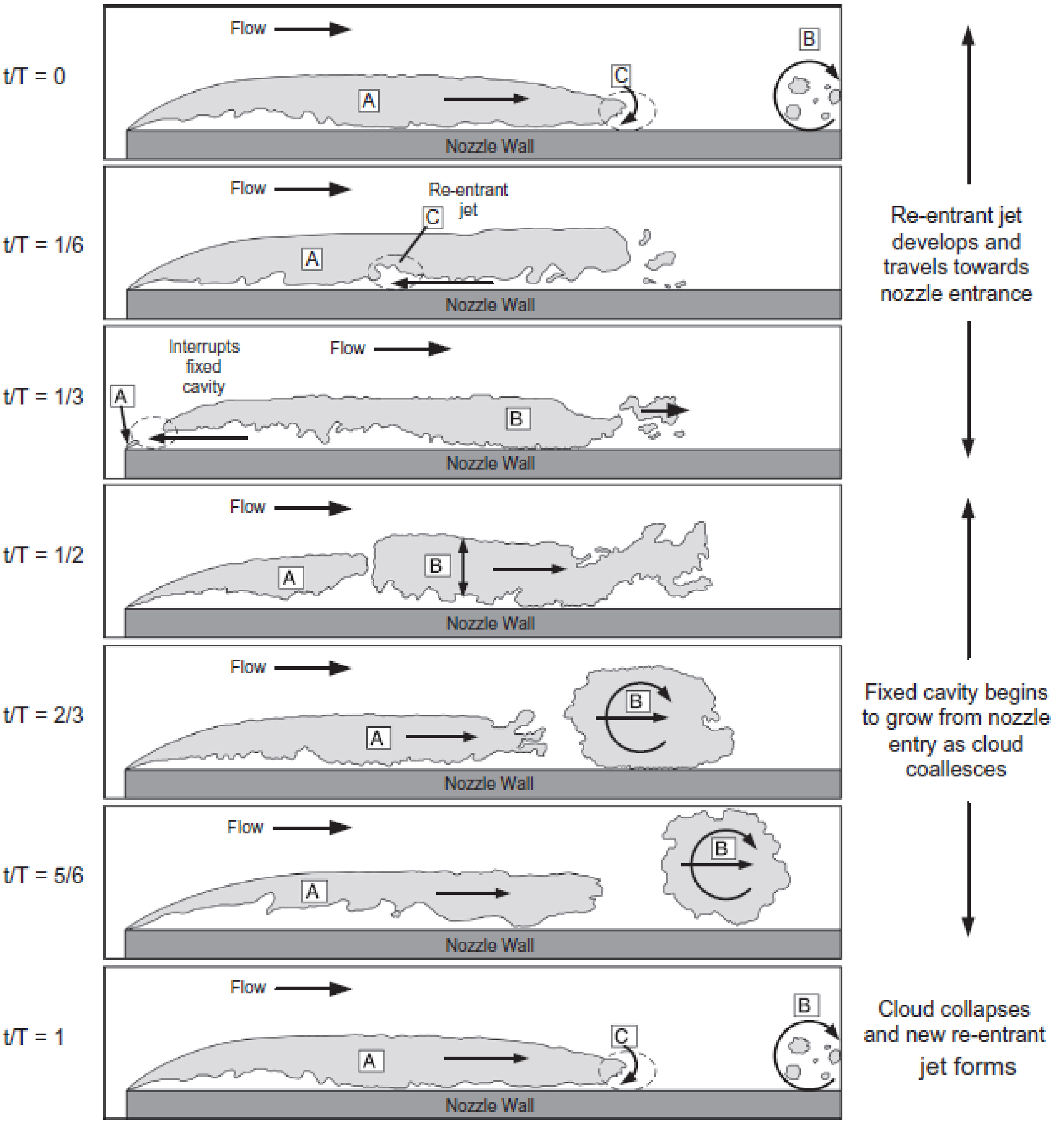

Figure 2.5: Schematic overview of the re-entrant jet dynamics from Stanley et al. [36]. In one total shedding cycle different important points can be identified. At t/T = 0 a fully developed cavity (A) can be seen with a re-entrant jet (C) that starts traveling towards the attachment point. This re-entrant jet propagates towards the attachment point and the fixed cavity is disconnected from the venturi (t/T = 1/3). At t/T = 1/2 the vapor cavity (B) is advected with the flow and a new cavity (A) starts to grow. The shedded vapor cloud (B) is further advected with the flow, coalesces and, a vortex ring is formed. In the end, at t/T = 1, the shedded vapor cloud (B) collapses and a new re-entrant jet (C) is generated.

consequence of the formation and coalescence of cavities on the separated shear layer [33]. Ink injection experiments in order to make the re-entrant jet motion visible were performed by Joussellin et al. [18], Le et al. [23] and Kawanami et al. [19]. Callenaere et al. [5] stated that two parameters are important for the re-entrant jet: the cavity thickness with respect to the re-entrant jet thickness and the adverse pressure gradient. This has to do with the friction losses that the re-entrant jet encounters in order to propagate to the leading edge. If the energy budget provided by the adverse pressure gradient is not sufficient to overcome these losses the re-entrant jet cannot proceed and the unsteady cavitation cloud shedding is not started. This clearly indicates that re-entrant jet cavity shedding is a pressure-driven phenomenon. Research towards the shedded cloud velocity was performed by Kubota et al. [21]. They studied the flow structures around unsteady cloud cavitation on a hydrofoil experimentally. To that end Laser Doppler Anemometry (LDA) with a conditional sampling technique was used. It was found that the convection velocity of this cloud is lower than the integral flow velocity. It was also observed that the vorticity or rate of rotation is increasing in the direction of the core of the advected cavitation cloud. A vorticity extremum was found at the center of the cloud. In the schematic presented in figure 2.5 also a rotational motion of the advected cavity can be seen. This rotational motion of the cloud is caused by the motion of the re-entrant jet.

Generally for the re-entrant jet driven cavitating flow a Strouhal number based on the cavity length in the range of 0.18-0.35 is found, irrespective if the flow is external (hydrofoil flow) or internal (venturi flow) [8, 12, 38]. See for the definition of the Strouhal number Equation 2.7.

Bubbly shock mechanism

The bubbly shock mechanism as initiator of the unsteady cloud cavitation shedding was first mentioned by Ganesh [12] in 2015. In this study time resolved X-ray densitometry was used in order to visualize the void fraction in the flow field. This in combination with a 2D cavitating wedge flow makes this a unique study. In a paper written by Ganesh, Mäkiharju, and Ceccio [13] the bubbly shock phenomenon is clearly explained and visualized. According to the authors this mechanism starts to play a role when the cavitation number is decreased and by that the void fraction in the cavity is increased. In this situation the shedding process is initiated by the bubbly shock mechanism instead of the re-entrant jet mechanism. This phenomenon can be explained as follows: at a certain moment, a well-defined void-fraction front can be observed in the cavity. This front spans the complete cavity height and moves with a certain velocity towards the wedge apex. If the void-fraction front reaches the wedge apex the fixed cavity is separated from the wedge apex and the vapor cloud is shed. Based on these observations, it can be argued that cavity shedding in the bubbly shock regime is shock-wave driven. For further details about the bubbly shock mechanism and the used measurement equipment, the reader is referred to the paper written by Ganesh et al. [13].

Tomov et al. [39] characterized the shedding frequency governed by the re-entrant jet dynamics with a frequency f_s and the shedding frequency corresponding to the bubbly shock mechanism with a frequency f_w. In an experimental venturi (2D) study, two different shedding frequencies were found for the same cavitation number. For a cavitation number of $\sigma = 1.23$, shedding frequencies of 47 Hz and 9.5 Hz were found for respectively re-entrant jet and vapor-shock wave induced shedding. It should be noted that in this case the cavitation number is based on the inlet venturi pressure.

Characteristic observations

With high speed imaging also different observations are presented. Some of them are characteristic for a specific geometry. In this paragraph a summary of some observations is given.

Sakoda et al. [31] performed research on a 2D hydrofoil and mention the occurance of 2 re-entrant jets in one cycle. Joussellin et al. [18], Stutz and Reboud [38] and Avellan et al. [1] noticed horseshoe vapor vortices at the liquid-vapor interface by unsteady cavitation on a hydrofoil. Brinkhorst et al. [4] found in a cavitating venturi, chaotic wave-like structures at the same interface. Tomov et al. [39] observed in a rectangular cross-section venturi a hairpin vortex occurring, during shedding of vapor cavities. This hairpin vortex is a vapor cloud that connects both cavitation regimes to each other. Thus far, this hairpin vortex is only mentioned in rectangular cross-section venturies. This is maybe due to a secondary flow pattern, which is present in a rectangular channel flow. Coalescence of individual shedded vapor clouds, before collapsing, is noted by Sato and Saito [32] in a circular-cylindrical orifice.

Especially in the axisymetric venturi very interesting and complex interacting fluid dynamics are present. Through the circular shape of this geometry an annular vortex ring is created which is interacting with the re-entrant jet, according to Rudolf et al. [30].

3

Experimental setup

In this chapter the experimental setup is described with the corresponding measurement systems and methods. In section 3.1 the experimental system is described with the used measurement equipment. The venturi is described in more detail in section 3.2. In section 3.3 the used highspeed imaging method is presented. Finally, the critical system pressure is determined, for which cavitation starts at the pump. This is discussed in section 3.4.

3.1. Experimental apparatus

A schematic overview of the experimental setup is given in figure 3.1.

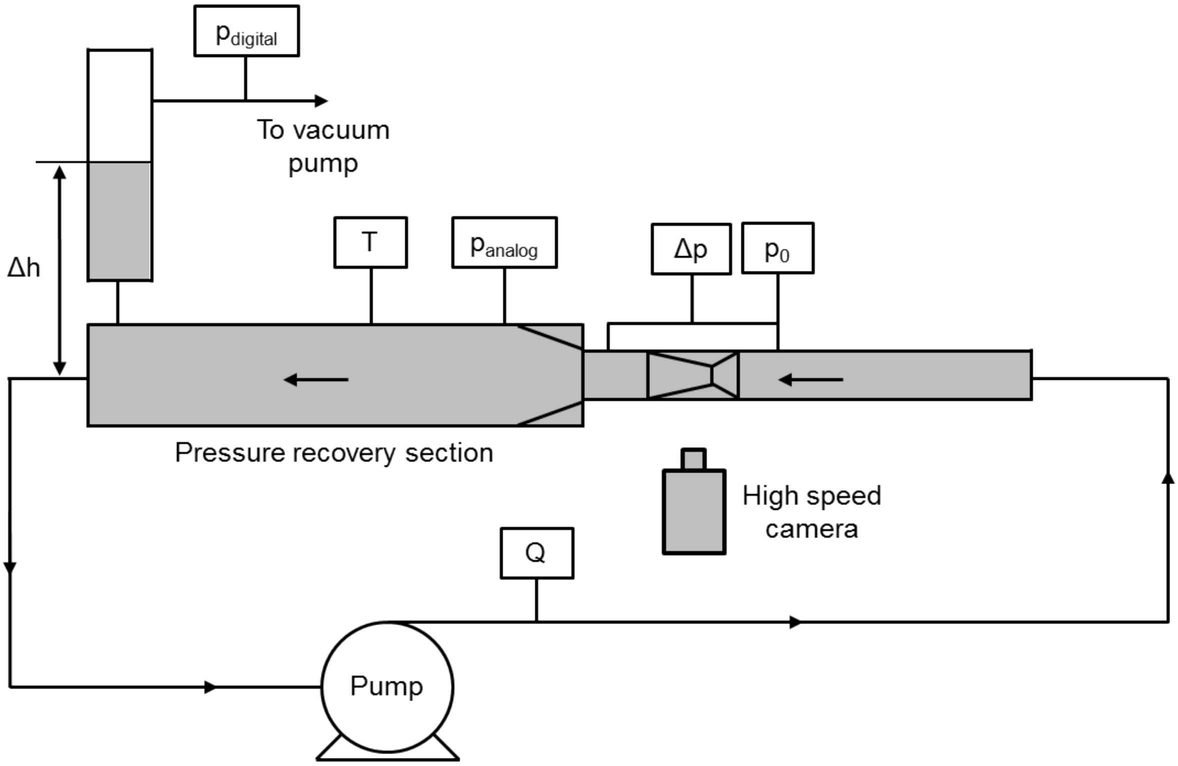

Figure 3.1: Schematic overview of the experimental setup. The setup consists of a centrifugal pump, an axisymmetric venturi, four pressure sensors, a temperature sensor, a flow meter, a high speed camera and a vacuumpump. The measurement data is processed with a PC.

The flow, in the closed loop system, is driven by a centrifugal pump (type: ICP3/80-200) which is installed at the lowest place in the circuit. This is done in order to ensure that cavitation does not occur

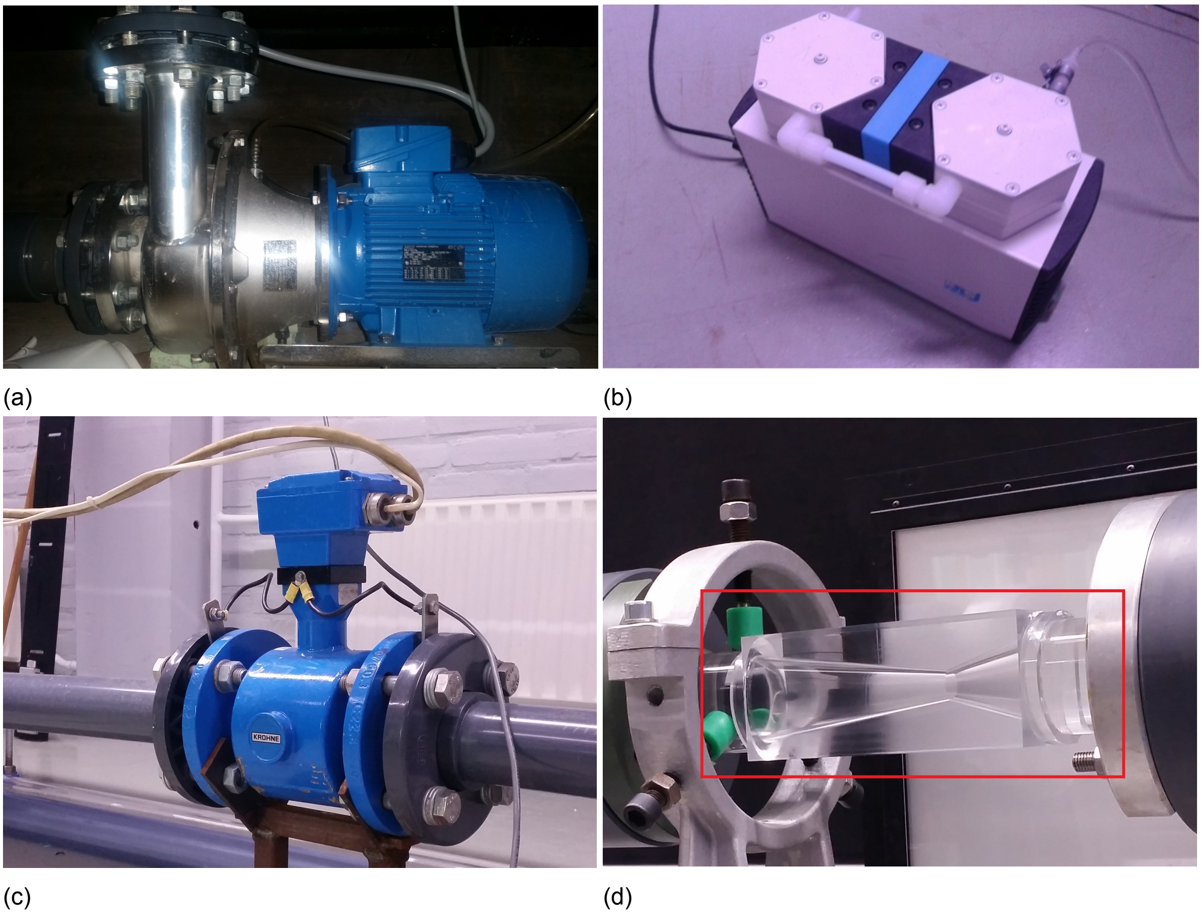

Figure 3.2: Images of different setup components. The used centrifugal pump is shown in figure 3.2a. The vacuum pump is displayed in figure 3.2b. The flow velocity is measured with the flowmeter depicted in figure 3.2c. Cavitation is studied in the venturi presented in figure 3.2d (red box). The flow direction is from right to left. On the background, the used illumination source (LED panel) can be seen.

at the pump impeller, but in the measurement section. This is elaborated in more detail in section 3.4. An image of the centrifugal pump is added in figure 3.2a. With this pump a flow range from 0 to 3.7 l/s is achieved, corresponding to an integral velocity range of 0 to 1.88 $\pm$ 0.4 % m/s in the pipe section in front of the venturi.

The flow rate is measured with a KROHNE flowmeter (type: IFS 4000F/6) and a corresponding signal converter of type SC 100 AS. A picture of this flowmeter is shown in figure 3.2c. The uncertainty in the velocity measurements is $\pm$ 0.4 % in case of a velocity > 1 m/s. If the velocity is < than 1 m/s, the uncertainty is given by $\pm$ 0.3% + 1 mm/s. Values are given in % of the flowrate.

The pipe section before the test section has a length of 2.0 m, which is 40d, in order to have a fully developed turbulent flow entering the test section [26]. Just before the venturi the initial or reference pressure, with respect to the ambient pressure, p_0, is determined by means of a Validyne DP15 differential pressure transducer (dpt) [9]. This dpt has an accuracy of $\pm$ 0.25% of full scale, which is translated in an uncertainty in the pressure measurement of $\pm$ 0.25 kPa. In addittion, the pressure transducer has an output of 3000 Hz. However, due to delay and damping in the system, the real sample frequency is expected to be much smaller. The same type of pressure transducer is used in order to measure the pressure difference over the venturi, denoted by Δp. The upstream pressure connection is 0.31 m before the venturi throat and the downstream pressure connection is 0.73 m after the venturi throat. Both pressure transducers are calibrated for a maximum pressure difference of 100 kPa and both calibration curves are attached in Appendix A. The venturi is discussed in detail in section 3.2. With a photron Fastcam APX RS high speed camera the flow in the venturi is captured. This camera is used in combination with a 105mm/2.8 FX AF MICRO-NIKKOR objective. The tube after the venturi has a length of 1.4 m.

There is a gradual transition from this tube to the pressure recovery section, with an angle of 5.7°, in order to avoid flow separation and minimize flow losses [41]. The length of this transition is 25 cm. After this transition, the pressure in the flow is recovered in a pressure recovery section, with an overall length of 1.92 m. In this section the pipe diameter is increased to 0.1 m, causing a maximum mean flow rate of 0.48 m/s. In this pressure recovery section, an analog pressure sensor is placed. Furthermore, a temperature measurement is performed, in the pressure recovery section, by means of a pt100 temperature sensor. With this temperature the vapor pressure of the water flow is calculated by means of the Antoine equation as defined in equation 2.4. At the end of the pressure recovery section a vertical water column is added, basically for two purposes. The first aim is to collect the air bubbles that are originally present in the system or that are generated by cavitation. These air bubbles assemble in the highest place of the setup, which is at the top of the vertical water column. The second purpose of this column is to be able to vary the global static pressure in the flow loop. A height Δh causes a hydrostatic pressure increase in the flow loop, and by means of a vacuum pump the global static pressure in the flow loop can be decreased. The global static pressure can be controlled from 110 kPa to 15 kPa, however, the system starts sucking in air for $p < 40$ kPa. A KNF Neuberger N840.3FT.18 vacuum pump is used, which can be seen in figure 3.2b. The pressure above the free surface is measured with an absolute digital pressure sensor (type: Barocel 600AB). The uncertainty of this sensor is 0.15 % of the reading. After pressure recovery section, the flow loop is closed.

Before and after each experiment the oxygen content in the experimental setup is measured with a RDO Pro oxygen sensor (from In-Situ). The accuracy of this sensor is ±0.1 mg/l for 0 to 8 mg/l; ±0.2 mg/l for 8 to 20 mg/l and ±10 % of reading for 20 to 50 mg/l. The resolution for the RDO Pro is 0.01 mg/l and the response time is 60 seconds.

The setup is filled with common tap water in order to perform the measurements. The total volume of the system without the vertical column is 60 L. A certain procedure is followed to fill the setup. At the same level of the pump, a vessel is filled with tap water. This vessel is connected with a tube to the system, at the exit of the pressure recovery section. By activating the vacuum pump, the water in the vessel is sucked in the setup. After the filling procedure, the setup is operated for a few minutes in order to stabilize the oxygen content in the setup. The pressurized tap water in the laboratory contains a supersaturated oxygen content as followed from measurements. The surplus oxygen content in the system assembles in the vertical column.

3.2. Venturi

A picture of the venturi can be seen in figure 3.2d. This venturi is made from polymethylmethacrylate (PMMA), which is better known as perspex or acrylic. The most important property of this material is the high light transmission, which gives the ability of optical access to the cavitation dynamics. The refractive index of this material is 1.49. The exact venturi geometry is presented in Figure 3.3, where the flow direction is from left to right. From figure 3.2d can be seen that the venturi is made from one rectangular piece of PMMA. There are four flat sides on the outside of the venturi, in to minimize the image distortion inside the venturi. In case of a round venturi outside, the image captured by the high-speed camera is much more distorted as follows from Snell's law. The two best finished, opposite sides of the venturi are oriented in the direction of the camera, in order to capture the cavitation behavior as good as possible. Usually, diffusers are designed in order to maximize pressure recovery. However, in this case a low pressure region is preferred for cavitation generation. A divergence angle of 16 ° is selected, in order to ensure flow separation and by that a low pressure region [41]. Furthermore, an area ratio of 1:9 (Area of the throat versus exit area) is selected. The inlet boundary layer blockage factor also influences the flow behavior in a conical diffuser [41]. Because the flow is converged before the throat, an almost smooth velocity profile can be assumed at the venturi throat. This implies that the influence of the boundary layer on flow separation is almost negligible. It is important to note that the behavior of the flow in the venturi is Reynolds number dependent [15]. Flow separation is enhanced for increasing Reynolds number.

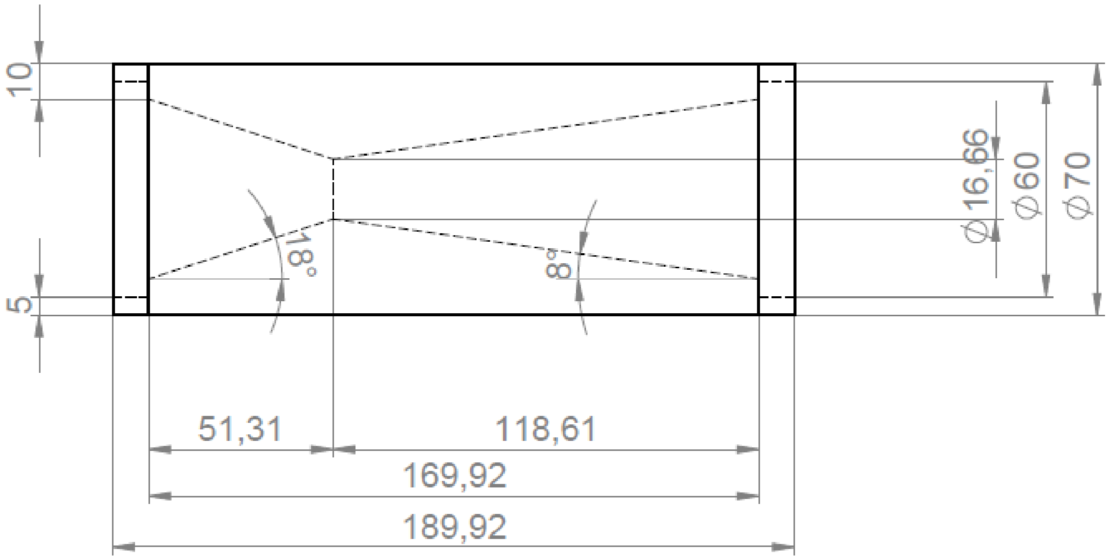

Figure 3.3: The exact venturi geometry, the dimensions are in mm. A divergence angle of 16 ° is selected, as well as an area ratio of 1:9. Flow direction is from left to right.

3.3. Highspeed imaging

The used method for capturing the cavity dynamics is shadowgraphy. A schematic overview of this method is shown in figure 3.4. In this method the measurement target is placed in between the light source and the (highspeed) camera. The light source illuminates the target from the back side in the direction of the camera sensor. Most preferably a homogeneous light source is used, for instance a LED panel, in order to minimize noise introduced by the light source. Every feature object that appear in the target blocks the light from the source behind. This results in a dark spot in the camera images. In this way the presence and position of vapor cavities can be determined.

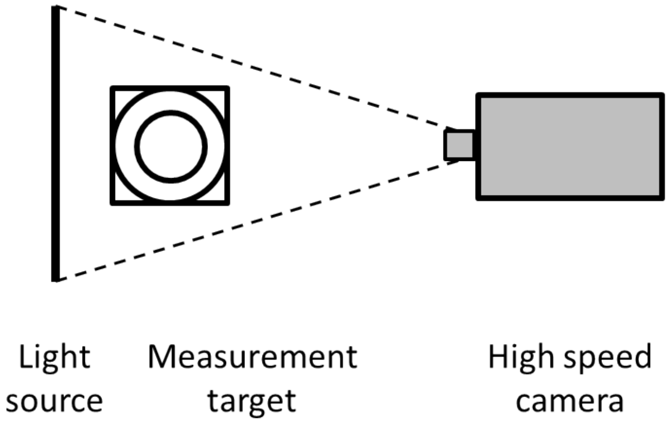

Figure 3.4: Schematic overview of shadowgraphy. In this method the measurement target is placed in between the (highspeed) camera and the light source. In this way the presence and position of vapor cavities can be determined.

3.4. Centrifugal pump

The Net Positive Suction Head (NPSH) of the pump is important, in order to avoid caviation in the pump. The maximum flow velocity in the setup is 1.7 m/s (with a tube diameter of 0.05 m), which corresponds to a flow rate of 12.0 m^3/h. According to the pump characteristics (added in Appendix B, figure B.1), the NPSH of the pump is 0.2 m. A safety heigth of 0.5 m is advised by Packo, the pump supplier. This implies that at least a NPSH of 0.7 m should be used for the minimum system pressure determination. The NSPH of the flow can be determined with equation 3.1 [41].

$$NPSH = \left(\frac{p_i}{\rho g} + \frac{V_i^2}{2g}\right) - \frac{p_v}{\rho g}, \tag{3.1}$$

where p_i and V_i are the pump inlet pressure and velocity. Further are p_v the vapor pressure and ρ the density of the liquid and g is the gravitational constant. For a temperature of 20° C, the vapor pressure is $2.3 \cdot 10^3$ Pa. For a maximum velocity of 1.7 m/s, a minimum pump inlet pressure, p_i = $7.7 \cdot 10^3$ Pa, is obtained. Taking the hydrostatic pressure (Δh = 2.75 m) into account, cavitation will definitely not occur at the pump.

4

Experimental procedure

In this chapter the experimental procedure is described. First of all the venturi is calibrated, this is described in section 4.1. In section 4.2 the best camera settings are presented. Finally the measurement procedure is described in section 4.3.

4.1. Venturi calibration

A calibration of the venturi is required for two reasons. The first reason is that the optical path through the venturi is distorted due to the difference in refractive index of the various substances (water, PMMP, air). The distortion in optical paths is translated in a distorted image of the cavity clouds, captured by the highspeed camera. The cavity lengths from the images are deviating from the real cavity lengths. The second reason is that a length scale or conversion factor can be determined from a calibration. This conversion factor (unit: px/mm) is required for the cavity length determinations.

For the calibration of the venturi a calibration grid is designed and produced. The schematic drawing of this calibration grid is presented in figure 4.1a. An image of the calibration grid in the venturi is presented in figure 4.1b. The two vertical black lines are o-rings, which are used for correct positioning of the target and in order to prevent damage to the venturi. With use of Matlab, the positions of the calibration points (+) are identified. A 3rd order polynomial in x and y direction is fitted through the identified calibration points. With this 3rd order fit, a transformation matrix is composed. The videoframes are multiplicated with this transformation matrix, which gives the calibration of the videoframes. The image of the calibration target in the venturi is also ”calibrated” with this fit. The result is shown in figure 4.1c. It can be seen that the crosses are located in a straight line (this is best visible by comparing the upper right vertical lines of crosses). However, it can be noted that the influcence of the optical distortion is almost negligible as can be seen from the difference between figures 4.1b and 4.1c.

In order to obtain the scaling relation from this calibration, the distances (unit: pixels) between the crosses is determined by means of Matlab. For the horizontal scaling the real distance between the crosses is 9.0 mm as can be seen in figure 4.1a. It should be noted that the third column (with crosses) from left is neglected in the callibration. This column was initially intended for better calibration in that region, but is not used because from the calibration follows (this is discussed in more detail in the next paragraph) that the resolution of the camera is the limiting factor. The averaged difference between every set of crosses is 70.33 $\pm$ 0.84 px (95 % confidence interval). This gives a scaling relation of 7.81 $\pm$ 0.09 px per mm in horizontal direction. For the first four (left) differences between the crosses, a difference in the range of 0.13 - 1.06 px is found, whereas the difference between the other crosses is uniformly distributed (0.03 - 0.13 px). The overall scaling of the original image is measured to be 7.78 pixel per mm, which is in correspondence with the obtained scaling relation. The same procedure is applied for the vertical scale and a scaling relation of 7.707 $\pm$ 0.334 pixel per mm is found (95 % confidence interval). This is in correspondence with the found horizontal scaling relation. It follows that the leading uncertainty is the uncertainty of the camera. This because from the calibration an uncertainty of 0.84 pixel is found, which is smaller than the resolution (1 pixel) of the camera.

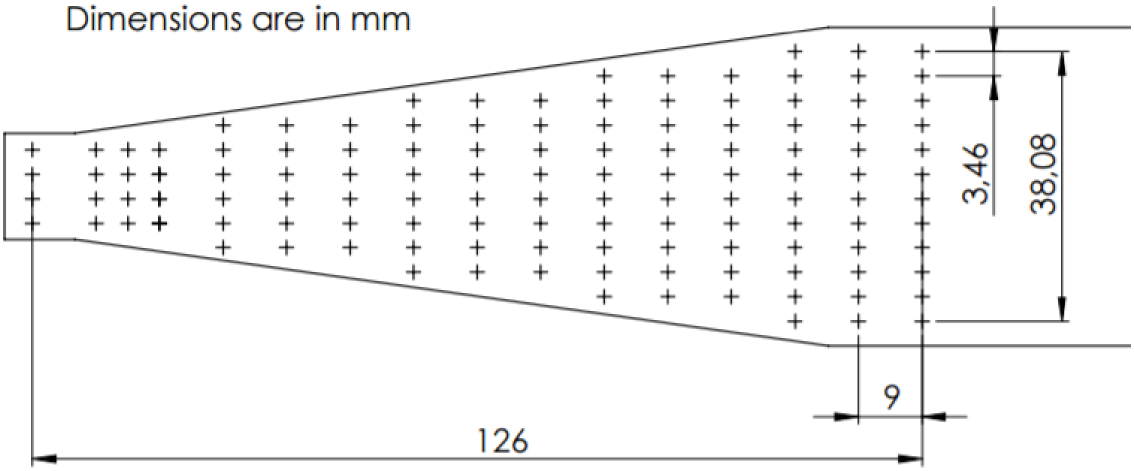

(a) Schematic drawing of calibration target with dimensions

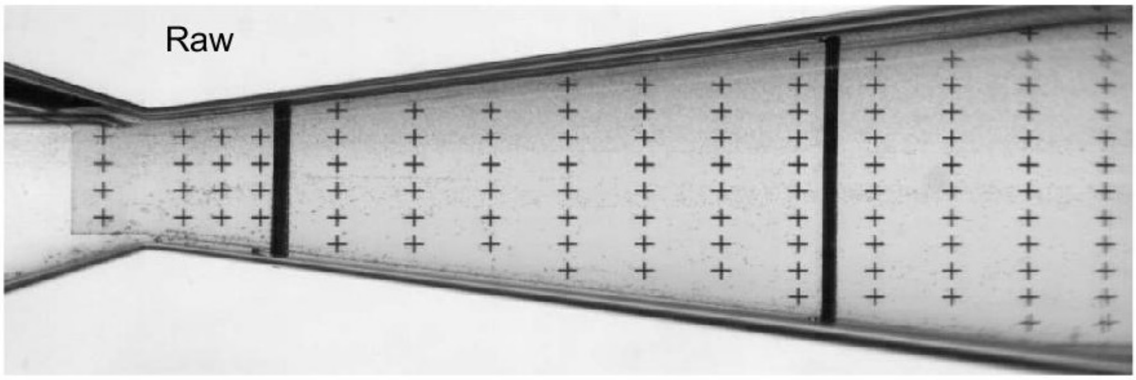

(b) Calibration target in the venturi

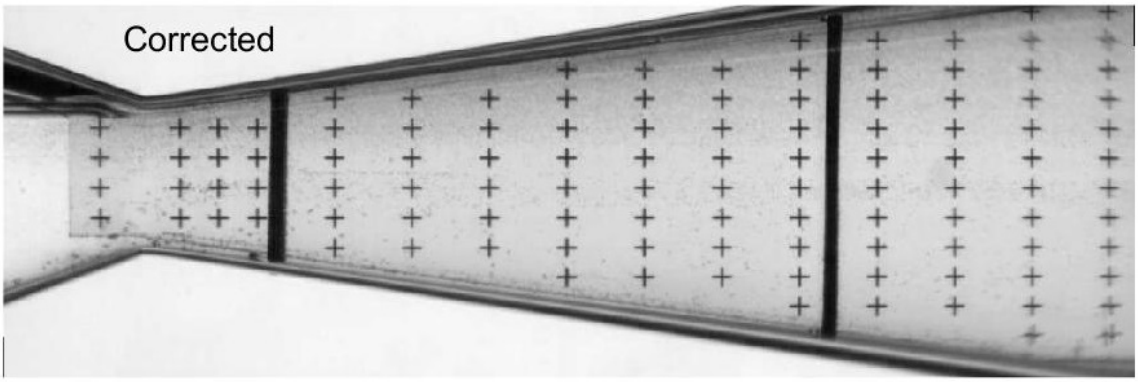

(c) The corrected calibration target image

Figure 4.1: Calibration targets

The performed calibration is a center or mid-plane calibration. This implies that all videoframes are corrected with a centerline based transformation matrix. However, the cavition clouds are not limited to the place of the calibration grid, but they are also on the front (curved!) side of the venturi, which is outside the calibrated plane. It should be kept in mind that this probably introduces some errors in the cavity length measurements.

4.2. Camera settings

A Photron Fastcam APX RS in combination with a 105mm/2.8 FX AF MICRO-NIKKOR object-glass is used to capture the cavitation dynamics. For the experiments two different camera modes are used, in both cases a diaphragm aperture $f^{\#}$ = 2.8 is used as well as a field of view of 1024x336 pixels. In the first case an exposure time of 1/9000 Hz is used in combination with a framerate of 800 Hz and a recording time of 4 seconds. This video is used for the determination of cavity shedding frequency. The sample frequency of 800 Hz is selected to meet the nyquist criterium, because a maximum shedding frequency of 300 Hz is expected. In the second case a framerate of 9000 Hz is used in combination with an exposure time of 1/framerate and a recording time of 0.1-0.15 seconds. This video is used for the cavity length determination. In chapter 5 is explained why this sample frequency is selected and how this is correlated with the uncertainty in cavity length determination. Digital change of the exposure time is selected to have the same video quality and to avoid manual change of the diaphragm settings during experiments. The distance of the camera, with respect to the venturi, is changed for the final two experiments in order to capture the cavity lengths. In both cases the cavity lenght was growing out of the field of view. It follows from the calibration that the image distortion is almost negligible, hence for the second calibration the overall venturi length is used. Based on this length and pixel difference, a scaling of 5.65 px/mm is found. Furthermore, the uncertainty is determined from the difference between the calibrated and the not calibrated target frame. By not calibrating the venturi, a systematic error of 3 pixels over the total venturi length (914 px) is introduced. The exact determination is added in Appendix A. In addition, the distance of the camera with respect to the venturi is enlarged (from 772 mm to 1068 mm). This results in a reduction of 1.38 pixels per mm field of view (less pixels are spread over the same area). Therefore, the systematic uncertainty introduced by not calibrating the venturi is 2.2 pixels or 0.39 mm. This is summarized in table 4.1.

Table 4.1: Calibration scales for different global static pressures.

Pressure (kPa)	Camera distance w.r.t. venturi (mm)	Calibration scale (pixel/mm)
50 - 110	772	7.81 ± 1.2 %
30 - 50	1068	5.65 ± 0.39 mm

4.3. Systematic data recording

In this section the measurement procedure is presented. Flow variables are measured as function of velocity and global static pressure. Because velocity is more convenient to adjust and set, for a fixed global static pressure a measurement series is performed, in which the flow velocity is varied. In order to minimize possible errors in the different measurements (series), measurements are performed according to a fixed protocol. This measurement procedure is stated below:

- Before each measurement series, a water sample is taken for the determination of the oxygen content in the system;
- Therafter, both pressure sensors are calibrated and possible air bubbles in the tubes are removed;
- The water level Δh is measured;
- The ambient pressure is determined, for determination of the inlet pressure p_0;
- The setup is operated for a few minutes before the measurement series is started, in order to mix the water in the system to obtain a uniform water temperature;
- The global static pressure of the system is set to a fixed, prescribed value and the measurements are started in case of a stable pressure reading;

- For the fixed, prescribed global static pressure, measurements are performed at different flow velocities;
- A measurement is performed when the flow velocity and the global static pressure are stabilized;
- By means of a LabView program the highspeed camera is triggered at the same time at which the sensor values are saved;
- After performing a measurement, the flow velocity is decreased in such a way that cavitation in the venturi is avoided, in order to prevent heating of the system. The pump has to overcome the friction losses in the venturi (due to cavitation), and heats the system rapidly in case of high friction. The transfer of the highspeed video to the PC takes a few minutes. If the flow velocity is sustained, a temperature increase of 1.2°C was found during data transfer of one measurement. In this case the cavitation number was 0.77;
- When all measurement points are performed a second series at the same global static pressure is performed, in which the 9000 Hz videos (for the cavity length determination) are recorded;
- In the end, the oxygen content is measured again by taking a water sample from the setup.

5

Data and data processing

In this chapter the processing of the acquired data is presented. This data can be roughly divided in two parts: video data and LabView data (i.e. pressure and temperature sensor data and flow rate data). From the high-speed videos four important parameters can be derived: the shedding frequency, the cavity growth rate as well as the advection velocity and the cavity length at the point of detachment. The extraction of these parameters from the high speed videos is explained in section 5.1. In this section also an uncertainty analysis is given on the shedding frequency and cavity lengths. The processing of the other part of the data (sensor data) is discussed in section 5.2.

5.1. Videodata

The cavitation dynamics following from the highspeed videos can conveniently be presented in a position-time diagram, or a so-called x-t diagram. This diagram is generated by taking a single videoframe as can be seen in figure 5.1a. It should be mentioned that the flow statistics are axisymmetric. Hence, the 2D video data captures the complete 3D cavitation dynamics. The videoframe is masked in such a way that only the centerline (Y/H = 0.5) with a certain bandwith is retained. The masked videoframe is presented in figure 5.1b. The retained bandwith is averaged in Y direction, in order to filter out local disturbances. In this way, a centerline averaged cavity cloud is obtained and this information is written to a new matrix. The global position of the cavity cloud is saved for the time instant of the image. The masking procedure is repeated for every next videoframe (read: timestep) and in this way a new matrix is built: the x-t diagram. In this diagram the global position of every cavity is saved as a function of time. This diagram contains the cavity information of one video in one image, as can be seen in figure 5.2. It should be emphasized that the colors in the x-t diagram are inverted, so white means the presence of a cavity cloud and black indicates a liquid phase. From this x-t diagram several flow properties can be derived. In the first place the shedding frequency of the cavitation clouds can be determined. This is done by means of a Fast Fourier Transform (FFT) along the time dimension (indicated with line 1). The second variable that follows from this x-t diagram, is the cavity growthrate given by the inverse of the slope indicated with line 2. From the literature study in chapter 2 follows that the global cavity growth rate is given by fl_0. The advection velocity of the detached cavity can be obtained by the inverse of the slope indicated by line 3. The final parameter that can be determined from the x-t diagram is the cavity length (l_0) at the time instant of detachment. This is indicated with line 4. The determination of the shedding frequency and cavity length with corresponding uncertainties are discussed in more detail in the next two subsections.

Shedding frequency determination and uncertainty analysis

Before systematic measurements are performed, a system frequency analysis is conducted to identify the frequencies that are already present in the system, e.g. pump frequency. For this analysis the pressure sensor data is used, because of the limited memory of the highspeed camera. This analysis points out that in the region of interest (30 - 300 Hz) no frequency peaks were found. This analysis is added in Appendix A.

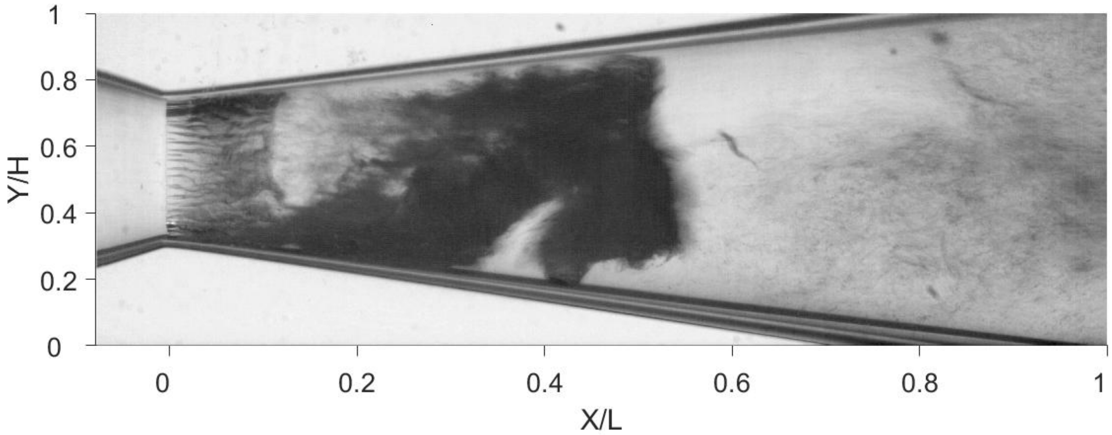

(a) Videoframe of the venturi with a (growing) cavity. The flow direction is from left to right. The darker region represents a vapor cavity, where the light regions represents a liquid phase.

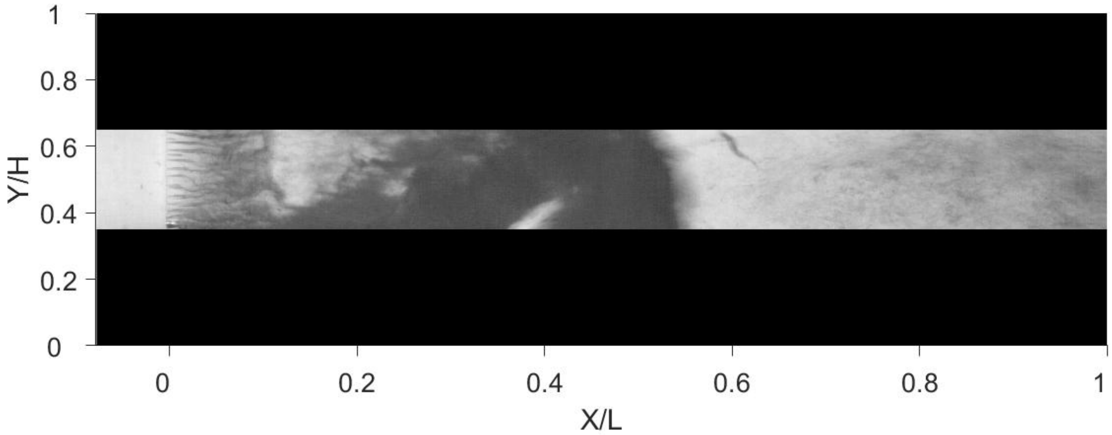

(b) Masked videoframe of the venturi with a cavity. The flow direction is from left to right.

Figure 5.1: Image masking procedure

Frequency determination

The shedding frequency of the cavity clouds is determined by means of a FFT in the x-t diagram along the time dimension. Different X positions can be selected at which the FFT is performed. In order to reduce noise in the final frequency m positions are selected, at which the frequency is determined. In the end the frequency is averaged over these m positions. The procedure for $m = 1$ is explained in more detail. A number of signal processing approaches are used for better frequency determination from this signal. In the first place, this signal is divided into n parts. Thereafter these parts multiplied with a hamming window, in order to account for edge effects. From each individual signal the power spectrum is determined by means of a FFT. All n powerspectra are averaged in order to reduce the noise that is present in one spectrum. From this powerspectrum the frequency, which contains the most power, is selected with two neighboring points on both sides. By means of a first order Gaussian curve fit through these five points, the resolution in the power signal is increased. A first order Gaussian fit gives the best approximation of the powerspectrum at the location of the maximum frequency (best R value). The frequency corresponding to the maximum point of this Gaussian is determined in order to obtain the final shedding frequency. In case of m positions, the frequencies are also averaged along the X dimension.

For the determination of the most suitable m positions, an initial analysis is performed. In figure 5.3 powerspectra at different X positions are presented. It should be noted that not all the power scales (vertical) are the same for every spectrum. From all subfigures it follows that the power peak around 200 Hz corresponds to the shedding frequency of the cavities. An important observation is that for X/L

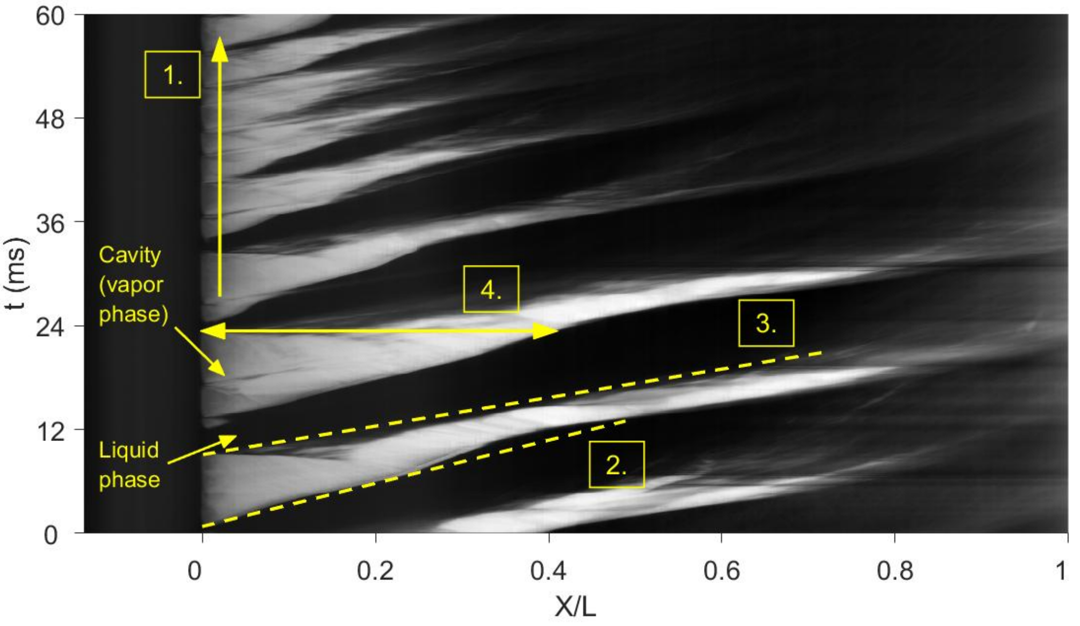

Figure 5.2: Cavitation dynamics summarized in a x-t diagram. Note that the colors are inverted with respect to the videoframes. White denotes the presence of a cavity (vapor phase) and black denotes the presence of liquid. The arrow indicated with 1. denotes the direction of the FFT for the cavity sheddin frequency determination. The dashed lines indicated with 2. and 3. are the cavity growth rate and the cavity advection velocity, respectively. The length, indicated with 4., is the cavity length at the point of detachment.

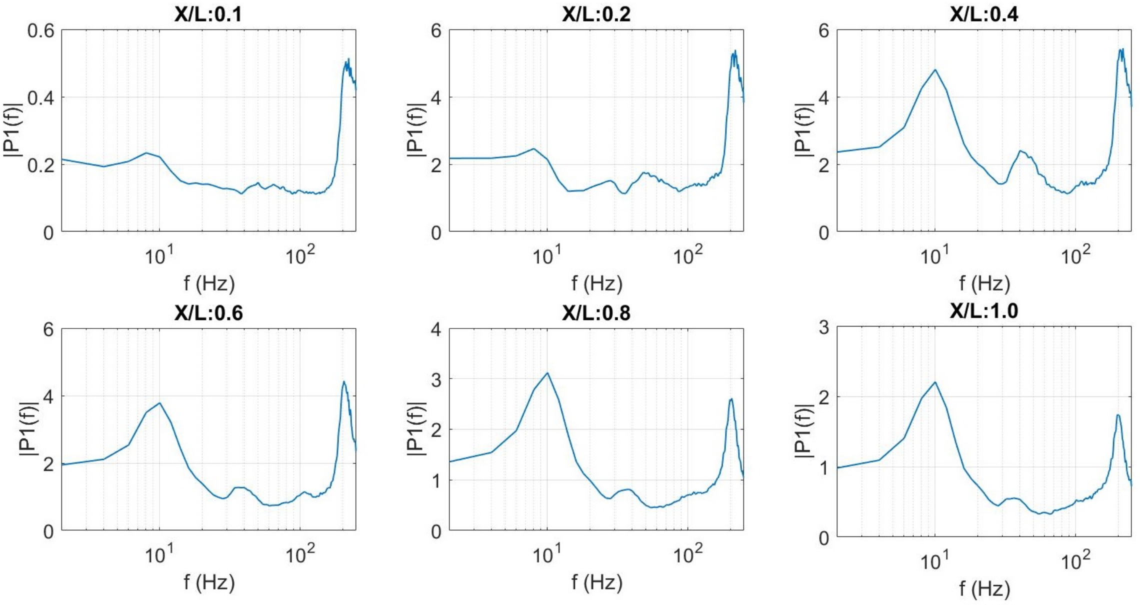

Figure 5.3: Powerspectra for different X positions. Note that the vertical scales are varying. The peak around 200 Hz corresponds to the shedding frequency of the cavity clouds. For X/L > 0.4 a low, unknown frequency component of 10 Hz starts to come in.

≥ 0.4 a low frequency component of approximately 10 Hz starts to come in. This frequency component is already present in X/L = 0.1 and X/L = 0.2, in the form of an almost uniform low frequency component. In the case of X/L ≥ 0.8, the power of this component is even higher than the power contained in the shedding frequency. The power in the frequency peak, corresponding to the cavity shedding frequency, is decreasing as function of time or position, simply because cavitation bubbles disappear. Based on this observation, the upper boundary for the position bandwidth is selected to be X/L = 0.2. The lower boundary is selected to be the start of the cavitation regime, which corresponds to X/L = 0. Between these boundaries m power spectra are selected, in this case m = 25. Following the above presented procedure for frequency determination, an average shedding frequency of 210.8 Hz is found.

The low frequency component in the powerspectrum at 10 Hz is still a mystery, because this frequency component is not captured by the pressure frequency analysis of the system. Two possible explanations can be formulated, in the first place can be thought of aliasing of a much higher frequency component, which is present in the system. For instance, this frequency can be the (aliasing of the) resonance frequency of the advected cavities. As second explanation can be argued that this is the frequency of the illumination source. A frequency analysis of the illumination source is performed, however, no frequency peak at 10 Hz is found. The result of this frequency analysis is added in Appendix A.

Frequency uncertainty analysis
A minimum signal length is required in order to obtain an accurate shedding frequency. To this end, a frequency uncertainty analysis has been conducted. A signal with $2.9 \cdot 10^4$ shedding cycles (overall frequency is found to be 214.7 Hz) is divided into eight parts, containing each $3.6 \cdot 10^3$ shedding cycles. It is assumed that these eight video parts are independent from each other because they are long enough and contain sufficient shedding cycles. From these eight videos the powerspectra (n = 100) are determined from which the prominent shedding frequency is derived. Based on the eight results a frequency of 214.3 ± 1.6 Hz is found, where the uncertainty based on $\frac{\sigma}{\sqrt{n}}$. In case of 36 divisions (n = 25), a frequency of 215.1 ± 1.1 Hz is found. It should be mentioned that n must be scaled with the total length of the data. In case of 72 divisions and n = 12, a cavity shedding frequency of 216.5 ± 0.7 Hz is found. This shows that, if n is scaled with the total length of the data, video lengths with 2 - 4 seconds are sufficient for accurate cavity shedding frequency determination.

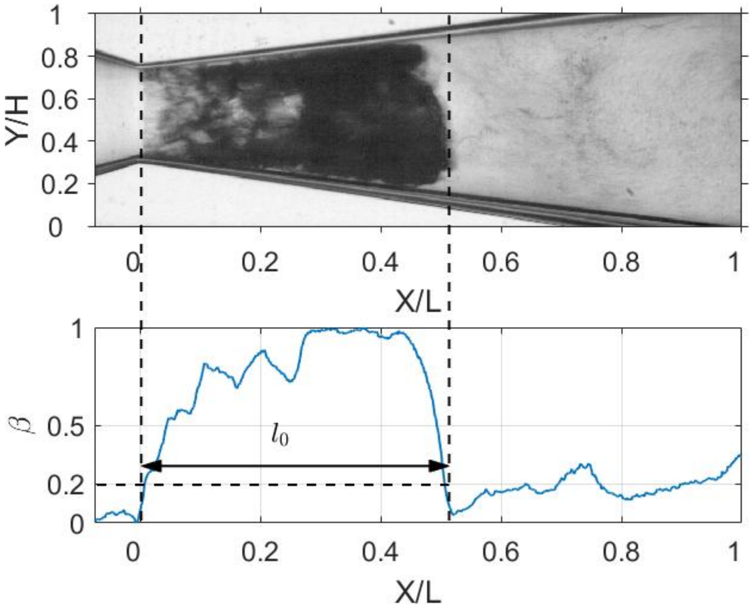

Figure 5.4: Image of cavity at time instant of detachment, with corresponding centerline averaged normalized grayscale β. The cavity length l_0 is given for a threshold value β = 0.2.

Cavity length determination and uncertainty analysis

In this section the method is described how the cavity length at the time instant of detachment is determined from the videodata. With use of the x-t diagram the time instant, at which the cavity detaches, can be easily approximated (figure 5.2, point 4). The centerline averaged normalized grayscale signal, β, corresponding to a cavity at time instant of detachment, is shown in figure 5.4. First, the throat position of the venturi is determined. At this position the cavity starts to develop. Application of a threshold at a certain β, for instance β = 0.2, gives an intersection between the grayscale of the cavity end position and this threshold. This intersection point minus the cavity throat position, gives the cavity length at time instant of detachment. In order to decrease the uncertainty in the cavity lengths, this procedure is repeated for five different cavities, which are averaged.

One could imagine that the sample frequency of the highspeed camera influences the accuracy of the cavity length determination: if the sample frequency is too small, the exact time instant of cavity detachment is not captured. This is visualised in figure 5.5, where three different grayscale profiles at different time instances are compared. The vertical dashed line corresponds to the throat position. In the first figure, the front position of the still growing cavity, can be seen at X/L = 0.42. In the second figure, the cavity profile at time instant of detachment is shown, where the cavity front position is at X/L = 0.47. In the final figure, the cavity is detached, and a new cavity can be seen, as indicated in the figure. The cavity front position in this case is given by X/L = 0.54. If the sample frequency is chosen too low, the center figure is not captured, and the cavity length is given by either the left or the right figure. This results in an under or over estimation of the cavity length. To this end, an analysis is performed for the change in cavity length between different time frames for different sample frequencies. This result is summarized in table 5.1. It can be seen that the uncertainty is decreasing for increasing sample frequencies as expected. From this follows that the error is proportional to the uncertainty multiplicated with the sample rate (e ∝ U · sample rate). For a sample frequency of 800 Hz, the error is 6.9 mm, which results for starting cavity lengths of approximately 14 mm in an error of 50 %. Hence the best available sample frequency of 9000 Hz is selected, which results in an error of 4 % for the smallest cavities. This error is decreasing for increasing cavity lengths and is less than 1 % in case of cavity lenghts l_0 > 0.061 m.

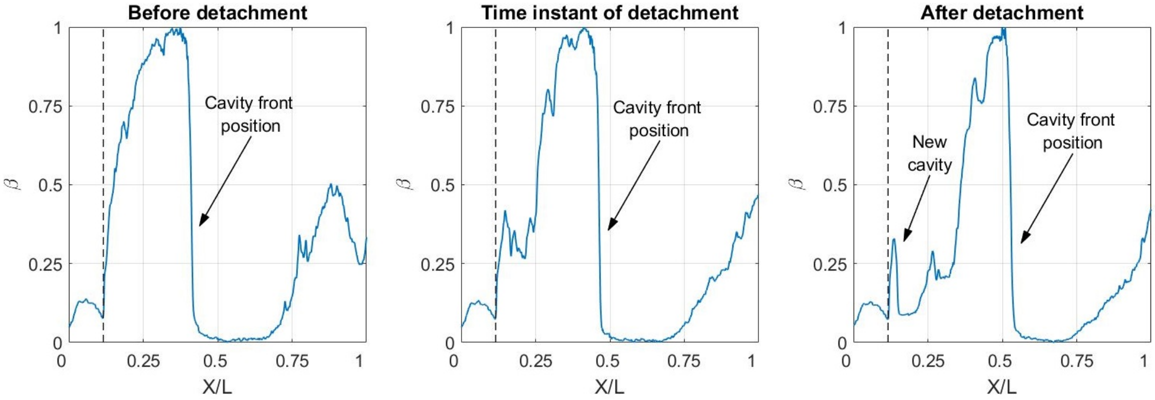

Figure 5.5: Grayscale index β for three different time instants. The vertical dashed line corresponds to the throat position.

Table 5.1: Cavity length uncertainty or cavity length shift for different sample frequencies.

Sample frequency (Hz)	Uncertainty (mm)
800	6.9
2400	2.3
7200	0.77
9000	0.61

5.2. LabView data

In this section the processing of the other sensor data is discussed. All the sensors (i.e. three pressure sensors, temperature sensor and flowmeter) are connected to a data acquisition system, from which all the readings are saved by means of a LabView program. The sample frequency of the sensors can be adjusted and set by the LabView program, and the same sample frequency is selected as the sample frequency of the highspeed camera. The camera is triggerd by the same LabView program and this trigger signal (block pulse) is added as a virtual sensor signal. The sensor data is saved from the index of the upgoing ramp of the block signal, which corresponds to the initial videoframe. In this way the pressure data is in correspondence with the videodata. With use of Matlab, the datasets are time averaged. The different non-dimensional numbers are based on these time averaged data and the signals from the videodata.

6

Results and Discussion

In this chapter the measurement results are presented as well as a discussion of these results. First of all, an analysis of starting cloud cavitation shedding is presented in section 6.1. In this analysis the basic cavitation dynamics are explained. Subsequently, the flow blockage through cavity formation is discussed in section 6.2. In this section also the typical cavity length scales are presented. The cavity time and velocity scales are covered in section 6.3, where a shedding frequency analysis is performed. Based on the time and velocity scales the following hypothesis can be formulated: the cavitation number σ determines the mechanism for cavity shedding. In section 6.4 the cavitation dynamics are presented, based on the discussed results in previous sections. From a physical point of view, two different cavity shedding mechanisms can be distinguished. These mechanisms are the re-entrant jet and the bubbly shock mechanism, which are respectively discussed in sections 6.5 and 6.6. This chapter ends with an introduction towards shear or jet cavitation in section 6.7.

6.1. Analysis of starting cloud cavitation shedding

In this section the basic cavitation dynamics, following from experimental observations, are discussed. To this end a complete cavity growth event is presented in figure 6.1. In 6.1a three different events can be distinguished. The first event is indicated with an A and represents an incipient cavity. A ring-shaped cavity can be observed at the venturi throat, in the vicinity of the venturi wall. This ring-shaped form can be explained from the fact that the highest flow velocity is found near the venturi wall at the throat. The highest flow velocity at the venturi wall is caused by the most contraction (of the streamlines) in this wall region, due to the shape of the venturi. This results in the lowest pressure in that regime, where vapor pockets are formed, when this pressure drops below vapor pressure. The second event is indicated with a B. Here a shed cavity can be seen, which is advected with the flow. The third event can be seen in the region indicated with C. At this place, still some bubbles can be seen that are remaining from a (partially) collapsed cavity. In figure 6.1b it can be seen that the cavity connected to the throat (A) is developing and a further advection of the detached cavity (B) can be remarked. In figure 6.1c the cavity denoted with A is still growing. The circular form of the cavity can be seen very well at the cavity front. A further observation is the partial collapse of cavity B, during this collapse complicated vapor structures can be observed. In figure 6.1d cavity A is detached from the throat and advected with the flow. A new cavity starts to develop at the venturi throat. A further collapse and advection of cavity B can be observed. In figure 6.1e the dynamics of cavity A are clearly visualized: during the advection of the cavity with the flow, a rotating motion of the cavity can be seen. The advection velocity, as well as the vortex motion, is indicated with arrows in the figure. In the final figure 6.1f the collapse of cavity A can be seen. During this collapse, a so-called horseshoe vortex is generated in the neighbourhood of the wall. This vortex is encircled in the figure. This horseshoe vortex is a very frequent phenonon in cavitating flows (see e.g. [1, 18, 38]), and is also found in numerical simulations (e.g. in a simulation towards cavitation on the twisted Delft hydrofoil by Ji et al. [17]). One cavity cycle can by summarized by the following: cavitation inception, cavity development, detachment with advection and a total collapse further downstream.

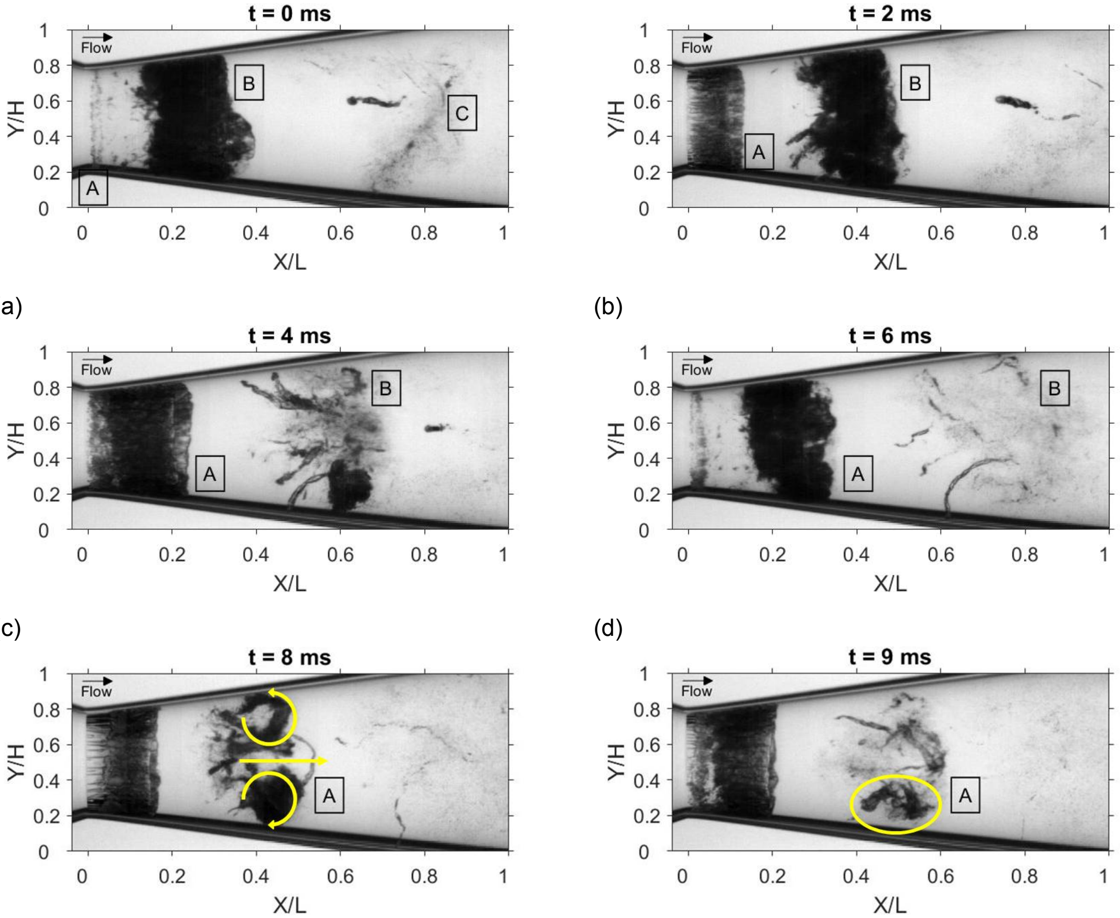

(a) (b) (c) (d) (e) (f)

Figure 6.1: Different video frames of a complete cavity growth event in the venturi. The flow direction is from left to right. Several events can be distinguished as function of time. A cavity cycle consists of caviation inception, cavity development, detachment and advection and finally a collapse. In this situation the cavitation number is σ = 1.00, which corresponds to a relative high global static pressure in combination with a relative low flow velocity.

6.2. Flow blockage through cavity formation

The intensity of the cavitation, presented in figure 6.1, can be described with the cavitation number as defined in equation 2.3. This situation is created with a relative high global static pressure and a relative low flow velocity, which results in a cavitation number of σ = 1.00. If the global static pressure is decreased in combination with an increasing flow velocity, the cavitation number decreases. More intensive cavitation is represented by a low cavitation number. For a decreasing cavitation number, the cavity length at the time of detachment is longer. This is schematically visualized for four different cavity lengths in figure 6.2. This figure is an approximation of the cavity behavior. It can be seen that the effective throat diameter is narrowed by the presence of the cavity, hence the throat diameter is a function of σ. Because of the narrowed throat diameter for decreasing cavitation number, a higher pressure loss over the venturi is encountered. This also follows from measurement results, where the cavitation number is varied and the pressure loss coefficient is measured, as can be seen in figure 6.3 (see for the definition of the pressure loss coefficient equation 2.5). For the definition of the cavitation number based on the global static pressure, all points are coinciding on one line. This implies that flow blockage (K) is only a function of cavitation number. The points corresponding to the global static pressure of 30kPa are deviating from the global trend, because air bubbles are entrained in the ciruit during the measurements at this pressure. A linear relation between the pressure loss coefficient and cavitation number is also found by Rudolf et al. [30]. The averaged cavity lengths at point of detachment are also measured as function of cavitation number, and are presented in figure 6.4. The cavity lengths are non-dimensionalized with the throat diameter (d) of the venturi. All measurement

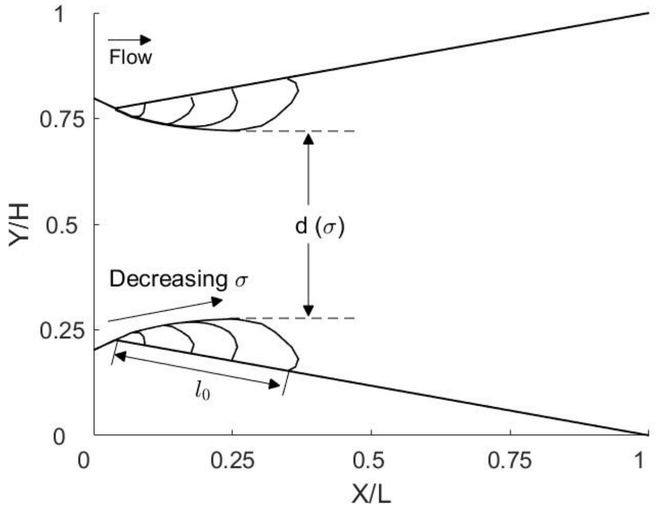

Figure 6.2: Schematic overview of the venturi with four different estimated cavity profiles at the time of detachment. The cavitation number is decreasing for increasing cavity length. The effective throat diameter is decreased by the presence of the cavities and is therefore a function of cavitation number.

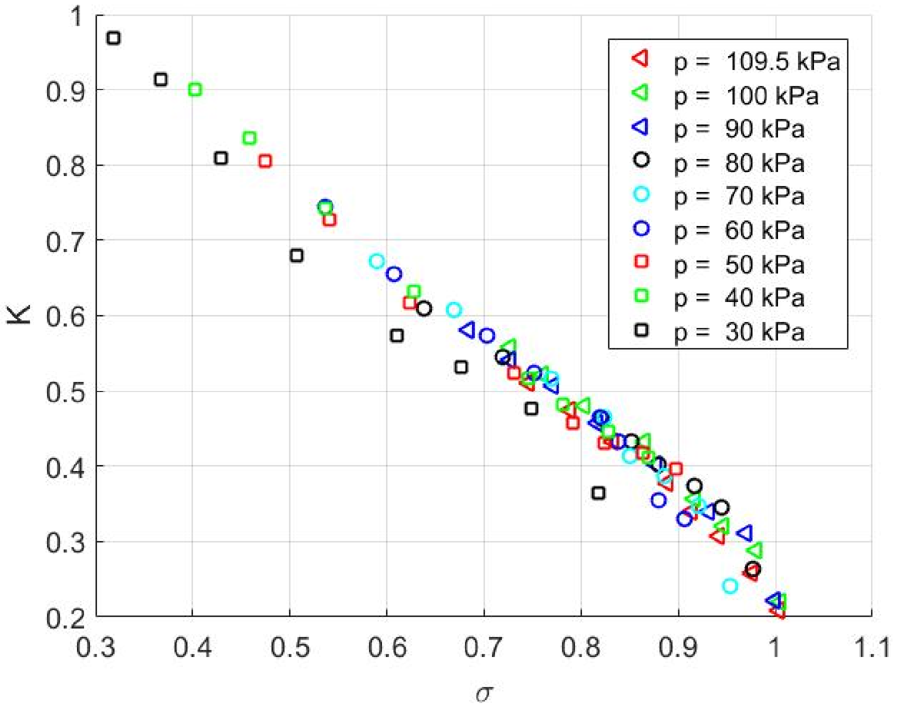

Figure 6.3: Pressure loss coefficient as function of Cavitation number. The cavitation number is based on the global static pressure. It follows for this definition that all points are collapsing on one line. This implies that pressure loss coefficient is a function of cavitation number only.

points are coinciding at one curve for the cavitation number based on the global static pressure. For starting cloud cavitation shedding, the dimensionless cavity lengths are of order unity. For decreasing cavitation number, cavities grow longer before detachment, almost up to 12d in the most extreme case. It can also be observed that the cavity length is a non-linear function of cavitation number, contrary to the pressure loss coefficient in figure 6.3. In order to explain this trend and the underlying physics, first a closer look to the corresponding time scales, that are characteristic for this shedding process, is necessary.

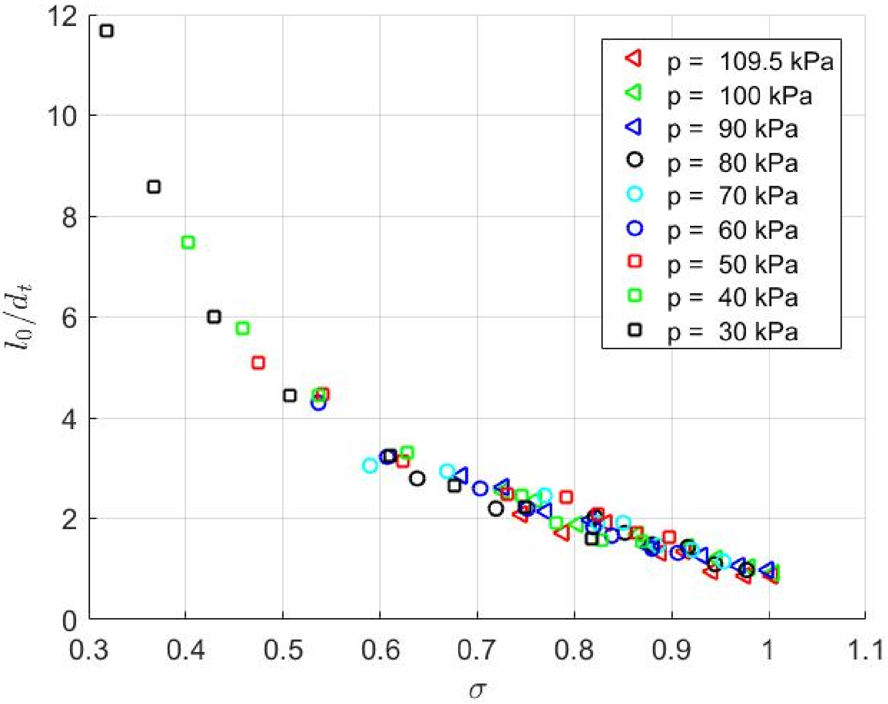

Figure 6.4: Cavity length, non-dimensionalized with the venturi throat diameter, as function of Cavitation number. For the cavitation number based on the global static pressure, all points are coinciding at one curve. Increasing cavity lengths can be observed for decreasing cavitation number, as already expected.

6.3. Cavity shedding frequency

From the shedding cycle shown in figure 6.1, one more parameter can be derived: the shedding frequency. Chapter 5.1 describes how this shedding frequency is determined from a x-t diagram. This shedding frequency can be presented in a non-dimensional form with the Strouhal number as defined in equation 2.6. The Strouhal number is also a function of cavitation number as can be seen in figure 6.5. It follows that all points are collapsing on one curve again. It can be seen that the shedding frequency is a non-linear function of cavitation number. Instead of looking to the Strouhal number as a dimensionless frequency, it can also be seen as a timescale of the cavity shedding process. This because the inverse of the shedding frequency gives the integral time scale, which corresponds to the process of cavity development to the time of detachment. Apparently, due to the characteristic shape of the curve in figure 6.5, a change in integral timescales can be observed for $\sigma \approx 0.8$. Multiplication of the integral timescale with the characteristic length scale at the time of detachment (see figure 6.4), gives the global growth rate of the cavity front. This global velocity scale is presented in a non-dimensional form, with the Strouhal number based on the cavity lenght (eqation 2.7). This Strouhal number is presented as a function of cavitation number in figure 6.6. This figure is a combination of the cavity length scale (figure 6.4) and the shedding frequency (figure 6.5). It can be seen that not all the points are coinciding at one curve, as in the case of the cavity length and time scales, but nevertheless a global trend can be observed. A global minimum, as well as the highest spread, can be observed for $0.8 < \sigma < 0.95$. Apparently, there is a certain transition where the characteristic cavity length and time scales are changing. For the same range in cavitation number, also the most spreading in cavity shedding frequency is found (see figure 6.5). According to the literature, a Strouhal number (based on cavity length) between 0.18 and 0.35 is found [8, 12, 39]. The main part of the Strouhal numbers is found to be in correspondence with these values. According to Ganesh et al. [13] the bubbly shock mechanism is observed for low cavitation numbers. Based on the found correlation and the result of Ganesh et al. [13] the following hypothesis is formulated:

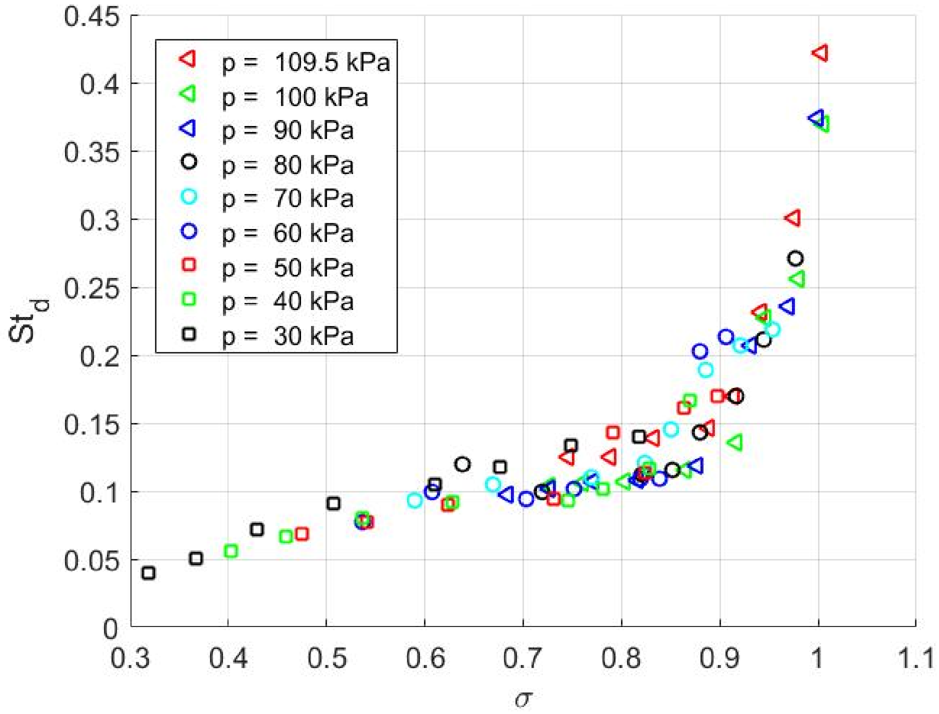

Figure 6.5: Cavitation number as function of the Strouhal number, which is based on the throat diameter. The cavitation number is based on the global static pressure. A change in time scale can be observed for $\sigma \approx 0.8$. A Strouhal number of 0.42 corresponds to a cavity shedding frequency of 370 Hz and the Strouhal number of 0.04 corresponds to a shedding frequency of 32 Hz.

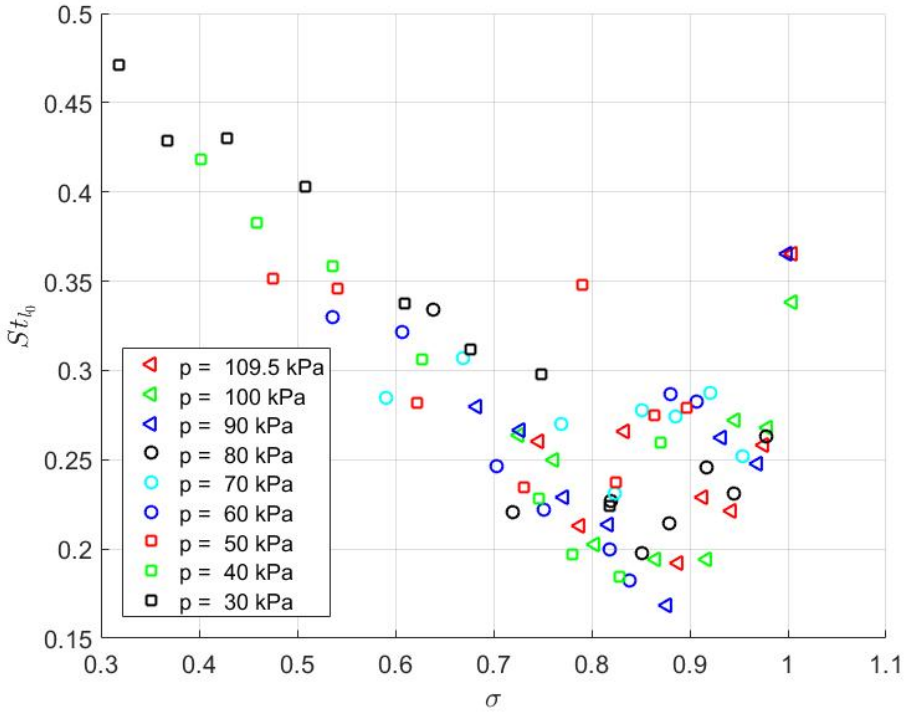

Figure 6.6: Cavitation number as function of the Strouhal number, based on the cavity length. The cavitation number is based on the global static pressure. A minimum in velocity scales can be observed for σ = 0.88.

Hypothesis: Two different cavitation mechanisms can be identified as function of cavitation number. For σ > 0.95 cloud cavitation shedding is governed by the re-entrant jet (i). For σ < 0.8 cloud cavitation shedding is governed by the bubbly shock mechanism (ii). The cavitation region in between is governed by both mechanisms (iii).

In order to accept or reject this hypothesis, a closer look to the cavitation dynamics at different cavitation numbers is necessary. In the next section an elaboration of the cavitation dynamics is given.

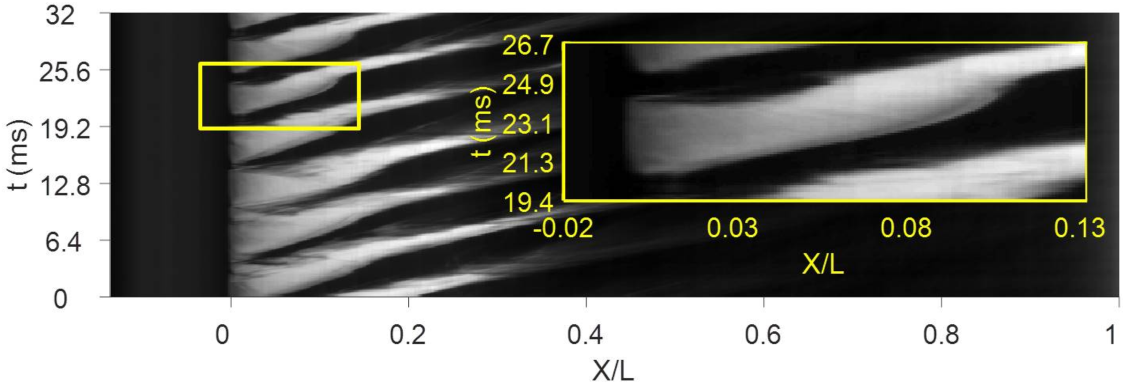

Figure 6.7: X-t diagram of a measurement point in the re- entrant jet regime. The white regions indicate the presence of vapor and the black regions indicate the presence of liquid. An enlargement of a typical shedding cycle is presented in the (yellow) box in the figure. For this case,s σ = 0.97 (corresponding to: u_0 = 13.5 m/s and p = 90 kPa) and Fs = 9kHz.

6.4. Cavitation dynamics

In this section the main proof of the hypothesis, which is formulated in the previous section (6.3), is given. From the literature study it follows that re-entrant jet is pressure driven, whereas bubbly shock is shockwave driven. In order to capture these physics, and to prove the hypothesis, cavitation fundamentals must be examined in more detail. The cavitation fundamentals are well presented in an x-t diagram, because in this diagram the cavity time and length scales are visualized in a clear way. The hypothesis consist basically of three parts, as indicated with Roman numerals. To that end three different x-t diagrams are examined, where each diagram corresponds to a part of the hypothesis.

First an x-t diagram for σ > 0.95 is examined in more detail, this corresponds to the part of the hypothesis indicated with (i). In this region the re-entrant jet mechanism is expected as prevalent mechanism for cavity shedding. To that end the x-t diagram corresponding to a cavitation number of σ = 0.97 (u_0 = 13.5 m/s and p = 90 kPa) is selected. This diagram is shown in figure 6.7. The white regions indicate the presence of a cavity (vapor) and the black regions indicates the presence of liquid. A typical shedding cycle is captured with a rectangular box and enlarged on the right side of the diagram. It can be seen that this cavity starts to grow at t ≈ 21 ms and grows linearly until a certain point. After that point the slope becomes steeper, indicating that the cavity front growth rate decreases. During this front velocity decrease, cavity detachment can be observed at t ≈ 25 ms. The back side of the cavity moves instantaneously from X/L = 0 to X/L = 0.05. This sudden detachment or condensation is possibly caused by an (higher) upstream pressure, which is built up during cavity development. After this sudden detachment, the vapor cloud is advected with a positive velocity. Furthermore, after detachment and partial advection, the cavity front velocity increases to a constant velocity (constant slope). This shedding cycle is characterized with stick-slip behavior, and is typical for the examined regime. This shedding behavior is associated with stick-slip, because the backside of the cavity sticks to the venturi throat and at a certain point this backside is suddenly detached, which is associated with slip. It should be noted that the re-entrant jet dynamics cannot be seen in the x-t diagram, due to insufficient contrast in this white region. However, the re-entrant jet can be observed by particle/bubble tracking in individual video frames, this is discussed in more detail in section 6.5.

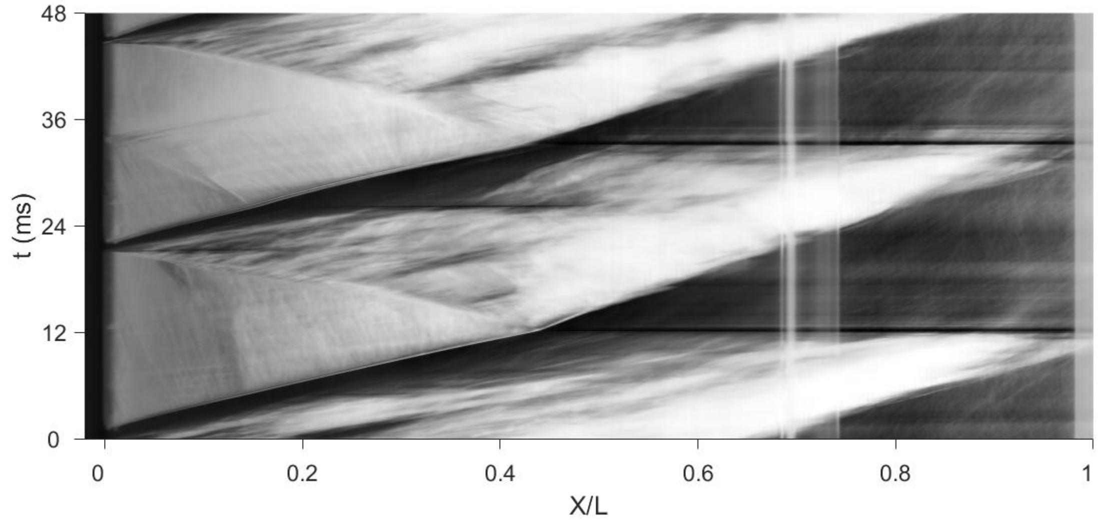

Figure 6.8: X-t diagram of a measurement point in the bubbly shock regime. The white regions indicate the presence of vapor and the black regions indicate the presence of liquid. Further is σ = 0.40 (u_0 = 13.7 m/s and p = 40 kPa) and Fs = 9kHz.

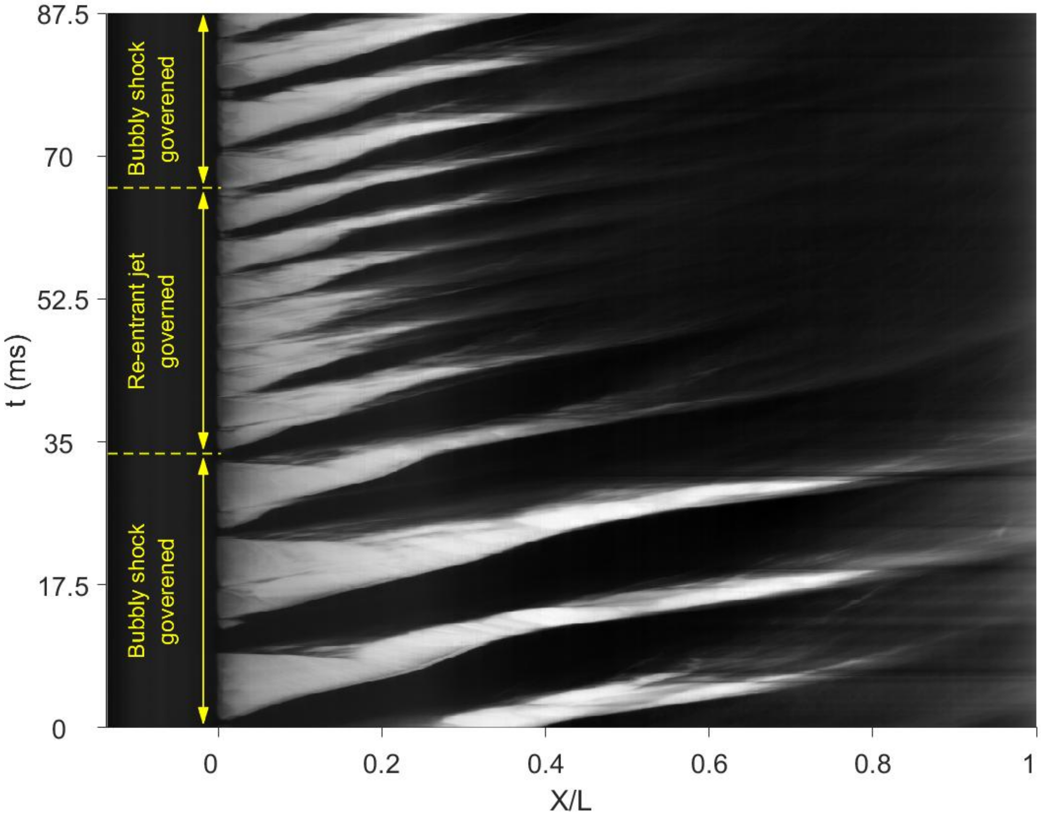

Figure 6.9: X-t diagram of a measurement point in the intermediate region. The white regions indicate the presence of vapor and the black regions indicate the presence of liquid. Bubbly shock induced shedding can be observed for 0 < t < 34 ms and 66 < t < 87.5 ms. Re-entrant jet governed shedding can be observed for 34 < t < 66 ms. Further is σ = 0.88 (u_0 = 14.2 m/s and p = 90 kPa) and Fs = 9kHz.

The second part (ii) of the hypothesis involves a case below transition (σ < 0.8). In this region the bubbly shock mechanism is expected as prevalent mechanism of cavity shedding. To that end an x-t diagram is selected, corresponding to a cavitation number of σ = 0.40 (u_0 = 13.7 m/s and p = 40 kPa). This diagram is presented in figure 6.8. It should be noted that in this figure the white region indicates the presence of vapor and the black region the presence of liquid. It can be seen that a cavity starts to grow at t ≈ 0 ms, with a constant growth rate (linear slope of the black-white interface). At t ≈ 12 ms a change in growth rate can be observed, this is exactly at the point where a black line (coming from the right) hits the cavity. This black line indicates that there is a liquid phase present in the venturi at this time. It can also be observed that above this black line, at X/L ≈ 0.8, the previously shed cavity cloud vanishes. It follows that, at the time of cavity collapse, a pressure wave is emitted in both directions. According to figure 2.4 in the literature study, high pressures are generated during vapor bubble collapse. The emitted pressure wave is propagating through the growing cavity, as can be seen from the density change in the growing cavity (white region). When the pressure wave reaches the venturi throat, the cavity detaches and is thereafter advected with the flow. This shedded cavity also collapses further downstream, emitting a pressure wave, which is the trigger mechanism for the next cavity detachment. In section 6.6 this mechanism is discussed in more detail.

Thus far two two typical cases are considered, where either the re-entrant jet mechanism, or the bubbly shock mechanism is expected as prevalent mechanism for cavity shedding. The final part (iii) of the hypothesis states that both mechanisms are occurring in the region where 0.8 < σ < 0.95. To this end an x-t diagram is selected, corresponding to a cavitation number of σ = 0.88 (u_0 = 14.2 m/s and p = 90 kPa), and is presented in figure 6.9. In this x-t diagram two different regimes can be identified, with a transition at t ≈ 34 and t ≈ 66 ms. For 0 < t < 34 ms and 66 < t < 87.5 ms emitted pressure waves can be observed, emanating from collapsing cavities. Although the pressure waves are not so evident as in the case of figure 6.8, they can still be identified as the trigger mechanism of (growing) cavity detachment. For 34 < t < 66 ms, the pattern changes and the characteristic form, corresponding with stick-slip behavior can be observed. This analysis shows that in the intermediate region indeed two alternating mechanisms can be observed.

The three examined x-t diagrams are the main proof for the hypothesis. Two different characteristic shapes can be distinguished in the diagrams. The stick-slip behavior, which is typical in the regime where the re-entrant jet is expected must be linked to the re-entrant jet. This is elaborated in more detail in the next section. The pressurewave is discussed in more detail in the section after.

6.5. Re-entrant jet dynamics

In this section the typical stick-slip shape found in the x-t diagram (see figure 6.7) for σ > 0.95 is related to re-entrant jet induced shedding. To this end an x-t diagram, as well as the corresponding video frames, are presented. In the videoframes bubbles are tracked. In order to be able to track these particles, the sample frequency is increased to 22.5 kHz. The x-t diagram of one shedding cycle is shown in figure 6.10.

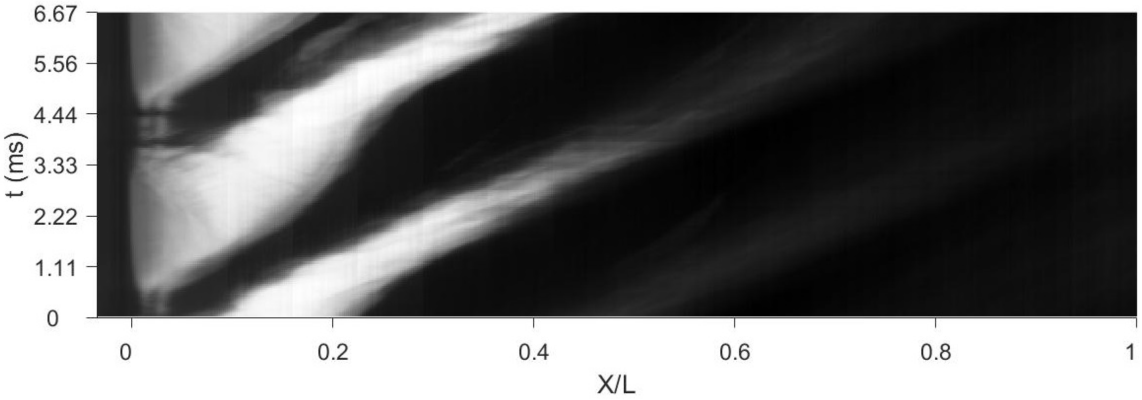

Figure 6.10: X-t diagram with a typical stick-slip shape. The white regions indicate the presence of vapor and the black regions indicate the presence of liquid. Further is σ = 1.00 (u_0 = 14.4 m/s and p = 106 kPa) and Fs = 22.5 kHz.

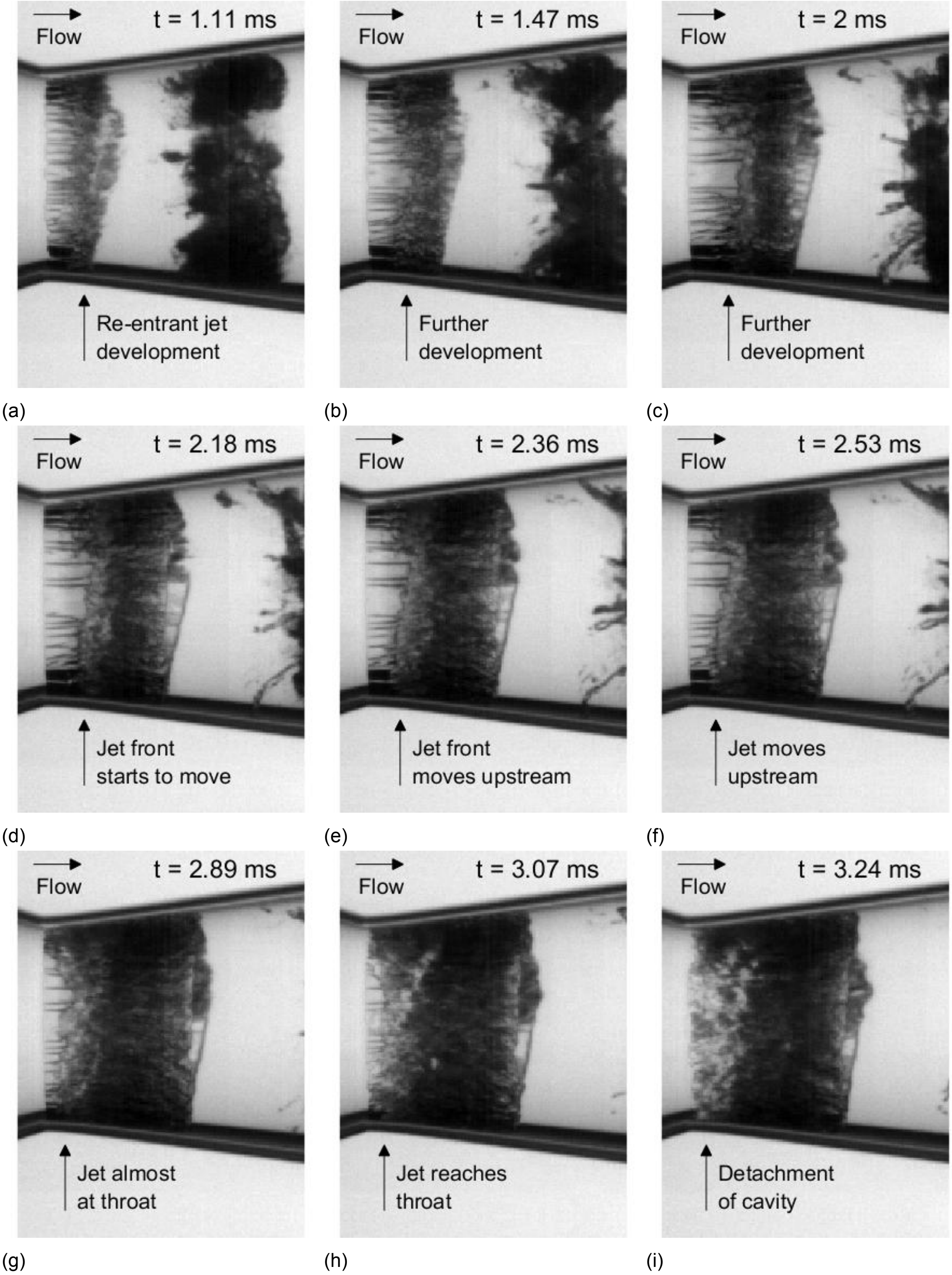

Figure 6.11: Video frames of re-entrant jet development. In figures 6.11a - 6.11c, re-entrant jet development can be observed. In figure 6.11d the jet front can be recognized by the chaotic interface, which can be seen above the arrow. The propagation of the jet front towards the venturi throat can be seen in figures 6.11d - 6.11h. In the end, cavity detachment is caused by the re-entrant jet as can be observed in figure 6.11i. In this situation the cavitation number is σ = 1.00.

In this figure the characteristic stick-slip shape, that was found in the region σ > 0.95, can be observed again. The corresponding videoframes are presented in figure 6.11. The first figure (6.11a) starts at t = 1.11 ms, where it can be seen that the re-entrant jet starts to develop. This development proceeds to t = 2.0 ms (figures 6.11b and 6.11c), after which the jet front starts to propagate in the venturi throat direction (6.11d). The re-entrant jet front can be recognized by the chaotic interface, which can be seen above the arrow. The propagation of the jet can be seen in figures 6.11e - 6.11g. The time at which the re-entrant jet reaches the throat, is shown in figure 6.11h. This causes a detachment of the cavity around t = 3.24 ms, as shown in figure 6.11i. From the x-t diagram in figure 6.10 follows that this detachment takes place at t $\approx$ 3.5 ms, which is in agreement with each other. This analysis points out that the typical stick-slip shape in the x-t diagram, found in the region σ > 0.95, is connected to re-entrant jet governed shedding.

From the highspeed images, the mechanism, which causes cavity detachment becomes also clear. Due to the shape of the venturi, flow separation is forced. In combination with an adverse pressure gradient (the pressure downstream is relative high and the pressure in the cavity is approximated by the vapor pressure), a re-entrant jet starts to develop. This re-entrant jet disconnects the cavity from the venturi throat, whereafter the cavity is advected with the flow and a new cavity starts to grow.

A number of re-entrant jet front tracking analysis is performed in order to estimate the re-entrant jet velocity. Global velocities of 1.1 - 3.4 m/s are found for mean flow velocities of 14.4 - 14.8 m/s at the venturi throat. The results are added in appendix A.

6.6. Bubbly shock dynamics

In this section a more detailed analysis of the bubbly shock dynamics is given. In figure 6.8, already a part of the bubbly shock dynamics is presented in the form of an x-t diagram. The corresponding video frames are shown in figure 6.12. Figures 6.12a and 6.12b are just before the time of complete cavity collapse. This complete collapse can be seen in figures 6.12c and 6.12d. This collapse causes a pressure wave, which is emitted in both directions (characteristic solution is given by u ±c). In figures 6.12e - 6.12m, the position of this (left running) pressure wave is indicated with an arrow. After passage of the pressure wave front, a new equilibrium state between the vapor and liquid phase must be formed. Due to the pressure rise after the pressure wave front, the void fraction in the (growing) cavity decreases by partial condensation. This was also observed in figure 6.8, where a difference in grayscale over the pressure wave was mentioned. When the pressure wave reaches the venturi throat, the cavity is detached, as follows from figure 6.12n.

The velocity of the pressure wave can be calculated from the inverse of the slope in the x-t diagram. First the pressure wave velocity in the growing cavitation cloud is determined, because this gives important insights on the physics of cavity detachment. The pressure wave path is well described with a second-order polynomial, as can be seen in figure 6.13a. The velocity of the pressure wave is given by the inverse of the derivative of this path. The pressure wave velocity in laboratory frame of reference is given by the black, continuous line in figure 6.13b. Adding the free stream velocity at the venturi throat, u_0, gives the upper bound for the absolute velocity of the pressure wave (blue line). However, if mass conservation is applied, the free stream velocity decreases as function of venturi position due to the divergent shape of the venturi. See for the velocity profile as function of venturi position, calculated with mass conservation, appendix A. Adding this velocity profile to the relative pressure wave velocity, gives the lower bound for the absolute velocity of the pressure wave (red line). The real, absolute velocity of the pressure wave is found between both extreme cases. Because the pressure wave travels through the cavity, the absolute velocity of the pressure wave can be best represented by adding the cavity growth rate to the relative pressure wave velocity. This velocity profile is given by the black, dashed line in figure 6.13b. It should be remarked that after pressure wave impact, this cavity growth rate changes, as can be seen from the change in slope, in figure 6.13a. This change in cavity growth velocity is probably caused by a higher downstream pressure, resulting in a decreasing growth velocity with a factor 1.19 with respect to the growth velocity before impact. This factor, which gives the change in velocity, is determined in appendix A. From the velocity profiles, the void fraction as function of position can be determined. To this end, the void fraction as function of speed of sound is presented in figure 6.14a. Two different void fraction profiles are presented, where the k-value is varied. In case of isothermal bubble behavior, k = 1.0 and in case of adiabatic bubble behavior, k = 1.3. If k = 1, both phases are in thermal equilibrium with each other. For instantaneous heat transfer, an infinitely homogenized mixture of vapor and liquid is required, with an extremely large heat transfer area between

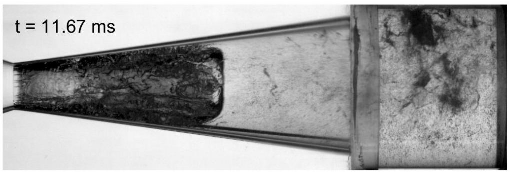

(a)

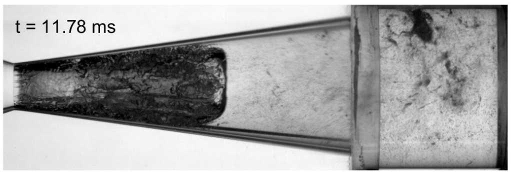

(b)

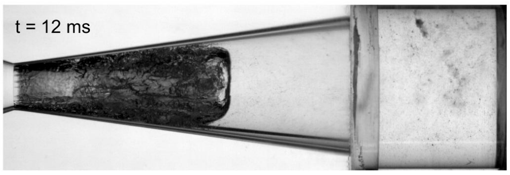

(c)

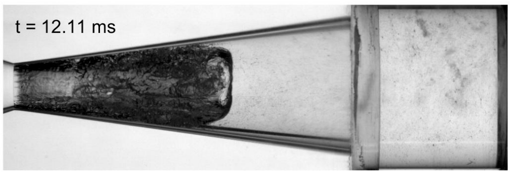

(d)

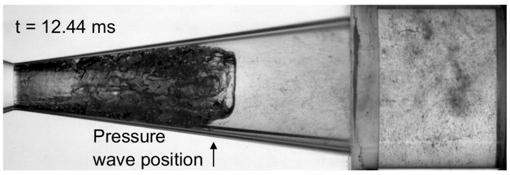

(e)

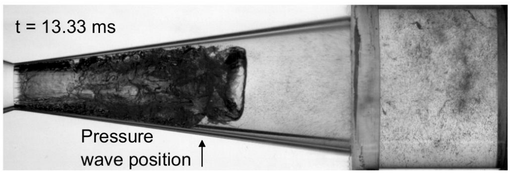

(f)

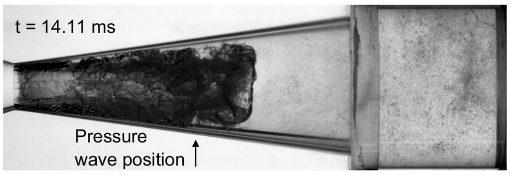

(g)

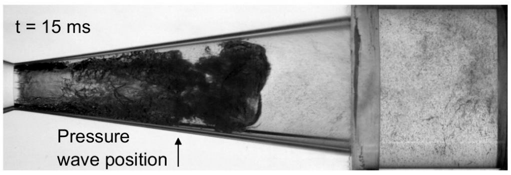

(h)

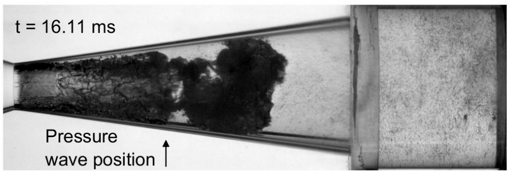

(i)

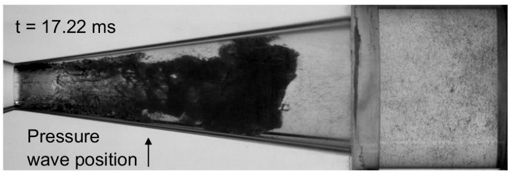

(j)

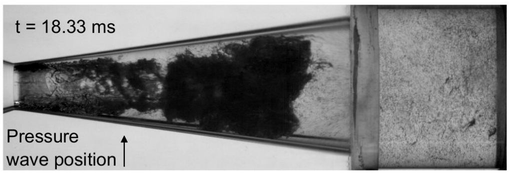

(k)

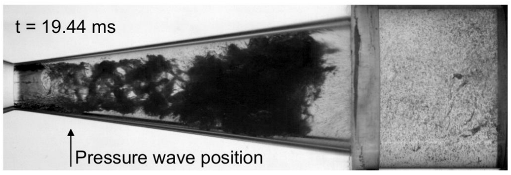

(l)

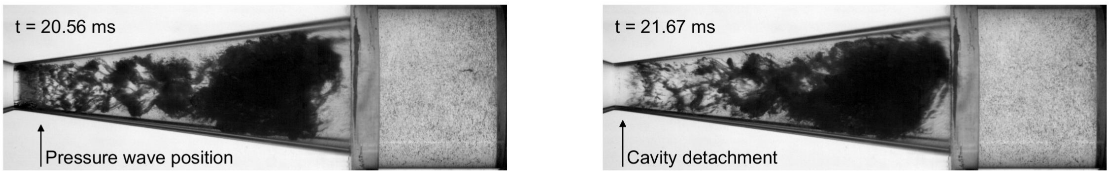

(m) (n)

Figure 6.12: Video frames of bubbly shock development. In figures 6.12a and 6.12b a collapsing cavity can be seen (right part of figure). In the subsequent figures (6.12c and 6.12d) the cavity is collapsed completely and a pressure wave is emitted. The position of this pressure wave is tracked and indicated in figures 6.12e - 6.12m. Condensation of the cavity beyond the pressure wave can be seen due to the higher pressure there. Cavity detachment can be observed when the pressure wave reaches the throat. The cavitation number is σ = 0.40 (u_0 = 13.7 m/s and p = 40 kPa) and Fs = 9kHz.

both phases. On the other hand, if k = 1.3, no heat transfer between both phases is assumed. In practice, the actual k-value lies in between both cases, depending on the mixture homogeneity and the heat transfer area between both phases. An enlargement of the profiles, in the region of interest, is shown in figure 6.14b. The void fraction profiles are determined with equation 2.9, according to the model given by Minnaert [25].

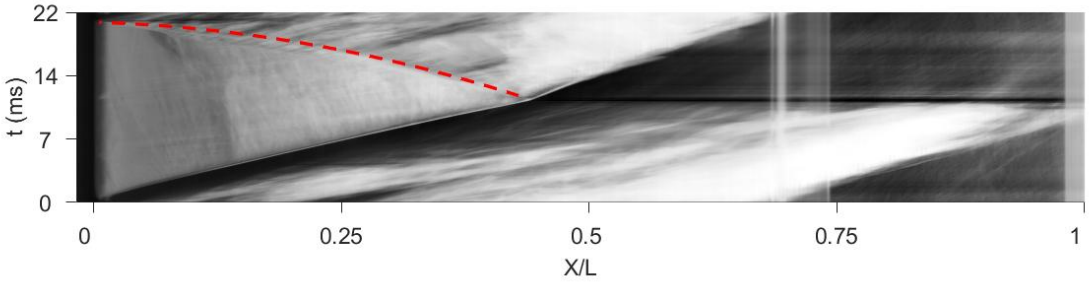

(a) X-t diagram of the shedding cycle from figure 6.12. A second order polynomial is fitted (red dotted line) to the pressure wave path.

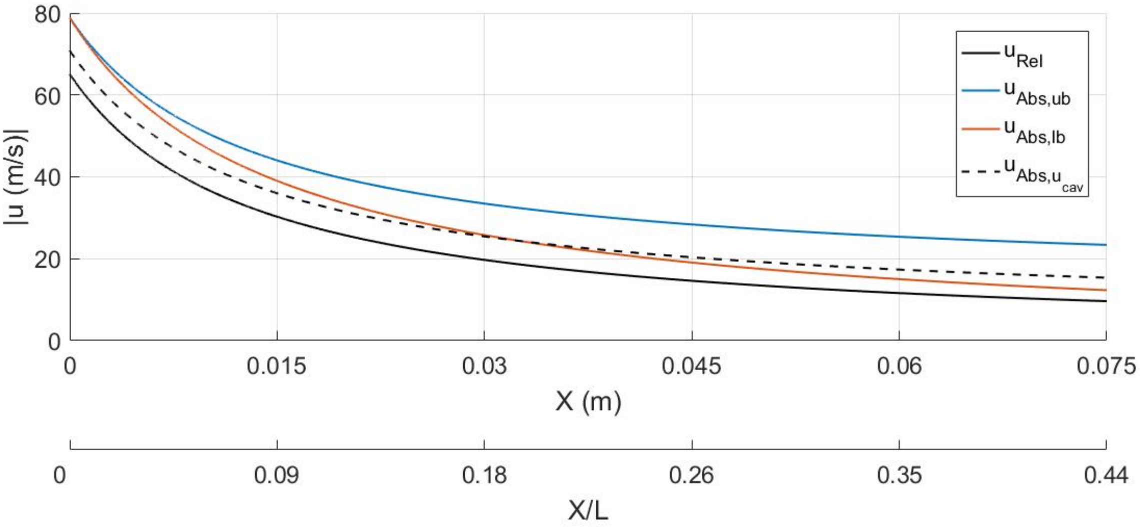

(b) Velocity profiles of the pressure wave as function of position. The black line is the velocity in the laboratory frame of reference. The blue line is the absolute velocity, where u_0 is added to the relative velocity. This gives the upper bound. If mass conservation to account for geometry change is applied, the velocity profile is given by the red line, which gives the lower bound. The black dashed line gives the absolute velocity based on the cavity growth rate.

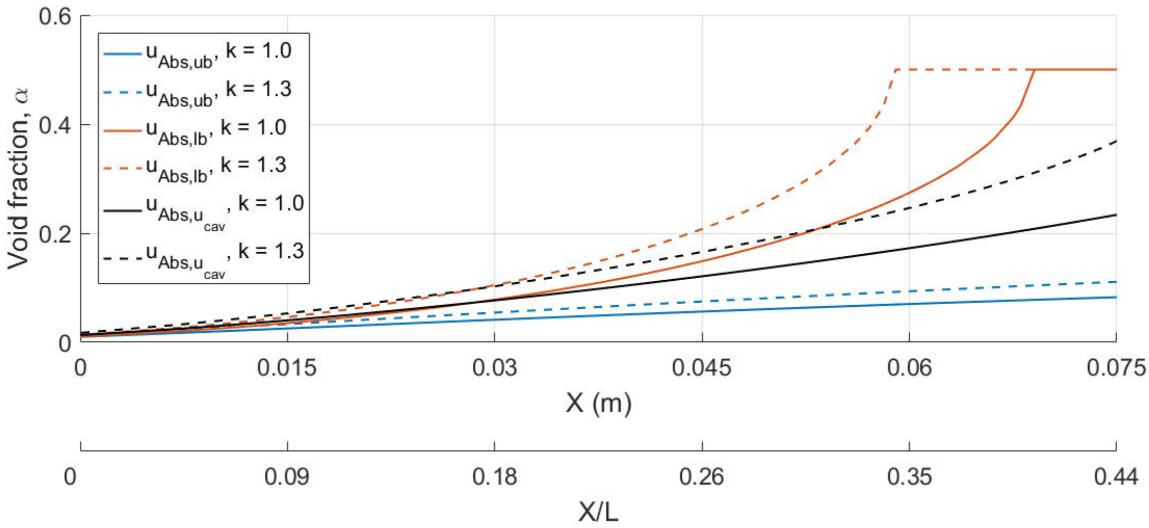

(c) Void fraction profiles as function of position corresponding to the absolute velocity profiles. The void fraction of the cavity is best approximated by the black curves, which lies in between both extreme curves. Although the different curves are deviatiating for X/L = 0.44, all profiles are converging to 1.1 % at the throat position. No solution is found for the part of the red curves where α = 0.5.

Figure 6.13: Pressure wave path with corresponding velocity and void fraction profiles.

The void fraction profiles for the three absolute velocity profiles and both k-values are presented in figure 6.13c. It should be noted that for both profiles of $u_{Abs,lb}$ no solution is found for α = 0.5. This implies that the velocity profile $u_{Abs,lb}$ is non-physical and the real free stream velocity is higher than this extreme case. Despite the spreading for X/L = 0.44, it can be seen that for X/L < 0.19 or X < 0.03 m the void fraction profiles are in the same order of magnitude, and are further converging to the same value at the throat position. The void fraction at the throat is found to be 1.1 % in all cases. From this observation, the cavity detachment mechanism in shockwave induced shedding can be derived.

It is already shown that the pressure wave causes partial condensation of the growing cavity. By this condensation, the void fraction of the complete cavity is decreased, also the part of the cavity where the lowest void fraction is found. By complete condensation of this connecting cavity part, the link between the cavity and the venturi throat is broken. The condensation of this connecting cavity part and the detachment of the cavity can be seen in figure 6.12n. From this can be derived that the mechanism of cavity shedding is basically a disconnection from the growing cavity and the throat, caused by condensation. This condensation is induced by a pressure wave, which is caused by the previously detached and collapsed cavity.

It can be proposed that for cavity detachment a pressure wave with a certain critical magnitude is required, in order to fully condensate the connecting cavity part. This implies that pressure waves with smaller amplitudes than this critical magnitude are not capable to cause cavity detachment. In figure 6.8 a pressure wave, caused by partial cloud collapse, can be observed at t ≈ 26 ms and X/L ≈ 0.4. The corresponding pressure wave path can be seen in the growing cavity, reaching the venturi throat at t ≈ 34 ms. However, no cavity detachment follows, but the cavity is still growing further, until the pressure wave at t ≈ 34 ms detaches this cavity at t ≈ 45 ms. Apparently, the pressure wave emitted from partial cloud collapse was not strong enough for condensation of the connecting cavity part and causing cavity detachment.

It is also interesting to note that the left running pressure wave, when it reaches the throat, is reflected. This reflected pressure wave can be observed in figure 6.8 at t ≈ 21 ms, starting from the venturi throat and propagating to the right. This reflection is possibly caused by the transition from a vapor phase to a liquid phase. This transition is accompanied with a steep velocity gradient of the pressure wave, as

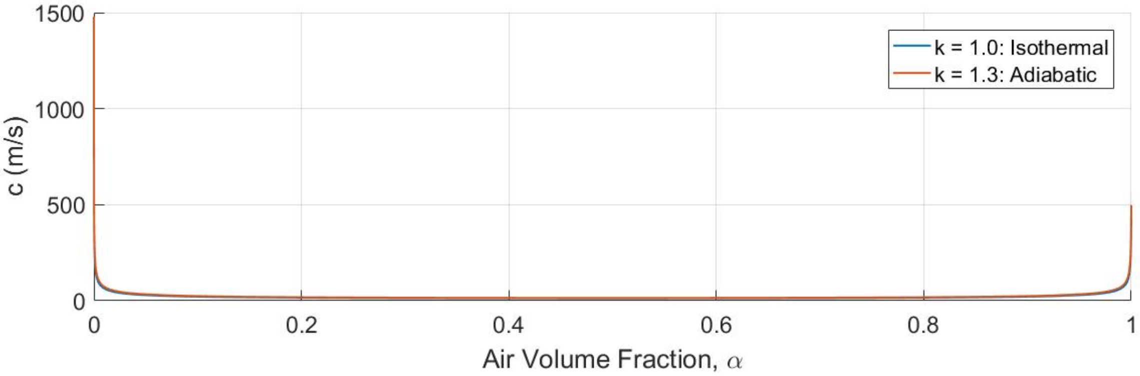

(a) Void fraction profiles as function of speed of sound. The selected parameters are ρ_l = 1000 kg/ m3, ρ_v = 0.21 kg/m3, c_l = 1480 m/s and p = 40 kPa. Two profiles are presented for different k values, where k = 1.0 corresponds to the case where no heat is exchanged and k = 1.3 corresponds to the adiabatic case.

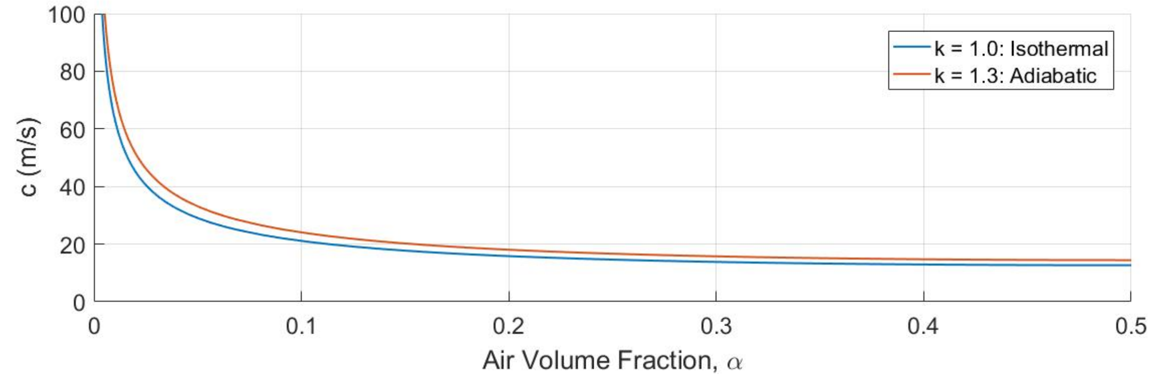

(b) Enlarged section of figure 6.14a in the region of interest. The difference in speed of sound between both cases can be seen more clearly.

Figure 6.14: Void fraction profiles as function of speed of sound.

follows from figure 6.14a. However, the black line (i.e. pressure wave) vanishes at X/L ≈ 0.2, because of decreasing amplitude of the pressure wave. It is important to note that the amplitude of every pressure wave is decreasing as function of position, because the pressure is distributed over a larger volume. Thus far, the velocity of the pressure wave in the growing cavity is presented, from which the physics of the periodic cavity shedding are derived. The velocity determination of the pressure wave in the liquid region is much more difficult. Due to the high velocity of the pressure wave in liquid, the slope of the black line is almost zero. To this end a video with a sample frequency of Fs = 125 kHz is recorded. The corresponding x-t diagram is shown in 6.15. The yellow section in the big x-t diagram is enlarged, and shown in the figure below that box. The expected source of the pressure wave is denoted with a yellow cross and the corresponding theoretical pressure wave path is indicated with a continuous yellow line. This line corresponds to the propagation velocity of a sound wave in pure liquid (c = 1480 m/s). The actual pressure wave velocity is slightly lower, and is best approximated with the dashed yellow line, with a velocity of 900 m/s. It is interesting to see that there is more than one pressure wave emitted from the cloud collapse, as can be seen by the different black lines in figure 6.15.

The pressure wave path is tracked through the cavity, but there is still a core that consists of liquid. The speed of sound in this liquid core is the same order of magnitude as found in the above conducted analysis. If the black shockwave path in figure 6.13a is extrapolated through the cavity, a white kind of plume can be observed at the cavity part at the throat (t ≈ 11 ms). This plume is possibly caused by the pressure wave, which traveled through the liquid core region instead of traveling through the cavity.

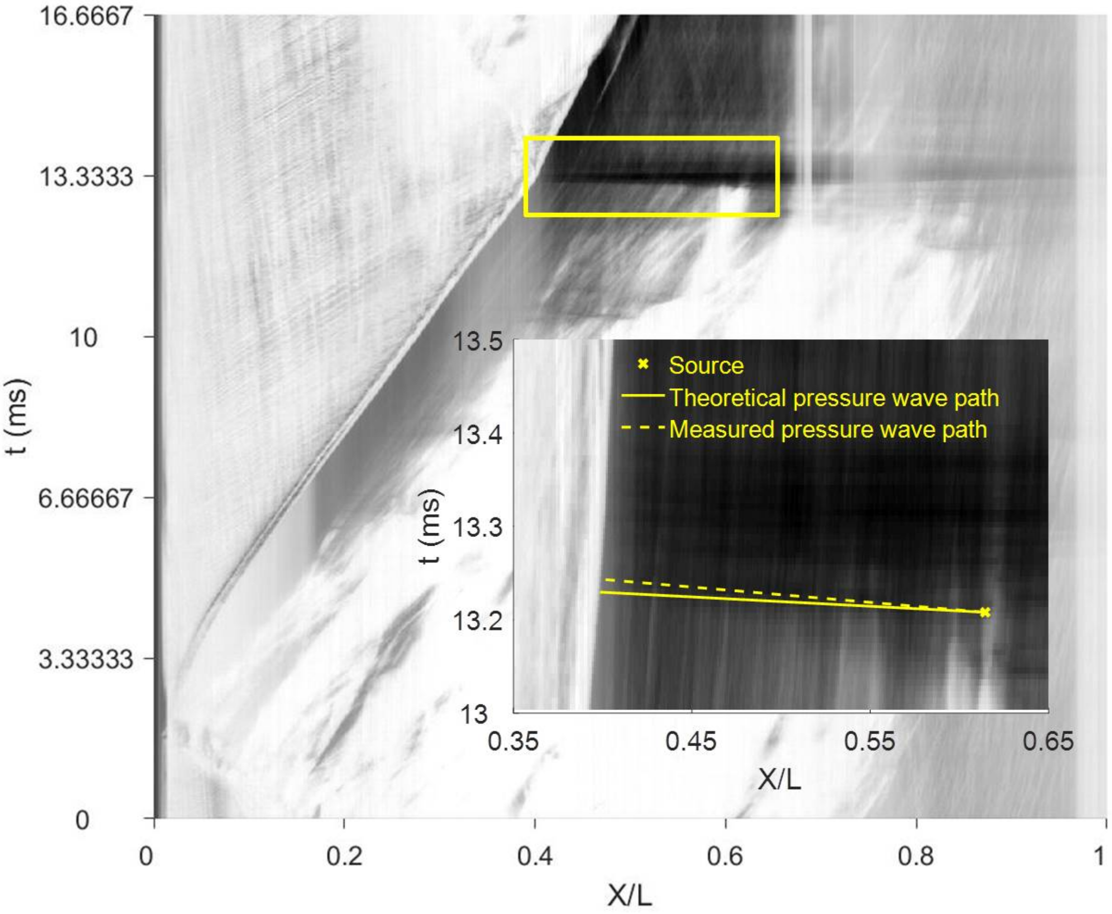

Figure 6.15: X-t diagram with an enlarged pressure wave path. The expected source of the pressure wave is indicated with a yellow cross (t ≈ 13.2 ms and X/L ≈ 0.62). The theoretical pressure wave path is indicated with the yellow line, where the speed of sound in pure liquid is used (c = 1480 m/s). The dashed yellow line gives the best approximation of the pressure wave path, corresponding to a velocity of 900 m/s. The sample frequency used is Fs = 125 kHz and the cavitation number is σ = 0.41 (u_0 = 13.5 m/s and p = 40 kPa).

6.7. Shear cavitation

The focus of this research is especially on cloud cavitation shedding and the corresponding physics and mechanisms. However, an introduction towards shear cavitation or jet cavitation can be given, based on the previous presented results. At a certain point, periodic cloud cavitation shedding stops, and a continuous jet is formed. In the experimental setup, this jet is indeed observed for low cavitation numbers ($\sigma \approx$ 0.1). Linear extrapolation of figure 6.5 for σ < 0.85 gives indeed an infinite shedding timescale for $\sigma \approx$ 0.14. A picture of the observed jet can be seen in figure 6.16. In this figure the flow direction is from left to right. The black lines along the venturi boundary are due to the difference in refractive index between water and perspex (the venturi material). It can also be observed that the jet diameter decreases as a function of X position. This can be due to the vena contracta effect, but also due to evaporation of the jet. According to Franc and Michel [11], these jets are rather complicated, since different kinds of vortices are formed such as toroidal, linear streamwise and helical vortices. Based on the observation, the next question can be formulated: What kind of mechanism stops the periodic cloud cavitation shedding? The answer of this question is most probably found in the length and velocity scales, just before formation of this jet. However, due to leakages in the system for p < 40 kPa, the final available measurement serie is for p = 30 kPa. In addition, due to the geometrical properties of the system, cavity lenghts l_0 > 0.17 m cannot be observed completely. Therefore the measurement serie for p = 30 kPa is used for further insights. In figure 6.13 the velocity profile of the pressure wave in the cavity is determined. It follows that this velocity profile is a function of void fraction or vice versa. The highest void fraction or lowest pressure wave velocity is found at the tip of the cavity

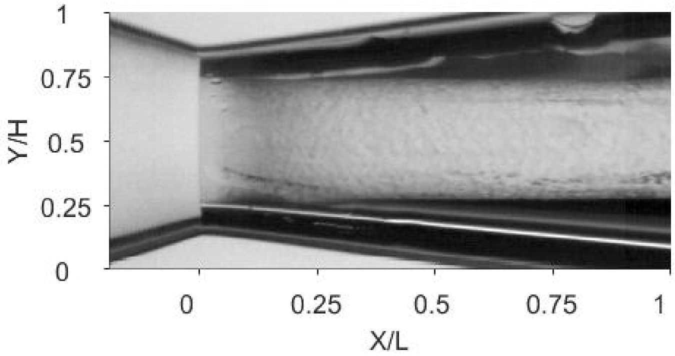

Figure 6.16: Image of continuous jet. The flow direction is from left to right. The black lines along the venturi boundary are coming from the difference in refractive index between water and perspex (venturi).

cloud. The Mach number, in laboratory frame of reference, of this pressure wave at this point can be calculated with equation 2.8. For u the cavity growth rate after pressure wave impact is selected, because after this impact the growth rate is decreased with a factor of 0.84. This factor is derived in appendix A. For c, the pressure wave velocity at the cavity tip is chosen where the void fraction is highest. The Mach number as function of cavitation number is shown in figure 6.17. A decreasing linear relation can be observed for the Mach number as function of cavitation number. The fit gives the expected behavior as function of cavitation number. The condition Ma = 1 is expected for σ = 0.11. For this critical condition, the pressure wave is not able to propagate upstream, through the cavity, and cause cavity detachment at the throat. The periodic cavity shedding regime ends for Ma = 1 and shear or jet cavitation starts. Based on this, three different situations can be distinguished:

$Ma < 1$: Fully developed / pressure wave driven cavitation
$Ma = 1$: Critical case, shear cavitation initiated
$Ma > 1$: Shear cavitation

In order to verify these expectations, it is recommended to perform more velocity measurements for cavitation number 0.05 < σ < 0.3. To this end, a leak-proof set-up with a longer test-section is necessary. Another way of looking to the physical background of the jet is from energy point of view. The upstream energy is given by the potential energy, present in the flow, and the downstream energy is given by the acoustic energy. For a certain critical combination of both, shear cavitation is initiated.

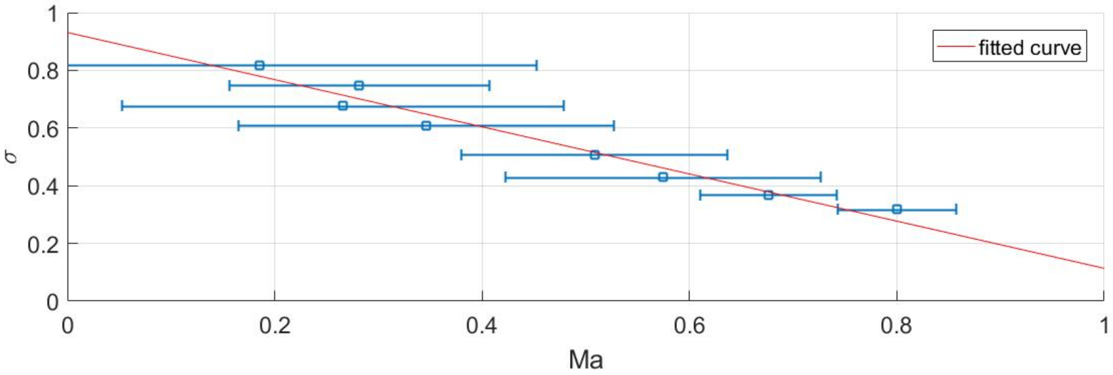

Figure 6.17: Mach number at the cavity tip as function of cavitation number. The Mach number is based on the cavity growth velocity after pressure wave impact. The uncertainty is based on $\frac{std}{\sqrt{n}}$. The linear fit gives the expected behavior as function of cavitation number. The critical case: Ma = 1 is reached for σ = 0.11.

7

Conclusion and recommendations

7.1. Conclusion

The purpose of the current study was to investigate the different cavitation regimes in a CD axisymmetric nozzle, in order to validate and further develop numerical two-phase flow models with the obtained data. The different cavitation regimes are generated by systematically changing the global static pressure and flow velocity. From this study, the following conclusions are formulated.

For a cavitation number based on global static pressure, the pressure loss coefficient is found to be a linear function of cavitation number only. Flow blockage is increasing for decreasing cavitation number. For the same definition of the cavitation number, cavity lenght and time scales are also a function of cavitation number only. In case of cavity length and time scales, a non-linear behavior is found. Both scales are combined in the Strouhal number, based on the cavity lengths at time instant of detachment. This Strouhal number is the dimensionless form of the integral cavity growth velocity. It follows that for this Strouhal number, as function of cavitation number, a global minimum is found for a cavitation number $\sigma = 0.88$.

Based on this result, and the cavitation dynamics in the x-t diagrams, three different cloud cavitation shedding regimes can be identified. It is found that for $\sigma > 0.95$, the periodic cavity shedding is caused by the re-entrant jet mechanism. Re-entrant jet governed cloud cavitation shedding is characterized by stick-slip behavior in the x-t diagram. For $\sigma < 0.8$, the prevalent mechanism for periodic cavity shedding is found to be the bubbly shock mechanism. Both mechanisms are encountered in the intermediate region, $0.8 < \sigma < 0.95$. From a physical point of view, both mechanisms are very different. The re-entrant jet motion is caused by flow separation and an adverse pressure gradient, which makes the re-entrant jet a pressure driven phenomenon. The bubbly shock in the growing cavity is caused by a pressure wave, which is emitted from the previously detached, advected and collapsing cavity. This makes this mechanism a shock-wave driven phenomenon.

The pressure wave velocity, as function of position, is determined from the pressure wave path in the x-t diagram. By means of the correlation between speed of sound and void fraction, the void fraction in the growing cavity is determined. The highest void fraction is found in the cavity front, and this void fraction is decreasing in the direction of the venturi throat. At the throat the lowest void fraction is found, which is 1.1 % in case of a cavitation number of $\sigma = 0.4$. From this void fraction profile the mechanism of cavity detachment in pressure wave driven cavitation is derived. The pressure wave partially condensates the growing cavity. The link between the cavity and the venturi throat is broken by full condensation of the connecting cavity part, where the void fraction is lowest. A pressure wave with a certain minimum amplitude is required for detachment of cavities, in order to fully condensate the connecting cavity part.

An introduction towards shear or jet cavitation is given, based on the found results. To this end, the Mach number is introduced in order to compare the pressure wave velocity with the cavity growth velocity. For the critical Mach number, Ma = 1, shear cavitation is initiated, because the pressure wave can not travel upstream and detach the growing cavity by means of condensation. Based on linear extrapolation of the obtained results, a critical cavitation number of $\sigma = 0.11$ is found. Shear cavitation is indeed observed, in the experimental setup, for $\sigma \approx 0.1$.

7.2. Recommendations for further research

In total, six recommendations are given for further research. In the first place Particle Image Velocimetry (PIV) is advised for accurate determination of the re-entrant jet velocity. An order of magnitude analysis is performed, however a large spreading is found in the obtained results. This has to do with an uncertainty in the depth of the measurement plane with respect to the venturi wall. By application of a laser sheet, particles can be tracked at the same distance with respect to the venturi wall and a quantitative analysis can be performed in this way. Secondly, a more quantitative analysis in the intermediate cavitation region $0.8 < \sigma < 0.95$, where both mechanisms are causing cavity shedding, is advised. This analysis gives a better insight on the time and length scales of both detachment mechanisms. Thirdly, very highspeed imaging (> 125 kHz) is advised for a better understanding of the pressure wave source, as well as a better estimation of the pressure wave propagation velocity. During these experiments a homogeneous light source is advised in order to reduce the noise in the x-t diagram. In the fourth place, an analysis of the effective throat diameter, which is changing as function of cavitation number, is recommended. If the highspeed camera is placed under a certain angle with respect to the venturi, this effective throat diameter can be determined. This analysis gives better insight in the link between pressure loss coefficient and throat diameter as function of cavitation number. The fifth recommendation is the verification of the current estimation of the void fraction profiles, as function of position. This verification can be done with X-ray measurements. From these measurements the effective throat diameter as function of position can also be obtained. With this, yet unknown, variable, the complete cavitation dynamics can be determined as function of time. The final recommendation has to do with shear or jet cavitation. In order to verify the presented expectations it is recommended to perform more velocity measurements (i.e. pressure wave and cavity growth) for cavitation number $0.05 < \sigma < 0.3$. To this end, a leak-proof set-up with a longer test-section is necessary.

Bibliography

[1] François Avellan, Philippe Dupont, and Mohamed Farhat. Cavitation erosion power 91 symposium, 1st asme-jsme fluid engineering conference, portland (oregon), usa, 23-27 june. *Proceedings of the Cavitation*, 116(LMH-CONF-1991-006):135–140, 1991.

[2] Gary J Balas, József Bokor, Bálint Vanek, and Roger EA Arndt. Control of high-speed underwater vehicles. In *Control of Uncertain Systems: Modelling, Approximation, and Design*, pages 25–44. Springer, 2006.

[3] Christopher E Brennen. *Cavitation and bubble dynamics*. Cambridge University Press, 2013.

[4] S Brinkhorst, E von Lavante, D Güler, and G Wendt. Experimental investigation of cavitating herschel venturi-tube configuration. FLOMEKO, 2016.

[5] Mathieu Callenaere, Jean-Pierre Franc, Jean-Marie Michel, and Michel Riondet. The cavitation instability induced by the development of a re-entrant jet. *Journal of Fluid Mechanics*, 444:223–256, 2001.

[6] Amélie Danlos, Florent Ravelet, Olivier Coutier-Delgosha, and Farid Bakir. Cavitation regime detection through proper orthogonal decomposition: Dynamics analysis of the sheet cavity on a grooved convergent–divergent nozzle. *International Journal of Heat and Fluid Flow*, 47:9–20, 2014.

[7] DF De Lange and GJ De Bruin. Sheet cavitation and cloud cavitation, re-entrant jet and three-dimensionality. In *In Fascination of Fluid Dynamics*, pages 91–114. Springer, 1998.

[8] Matevz Dular, I Khlifa, Sylvie Fuzier, M Adama Maiga, and Olivier Coutier-Delgosha. Scale effect on unsteady cloud cavitation. *Experiments in fluids*, 53(5):1233–1250, 2012.

[9] Validyne Engineering. Pressure transducers, transmitters & sensors | data acquisition & signal conditioning systems | validyne engineering, 2016. URL `http://validyne.com/`.

[10] Evert-Jan Foeth, Tom van Terwisga, and Cas van Doorne. On the collapse structure of an attached cavity on a three-dimensional hydrofoil. *Journal of Fluids Engineering*, 130(7):071303, 2008.

[11] Jean-Pierre Franc and Jean-Marie Michel. *Fundamentals of cavitation*, volume 76. Springer Science & Business Media, 2006.

[12] Harish Ganesh. *Bubbly shock propagation as a cause of sheet to cloud transition of partial cavitation and stationary cavitation bubbles forming on a delta wing vortex*. PhD thesis, The University of Michigan, 2015.

[13] Harish Ganesh, Simo A Mäkiharju, and Steven L Ceccio. Bubbly shock propagation as a mechanism for sheet-to-cloud transition of partial cavities. *Journal of Fluid Mechanics*, 802:37–78, 2016.

[14] Kelly Hudson and Bijan Kazem. Highly efficient method of mixing dissimilar fluids using mechanically induced cavitation, September 30 2003. US Patent 6,627,784.

[15] Isaak E Idelchik and Erwin Fried. Handbook of hydraulic resistance. 1986.

[16] Jablonská Jana, Kozubková Milada, Himr Daniel, and Weisz Michal. Methods of experimental investigation of cavitation in a convergent-divergent nozzle of rectangular cross section. *Measurement Science Review*, 16(4):197–204, 2016.

[17] Bin Ji, Xianwu Luo, Yulin Wu, Xiaoxing Peng, and Yunling Duan. Numerical analysis of unsteady cavitating turbulent flow and shedding horse-shoe vortex structure around a twisted hydrofoil. *International Journal of Multiphase Flow*, 51:33–43, 2013.

[18] F Joussellin, Y Delannoy, E Sauvage-Boutar, and B Goirand. Experimental investigations on unsteady attached cavities. *Cavitation'91*, pages 61–66, 1991.

[19] Y Kawanami, H Kato, H Yamaguchi, M Tanimura, and Y Tagaya. Mechanism and control of cloud cavitation. *Journal of Fluids Engineering*, 119(4):788–794, 1997.

[20] Robert T Knapp. Recent investigations of the mechanics of cavitation and cavitation damage. *Transactions of the ASME*, 77:1045–1054, 1955.

[21] A Kubota, H Kato, H Yamaguchi, and M Maeda. Unsteady structure measurement of cloud cavitation on a foil section using conditional sampling technique. *Journal of Fluids Engineering*, 111 (2):204–210, 1989.

[22] P.K. Kundu, I.M. Cohen, and D.R. Dowling. *Fluid Mechanics*. Elsevier Science, 2015.

[23] Q Le, Jean-Pierre Franc, and JM Michel. Partial cavities: global behavior and mean pressure distribution. *Journal of Fluids Engineering*, 115(2):243–248, 1993.

[24] Hans Lindgren and Carl Anders Johnsson. *Cavitation Inception on Head Forms ITTC Comparative Experiments*, volume 3. Akademiförlaget/Gumpert, 1966.

[25] Marcel Minnaert. Xvi. on musical air-bubbles and the sounds of running water. *The London, Edinburgh, and Dublin Philosophical Magazine and Journal of Science*, 16(104):235–248, 1933.

[26] J Nikuradse. Gesetzmäßigkeiten der turbulenten strömung in glatten rohren. 1932.

[27] TM Pham, F Larrarte, and DH Fruman. Investigation of unsteady sheet cavitation and cloud cavitation mechanisms. *Journal of fluids engineering*, 121(2):289–296, 1999.

[28] Lord Rayleigh. Viii. on the pressure developed in a liquid during the collapse of a spherical cavity. *The London, Edinburgh, and Dublin Philosophical Magazine and Journal of Science*, 34(200): 94–98, 1917.

[29] Osborne Reynolds. The causes of the racing of the engines of screw steamers investigated theoretically and by experiment. *Trans. Inst. Naval Arch*, 14:56–67, 1873.

[30] Pavel Rudolf, Martin Hudec, Milan Gríger, and David Štefan. Characterization of the cavitating flow in converging-diverging nozzle based on experimental investigations. In *EPJ Web of Conferences*, volume 67, page 02101. EDP Sciences, 2014.

[31] Motoyuki Sakoda, Ryo Yakushiji, Masatusgu Maeda, and Hajime Yamaguchi. Mechanism of cloud cavitation generation on a 2-d hydrofoil. *http://resolver. caltech. edu/cav2001: sessionA9. 004*, 2001.

[32] Keiichi Sato and Yasuhiro Saito. Unstable cavitation behavior in a circular-cylindrical orifice flow. *JSME International Journal Series B Fluids and Thermal Engineering*, 45(3):638–645, 2002.

[33] Hoseyn Sayyaadi. Instability of the cavitating flow in a venturi reactor. *Fluid Dynamics Research*, 42(5):055503, 2010.

[34] Vladimir Pavlovich Skripov. *Metastable liquids*. Wiley, 1974.

[35] S Som, Suresh K Aggarwal, EM El-Hannouny, and DE Longman. Investigation of nozzle flow and cavitation characteristics in a diesel injector. *Journal of Engineering for Gas Turbines and Power*, 132(4):042802, 2010.

[36] C Stanley, T Barber, and G Rosengarten. Re-entrant jet mechanism for periodic cavitation shedding in a cylindrical orifice. *International Journal of Heat and Fluid Flow*, 50:169–176, 2014.

[37] Daniel R Stull. Vapor pressure of pure substances. organic and inorganic compounds. *Industrial & Engineering Chemistry*, 39(4):517–540, 1947.

[38] B Stutz and JL Reboud. Experiments on unsteady cavitation. *Experiments in fluids*, 22(3):191–198, 1997.

[39] Petar Tomov, Kilian Croci, Sofiane Khelladi, Florent Ravelet, Amélie Danlos, Farid Bakir, and Christophe Sarraf. Experimental and numerical investigation of two physical mechanisms influencing the cloud cavitation shedding dynamics. 2016.

[40] EA Weitendorf. On the history of propeller cavitation and cavitation tunnels. In *Fourth International Symposium on Cavitation*, 2001.

[41] Frank M White. Fluid mechanics/frank m. white, 2003.

[42] Stewart Whitworth. Cavitation prediction of flow over the delft twist 11 foil. In *Second International Symposium on Marine Propulsors smp'11*, 2011.

[43] Songlin Zhu, Franklin H Cocks, Glenn M Preminger, and Pei Zhong. The role of stress waves and cavitation in stone comminution in shock wave lithotripsy. *Ultrasound in medicine & biology*, 28 (5):661–671, 2002.

A

Appendix

Pressure calibration curves

The differential pressure sensors in the system are calibrated before use. The found calibration curves are shown in figure A.1.

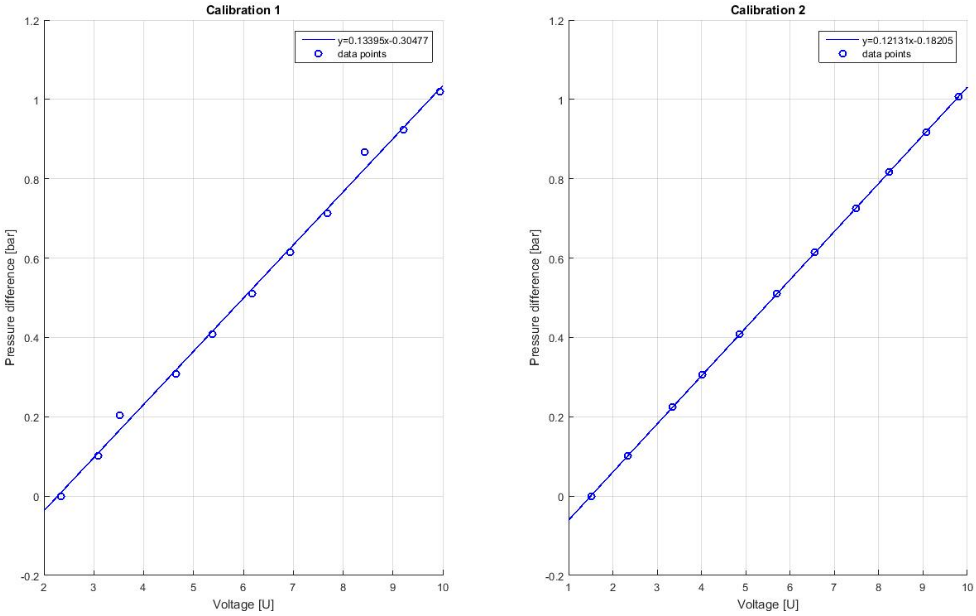

Figure A.1: Calibration curves of the differential pressure transducers

System frequency analysis

In order to ensure that only the shedding frequency is measured, first a system frequency analysis is performed. For this analysis the pressure sensors are used, because of the limited memory of the high speed camera. The system is operated for 300 seconds at a mean flow velocity of 1.02 m/s (cavitation was not present at the venturi). From the obtained pressure data a powerspectrum is determined, as can be seen in figure A.2. It can be concluded that there is not a frequency component captured in the frequency range which is in the region of interest.

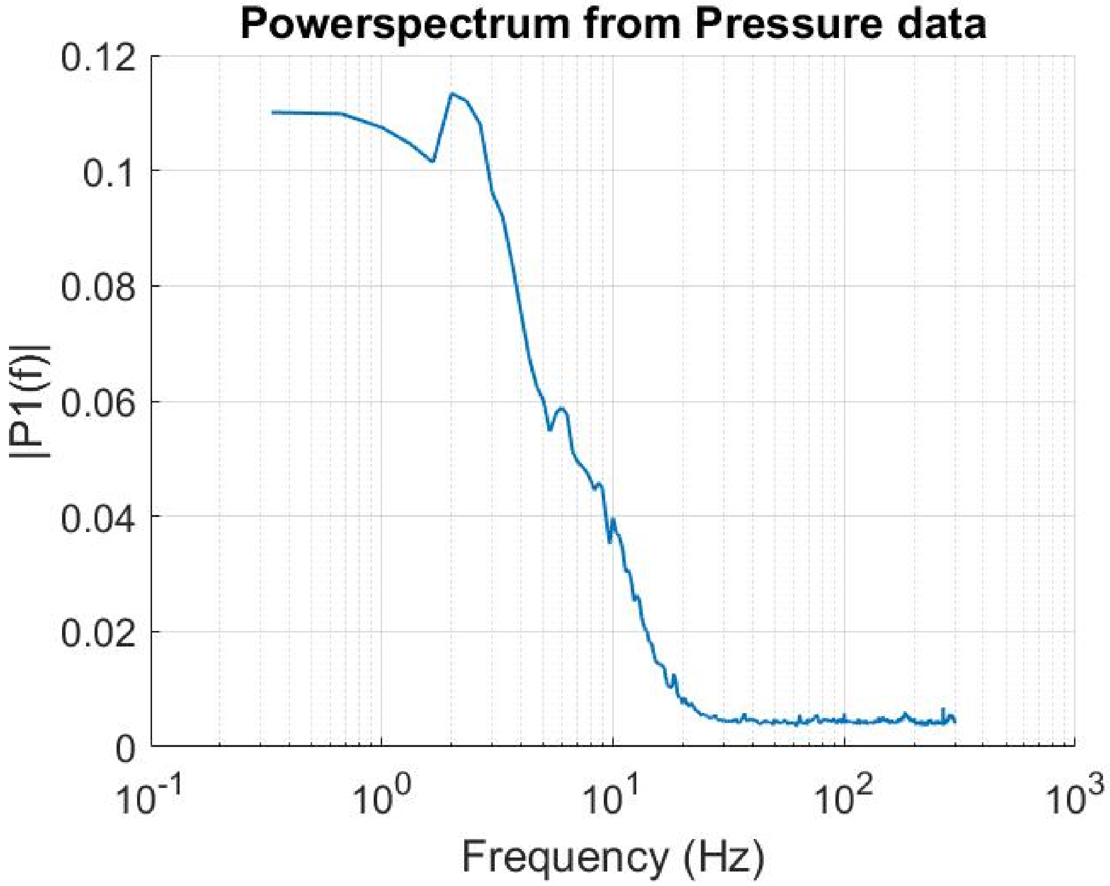

Figure A.2: Frequency analysis of the system from pressure data in the region of interest.

Velocity shift factor

When the emitted pressure wave by a cavity collapse hits the growing cavity, a change in slope can be observed. This change in slope is rather significant in the Mach number determination, because this changed (!) slope determines the cavity growth rate after pressure wave impact. Figure A.3 corresponds to the case of figure 6.13. In this figure the change in slope is determined from the three points and the corresponding lines. A ratio of 1 to 0.84 is found, indicating that the growth velocity decreases with a factor 0.84.

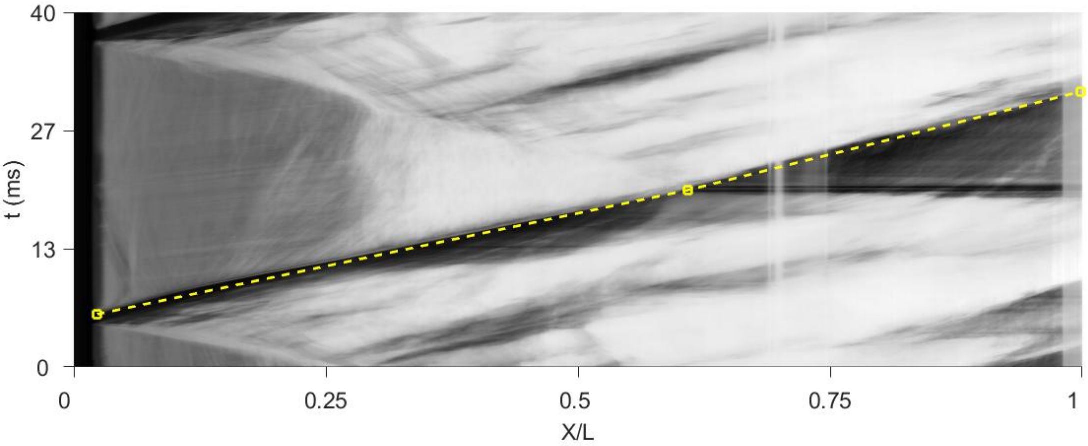

Figure A.3: Cavity growth velocity change analysis before and after impact of pressure wave.

Re-entrant jet velocity analysis

The re-entrant jet velocity is determined by means of re-entrant jet front tracking. Four different cases are analyzed. The position of the front as function of time is shown in figures A.4 - A.7. The fit through the datapoints gives the global path of the re-entrant jet. The derivative of this fit gives the integral velocity of the re-entrant jet. This velocity scale varies from 1.1 - 3.4 m/s, probably due to variation of the re-entrant jet position with respect to the venturi wall. In the near wall region the pressure and velocity gradient is steep, that can result in a variation of re-entrant jet velocity. In order to obtain more accurate results, PIV is recommended to ensure a constant position from the measurement plane with respect to the venturi wall.

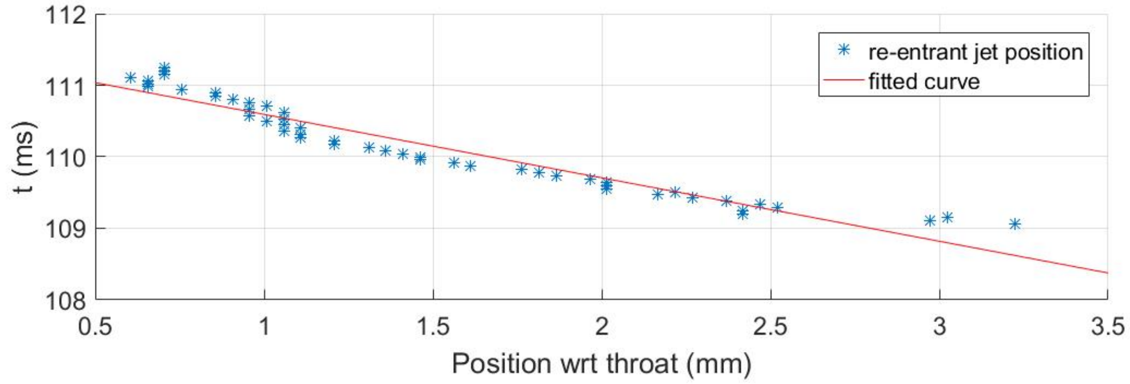

Figure A.4: Re-entrant jet position as function of time, u_0 = 14.4 m/s. The order of magnitude for the velocity is found to be -1.13 ± 0.10 m/s.

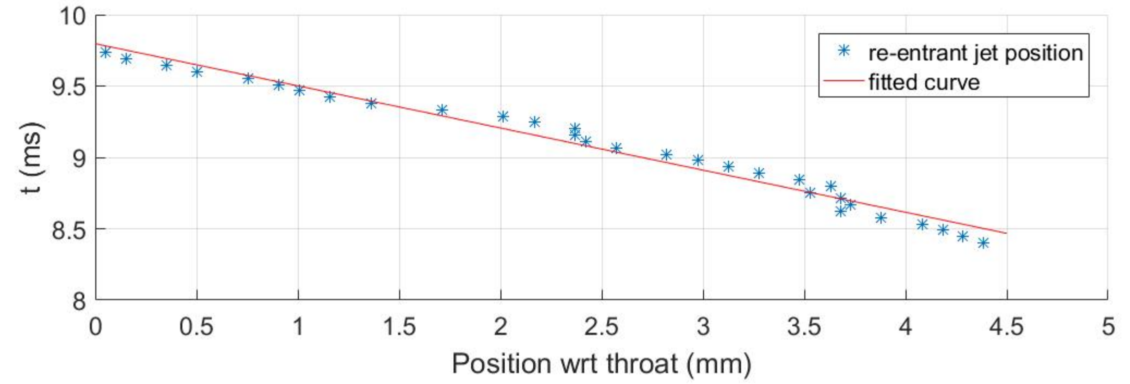

Figure A.5: Re-entrant jet position as function of time, u_0 = 14.4 m/s. The order of magnitude for the velocity is found to be -3.39 ± 0.21 m/s.

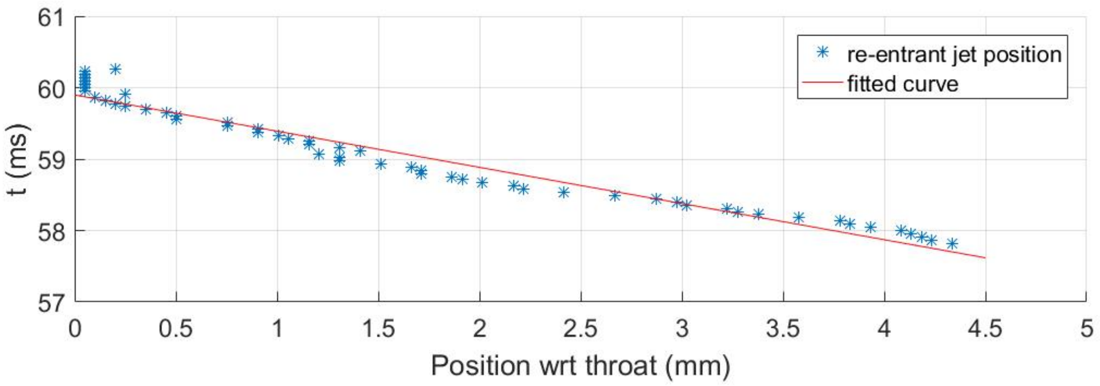

Figure A.6: Re-entrant jet position as function of time, u_0 = 14.7 m/s. The order of magnitude for the velocity is found to be -1.97 ± 0.13 m/s.

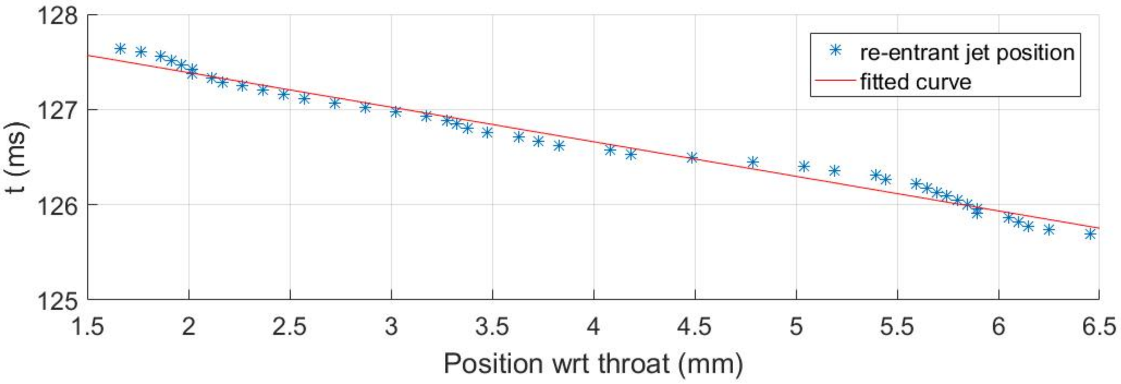

Figure A.7: Re-entrant jet position as function of time, u_0 = 14.8 m/s. The order of magnitude for the velocity is found to be -2.75 ± 0.13 m/s.

Velocity after venturi throat calculated bij mass conservation

In figure A.8, the normalized velocity profile as function of venturi position is presented. This profile is calculated by the mass conservation equation (A · u = constant).

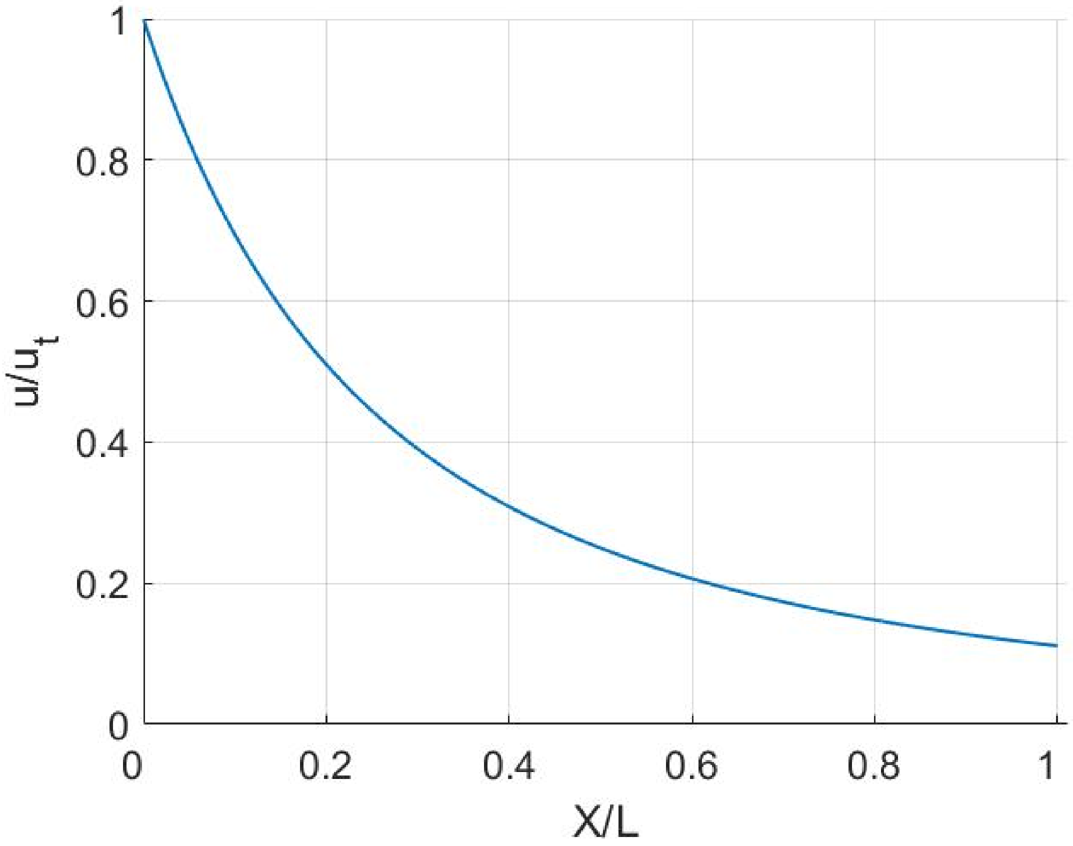

Figure A.8: Normalized stream-wise velocity as function of venturi position.

Oxygen content measurements

The oxygen content in the setup is measured for each dataserie. The results are tabulated in table A.1. The result for p = 109.5 is missing, because the sensor was not working properly that day. Some second measurements are not presented, because after some measurement series, it was decided to perform two oxygen content measurements. For the current measurement values, the uncertainty is ±0.1 mg/l.

Table A.1: Oxygen content for different global static pressures.

Pressure (kPa)	Measurement 1		Measurement 2	
	mg/l	% saturation	mg/l	% saturation
100	3.9	42		
90.0	3.6	38	3.1	34
80.0	3.1	35		
70.0	4.0	45	3.7	43
60.0	3.7	43		
50.0	3.6	41		
40.0	2.8	30	2.9	34
30.0	2.9	31	3.1	34

Systematic calibration error

A systematic error is introduced by not calibrating the venturi. This error can be determined from comparison of the calibrated and not calibrated calibration target in the venturi. The locations of two crosses in the corrected calibration target image are determined and depicted in the raw calibration target image. This can be seen in figure A.9, where both crosses are encircled. The difference between both yellow crosses is found to be 911 pixels, whereas the difference between the corresponding crosses in the raw image is found to be 914 pixels. This results in a systematic error of 3 pixels. Taking the change in field of view into account, factor 1.39, the systematic error reduces to 2.2 pixels.

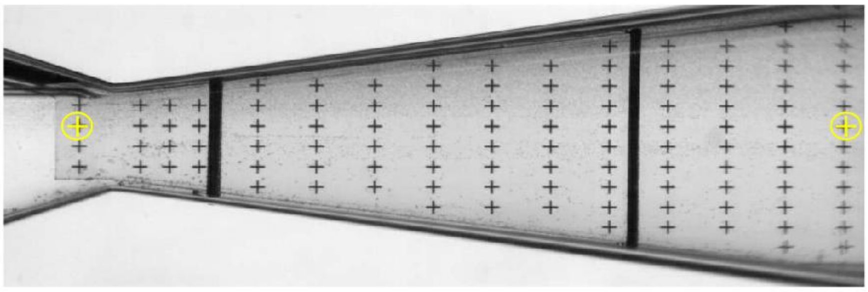

Figure A.9: Raw calibration target image with two, encircled crosses from the corrected calibration target image. It can be seen that the effect of the calibration is almost negligible.

Frequency analysis of illumination source

A frequency analysis of the illumination source (LED panel) is performed, in order to check whether the peak of 10 Hz is coming from the LED panel. To this end, a video of the illumination source at a frequency of 50 Hz (3000 frames) is recorded. From this movie, the frequency is determined, which is presented in figure A.10. It follows from this frequency response that the peak of 10 Hz is not caused by the light source.

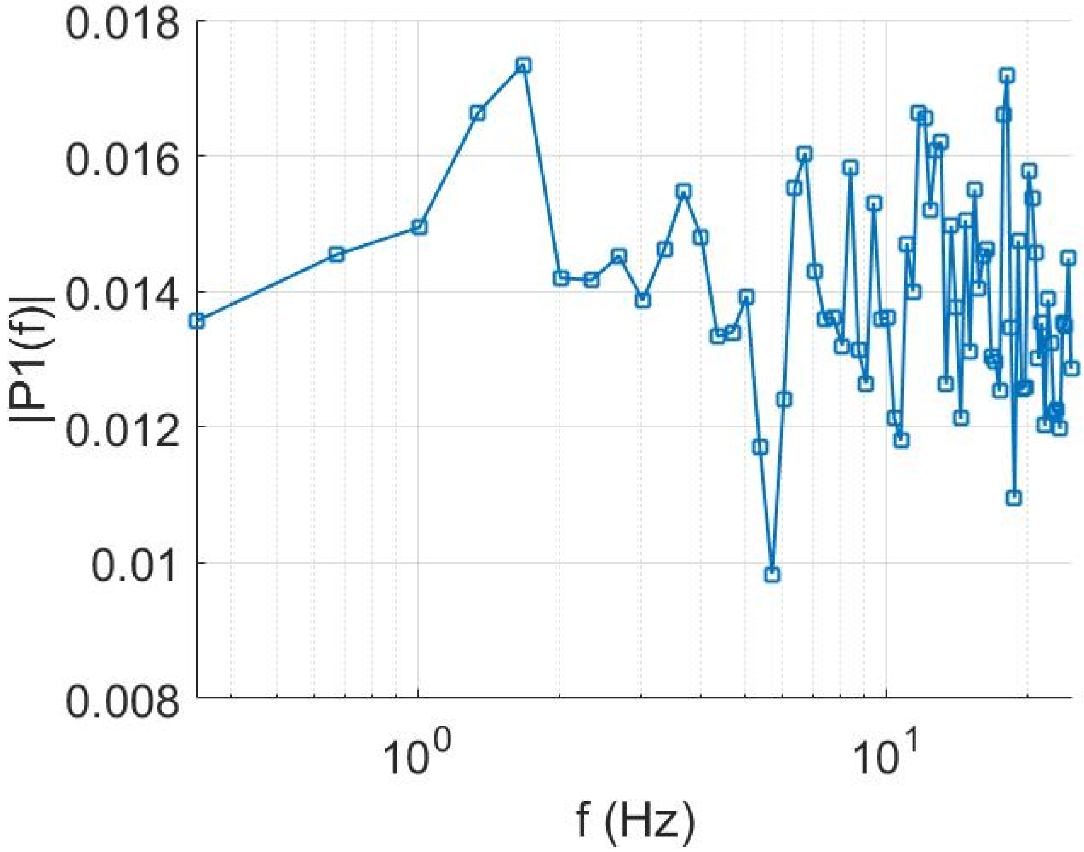

Figure A.10: Frequency response of the illumination source. No obvious frequency peak is found.

B

Appendix

Centrifugal pump characteristics

In this appendix, the centrifugal pump characteristics are added in figure B.1.

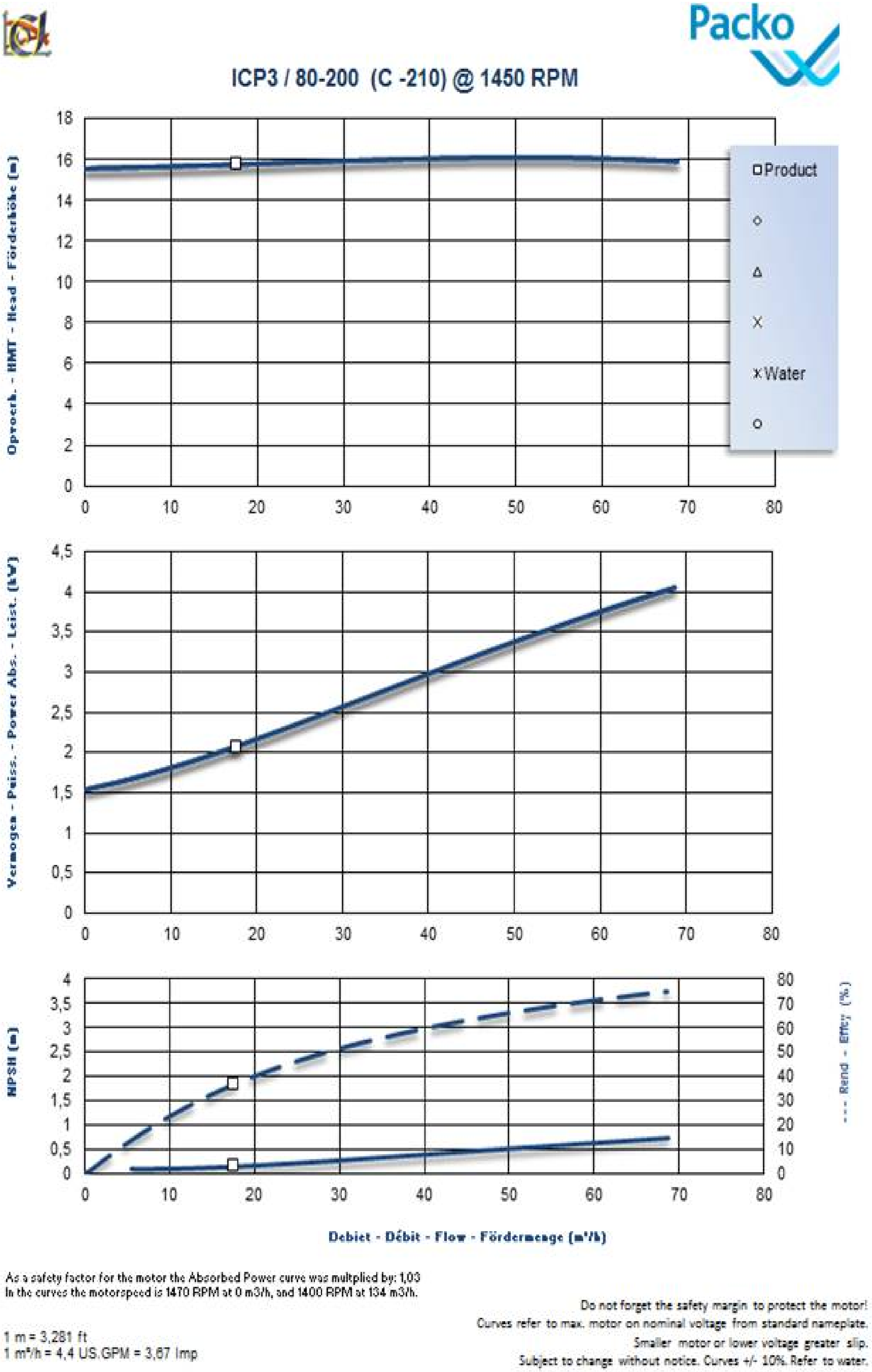

As a safety factor for the motor the Absorbed Power curve was multplied by: 1,03
In the curves the motorspeed is 1470 RPM at 0 m3/h, and 1400 RPM at 134 m3/h.

1 m = 3,281 ft
1 m³/h = 4,4 US.GPM = 3,67 Imp

Do not forget the safety margin to protect the motor!
Curves refer to max. motor on nominal voltage from standard nameplate.
Smaller motor or lower voltage greater slip.
Subject to change without notice. Curves +/- 10%. Refer to water.

Figure B.1: The pump characteristics.

C

Appendix

Matlab code for x-t diagram generation from highspeed videos

This code creates an x-t diagram (output: X) for a selected videofile (avi.)

```
% Initializations
% Load and allocate video
[filename, pathname] = uigetfile( ...
    {'*.avi','Data Files (*.avi)'; ...
    '*.*',  'All Files (*.*)'},...
    'Select video file to analyse');
v = VideoReader(strcat(pathname,filename{1}));  % Allocate video to v

% Ask for user input
prompt={'Enter the camera framerate (in Hz)'};
name = 'Frame Rate';
defaultans = {num2str(framerate)};
options.Interpreter = 'tex';
Fs = inputdlg(prompt,name,[1 35],defaultans,options);
Fs = str2double(Fs{1});            % Inserted framerate in Hz (samp. freq.).

% Video initializations
L = round(v.Duration*v.FrameRate); % Length of signal
T_end = L/Fs;                      % Determine total video time

% Preallocations
t = (1:L-1)*T_end/L;               % Time vector
X = meshgrid(zeros(1,v.Width),t);  % X,t Diagram

% Initialize parameters for rectangle
rx = v.Width/2;                    % Rectangle x center
ry = 210;                          % Rectangle y center
rw = v.Width-1;                    % Rectangle with
rh = 100;                          % Rectangle heigth

% Define rectangle
rectImage = false(v.Height, v.Width);
rectImage((ry-0.5*rh:ry+0.5*rh),(ceil(rx-0.5*rw):ceil(rx+0.5*rw))) = true;

% Determine X-t diagram
h = waitbar(0);
for i = 1:L
    vidFrame = readFrame(v);       % Load videoframe

    % Mask the image with the rectangle.
```

```
    maskedImage = vidFrame;         % Initialize with the entire image.
    maskedImage(~rectImage) = 0;    % Zero image outside the rectangle mask.
    X(i,:) = 255-(sum(maskedImage)/(rh+1)); % X is gray value index
    waitbar(i/L,h,sprintf('Processing video: %3.1f %% ',i*100/L))
end
delete(h)
```

Matlab code for cavity shedding frequency determination from x-t diagram

In this section the code for the determination of the shedding frequency of the cavities is provided. Four inputs are required for this code. In the first place the x-t diagram (X matrix determined in the code above). In this diagram a Fast Fourier Transform is performed along the time dimension. In the second place the sample frequency or framerate is required, for the calculation of the right frequency. In the third and fourth place, the lower and upper bound of the position (x-dimension) is required, between which the frequency is determined.

```
% Initializations
[L, ~] = size(X);                            % Length of signal
T_end = L/Fs;                                % Determine total video time
t = (1:L-1)*T_end/L;                         % Time vector

K = X(:,1:n2)-repmat(mean(X(:,1:n2)),[L,1]); % Save X data to K, with zero average

% Boundary initializations
N = floor(L/240);                            % Number of divisions of P. spectrum
Li = floor(L/N);                             % Divide into # parts
S = (1:1:N);                                 % Section numbers
L1 = (S-1)*Li+1;                             % Define lower boundary
L2 = L1+Li-1;                                % Define upper boundary

% Preallocations
Y = zeros(Li,n2,N);
P2 = zeros(Li,n2,N);
P1 = zeros(Li/2+1,n2,N);
clear fd
fd(:,1) = Fs*(0:(Li/2))/Li;                  % Set up frequency domain
w = repmat(hann(Li),1,n2);                   % Apply hanning for edge effects
% w = ones(size(w));                         % Select this one to undo hanning

% Perform fft on this data
for i = 1:N
    %take datasamples
    Y(1:Li,1:n2,i) = K(L1(i):L2(i),:);       % Write data from K to Y
    Y(1:Li,1:n2,i) = fft(w.*Y(:,:,i));       % Perform Fast Fourier Transform on Y
    P2(:,:,i) = abs(Y(:,:,i)/Li);
    P1(:,:,i) = P2(1:Li/2+1,:,i);            % Calculate symmetric power
    P1(1:end,1:end,i) = 2*P1(1:end,1:end,i); % Normalize power
    P1(1,1) = 0.5*P1(1,1);                   % Correct initial value
    P1(end,end) = 0.5*P1(end,end);           % Correct final value
end
P_avg = mean(P1,3);                          % Average p.s. to make it smoother
P_avg(fd < lowpass,:) = 0;                   % Cut-off frequencies below lowpass
P_avg(fd > highpass,:) = 0;                  % Cut-off frequencies above highpass

% Select the region of interest by applying a bandwith filter
[~, ymax(1:n2)] = max(P_avg(:,1:n2));
P1c = zeros(size(P_avg,1),n2);               % Initialize corrected P1
c = 2;                                       % Bandwith around max

for i = 1:n2
    if (ymax(i) - c) < 1
        ymax(i) = c+1;
    elseif (ymax(i) + c) >= size(P_avg,1)
        ymax(i) = ymax(i) - c;
    else
        ymax(i) = ymax(i);
    end
```

```matlab
    P1c(ymax(i)-c:ymax(i)+c,i) = 1;           % Define bandwith in P1
end
P1c = P1c.*P_avg;                             % Select bandwith values in P1

% Curvefitting and frequency determination
n = 25;
x = zeros(n,1);
val = floor(n1+linspace(1,n2-n1,n));
for i = 1:n
    ind = find(P1c(:,val(i))~=0);             % Find index values
    fdc = [fd(ind(1))-(fd(ind(2))-fd(ind(1))), fd(ind)', Fs]'; % Def. freq. domain
    Pc = [0, P1c(ind,val(i))', 0]';           % Define Power data
    % Make fits at different cross-sections with first order gaussian:
    f = fit(fdc,Pc,'gauss1');
    % Find frequency at maximum point of function:
    x(i) = f.b1;
end
freq = mean(x);                               % Frequency is mean of n values
```

Matlab code for cavity length determination from x-t diagram

In this section the code for the cavity length determination is presented. The .mat file is required, in which the x-t diagram is saved. The average maximum cavity length (at time instant of detachment) is based on five measurements.

```matlab
% Initializations
scale = 1/7.8;                                  % mm/px

[filename, pathname] = uigetfile( ...
    {'*.mat','Data Files (*.mat)';'*.*', 'All Files (*.*)'},'Select file');
load([pathname,filename]);
fprintf(['Selected file:',filename,'\n']);

% Length determination code
[L, n] = size(X);                               % Length and width of video

X1 = X-repmat(mean(X,2),[1,size(X,2)]);         % Zero-average X and save to X1
X2 = fliplr(abs(X1.*(X1 < 0)));                 % Make cavities zero and flip
X2 = X2./max(X2,[],2);                          % Normalize X2

z = zeros(1,n);                                 % Preallocate vector z for storage of cavitation area
for i = 1:n
    z(i) = nnz(~X2(:,i));
end

% point selections
[~, yind] = max(abs(diff(z(1:n/2))));           % Find y-index value of cavitation start

% Pre-allocate data
n = 5;      % number of data points
X3 = zeros(n,size(X2,2)-yind+1);
X4 = zeros(n,size(X2,2)-yind+1);
exppos = zeros(n,1);
indx = zeros(n,1);

% figure
figure(1);
subplot(1,2,1), hold on
li = 0; ci = 1; ri = size(X2,2)-yind;
contourf(X2(ci:end,yind:end),4);

for i = 1:n
    % Y position (line)
    % Plot contour and select cavity length position
    subplot(1,2,1), hold on
    str1 = 'Select point';
    title([str1, num2str(i)])
    [~,ypos(i)] = ginput(1); ypos(i) = round(ypos(i))+ci;
    plot([0,ri],[ypos(i)-ci, ypos(i)-ci],'-r','Linewidth',1.2)

    % Check whether the right y-position is selected
    crit = 0; % Criterium is not met

    while crit ~= 1
        % plot cross-secton of contour:
        subplot(1,2,2), hold on, grid on
        cla     % Clear axis
        ef = 800;
        plot(X2(ypos(i)-1,yind:ef),'--','Linewidth',0.8) % plot -1
```

```
        plot(X2(ypos(i),yind:ef),'k','Linewidth',1.0)    % plot selected curve
        plot(X2(ypos(i)+1,yind:ef),'--','Linewidth',0.8) % plot +1
        legend('Curve -1','Selected curve','Curve +1')

        % Ask for user input, correct y position (line):
        options.Interpreter = 'tex';
        options.Default = 'Yes';
        qstring = 'Is the right curve selected?';
        a1 = sum(double(questdlg(qstring,'Boundary Condition',...
            '<<','Yes','>>',options)));

        % check selection and change y position
        if a1 == sum(double('Yes'))    % then the middle curve is selected
            ypos(i) = ypos(i);
            crit = 1;
        elseif a1 == sum(double('<<')) % then first left curve is selected
            ypos(i) = ypos(i)-1;
            crit = 0;
        elseif a1 == sum(double('>>')) % then first right curve is selected
            ypos(i) = ypos(i)+1;
            crit = 0;
        end
    end

    % X position
    % determine the correct x-position and plot
    X3(i,:) = X2(ypos(i),yind:end);
    X4(i,:) = X3(i,:);
    exppos(i,1) = nnz(~X3(i,:));
    X4(i,1:round(exppos(i)*0.40)) = 0;
    indx(i,1) = find(X4(i,:) > 0,1);
    plot(indx(i),0,'k*')

    crit = 0;   % Criterium
    while crit ~= 1
        % Ask for correct x position:
        prompt={'Right x position selected?'};
        name = 'Selection';
        defaultans = {num2str(indx(i))};
        options.Interpreter = 'tex';
        answer = inputdlg(prompt,name,[1 35],defaultans,options);
        a2 = str2double(answer{1});

        if a2 ~= indx(i) % position is changed
            exppos(i) = a2;
            X4(i,:) = X3(i,:);
            X4(i,1:round(exppos(i)-20)) = 0;
            indx(i,1) = find(X4(i,:) > 0,1);
            plot(indx(i),0,'k*')
            crit = 0;
        else    % nothing is changed
            exppos(i) = exppos(i);
            crit = 1;
        end
    end
end
close(figure(1))

% Calculate and print cavity length
l0 = mean(indx)*scale;
fprintf('The mean cavity length is %3.1f +/- %3.1f mm \n',l0,std(indx*scale))
```